



POLITECNICO DI MILANO
DEPARTMENT OF PHYSICS
DOCTORAL PROGRAMME IN PHYSICS

ADVANCES IN BROADBAND TIME-RESOLVED
SPECTROSCOPY OF DIFFUSIVE MEDIA - FROM PHYSICS
TO CLINICS

Doctoral Dissertation of:
Sri Rama Pranav Kumar Lanka

Supervisor:
Prof. Antonio Pifferi

Tutor:
Prof. Paola Taroni

Coordinator:
Prof. Marco Finazzi

2019 – XXXII Cycle

Acknowledgements

All the work leading to this PhD dissertation was funded by BitMap (Brain injury and trauma monitoring using advanced photonics) an H2020 MSCA-ITN-ETN - Training Network. The author is a Marie Curie fellow funded by this project. The author expresses his utmost gratitude to his supervisor (Prof. Antonio Pifferi) and tutor (Prof. Paola Taroni) for their constant support and guidance. The author is also grateful to the European Commission and the European Union for their financial and overall support.

Preface

THE research presented in this thesis, was carried out mainly in the Department of Physics of Politecnico di Milano. Fundamentally, it deals with the interaction of light with highly diffusive or scattering media. A particularly interesting example of such diffusive media is biological tissue. The capabilities of such diffusive media to absorb and scatter light are quantified by parameters known as absorption (μ_a) and scattering (μ_s). The knowledge of these properties (known generally as *optical properties*), particularly for different wavelengths ("colors") of light is very useful in the assessment and analysis of tissue health, to diagnose diseases and in laser related treatment methodologies. Such *broadband spectral* information of these two properties provides information about the composition and the morphology of the sample. Considerable progress has been achieved in this field over the last few decades and the number of applications that it has been used for has only been increasing over time. A brief description of this theory along with some basic physics and methodology, particularly relevant to the rest of the thesis, is presented in **Chapter 1**.

Several techniques have been implemented for the characterization of these optical properties over a broad spectral range, such as Continuous Wave (CW), Time-Domain (TD), Frequency-Domain (FD) and Spatial Frequency Domain Imaging (SFDI). Of these, the work described in this thesis mainly used the TD approach. An instrument that can perform TD measurements to recover the broadband optical properties of biological tissue in the wavelength region of 600 - 1100nm (also known as the therapeutic window) at multiple inter-fiber distances was developed during this course of the work leading to this dissertation. The ability of the instrument to perform multi-distance measurements is very useful as it permits the study of heterogeneous or layered media with better accuracy. **Chapter 2** describes in detail the design, development and some of the novel features of this system. The system was designed to be portable which permits its usage beyond the lab and in a clinical scenario. Additionally, the system was validated using well established performance assessment protocols and will soon be enrolled in a Hospital in Verona to non-invasively assess the physical frailty of the elderly and the obese.

Chapter 3 demonstrates the ability of the instrument to accurately decouple the

optical properties of layered diffusive media. To this end, two layered samples with known optical properties engineered using different kind of base materials were designed and an analytical model that employs multi-distance measurements, such as the ones provided by this instrument, was used to disentangle the optical properties of the two layers. The results fared better in comparison to the results from the traditional analysis models. The broadband data also provides information about the composition of the different two-layer structures which further demonstrates the need of such instruments and analysis methods while dealing with layered media (e.g. the human abdominal region or the forehead region). The chapter concludes with some interesting results from *in-vivo* measurements on the human forehead region which is known to display a layered geometry.

Chapter 4 deals with a pre-clinical *in-vivo* measurement campaign aimed at understanding the feasibility of the TD spectroscopy technique in the non-invasive assessment of the human abdominal region. A total of 10 healthy male volunteers were enrolled for the study and multi-distance measurements were performed on five different regions of the abdomen. The results clearly suggest that the stratified nature of the abdominal region, composed primarily of skin, fat tissue and underlying muscle has a visible impact on the recovered optical properties and hence demands caution in the straight forward application of the traditionally used analysis methodologies. A set of simulations were performed to further validate the results observed from these measurements.

A novel application of the broadband TD diffuse optics spectroscopy (TD-DOS) is presented in **Chapter 5**. An instrument similar to the one developed during the course of this thesis is used to understand the influence of thermal treatment methodologies (e.g. Radio Frequency Ablation or Microwave ablation) on the broadband optical properties of biological tissue. The measurements are performed on different types of *ex-vivo* bovine tissue. Interesting variations are observed in the recovered optical properties as the tissue undergoes the thermal treatment methodologies. While these variations need to be further validated in an *in-vivo* scenario, these findings prove that optical properties obtained using broadband TD-DOS could be of great value in monitoring the above mentioned thermal treatment methodologies in a clinical environment.

Finally, **Chapter 6** summarizes some of the initial results from a multi-laboratory performance assessment exercise titled " the BitMap Exercise" (named after the BitMap Marie Curie consortium, an EU level consortium which funds the author of this work). A total of 29 diffuse optics instruments were enrolled for the exercise, making it the largest of its kind. Instruments with different techniques, applications and levels of technological readiness are enrolled for the exercise. The exercise is still in progress with the author of this work playing a key role in its organisation and implementation. Some preliminary results from this ambitious exercise comparing the performance of various instruments are presented.

Contents

1	Diffuse Optics: an Introduction	1
1.1	Light Matter Interaction	1
1.2	Transparent and Diffusive Media	2
1.3	Applications of Diffuse Optics in Biological Tissue	3
1.3.1	Diffuse Optical Spectroscopy (DOS)	3
1.3.2	Diffuse Correlation Spectroscopy (DCS)	4
1.4	Techniques and Instrumentation	4
1.4.1	Continuous Wave	5
1.4.2	Frequency Domain	5
1.4.3	Time Domain	5
1.4.4	Spatial Frequency Domain Imaging	7
1.4.5	Overview and discussion	8
1.5	Models of Photon Propagation in Diffusive Media	9
1.5.1	The Radiative Transport Theory	9
1.5.2	The Diffusion Approximation	10
1.6	Analytical Solutions of the Diffusion Equation in the Time Domain	11
1.6.1	Case1: Homogeneous Medium	11
1.6.2	Case2: Multilayered media	13
1.7	Stochastic (Monte Carlo based) Solutions of the RTE in Time Domain:	15
1.8	Optical Properties (μ_a, μ_s) Estimation	16
2	Broadband Multi-distance TD-DOS Instrumentation for Clinical Use	19
2.1	Introduction	19
2.2	Design and Characteristics of Instrument	20
2.2.1	Optical Layout of the instrument	20
2.3	Novel Features:	21
2.4	Characterization and Performance Assessment	25
2.4.1	Accuracy	25
2.4.2	Linearity	27
2.4.3	Noise/Uncertainty	28
2.4.4	Stability	28

Contents

2.4.5	Reproducibility	29
2.5	Clearance for clinical Use:	29
2.6	Conclusions	30
3	Retrieval of Absolute Optical Properties from Heterogeneous/Layered Diffusive Media	31
3.1	Introduction	31
3.2	Silicon Based Two-layer structures	32
3.2.1	Analysis using Homogeneous Model	33
3.2.2	Analysis using Layered Model	33
3.2.3	Spectral Fitting – Quantification of Absorber Concentrations	37
3.3	<i>Ex-vivo</i> Biological Tissue Based Two-layer structures	39
3.3.1	Analysis using Homogeneous Model	39
3.3.2	Analysis using Layered Model	40
3.3.3	Spectral Fitting – Quantification of Absorber Concentrations	40
3.4	Initial Application <i>In-vivo</i>	41
3.4.1	Analysis using Homogeneous Model	42
3.4.2	Analysis using Layered Model	42
3.4.3	Spectral Fitting – Quantification of Absorber Concentrations	42
3.5	Conclusions:	44
4	<i>In vivo</i> Application of Broadband DOS for Layered Media: Abdominal Adipose Tissue	47
4.1	Introduction	47
4.2	Broadband optical properties of the human abdomen <i>in-vivo</i>	48
4.2.1	Subjects, Measurements and Analysis	48
4.2.2	Absorption and Reduced Scattering spectra	50
4.3	Tissue Composition:	53
4.4	Broadband Simulation of Multi-distance measurements on the Abdomen:	53
4.5	Initial application of the two-layered model	56
4.6	Conclusions	57
5	Optical Signatures of Thermal damage in Biological tissue - an exploratory study on <i>ex-vivo</i> biological tissue	61
5.1	Introduction	61
5.2	Optical characterization of <i>ex-vivo</i> Porcine Tissue	63
5.2.1	Measurement Setup, Samples and Analysis	63
5.2.2	Optical Property Spectra	65
5.3	Optical characterization of thermal treatment using Radio Frequency Ablation (RFA)	67
5.3.1	Measurement Setup, Samples and Analysis	67
5.3.2	Spectra of Optical Properties before and after thermal treatment:	68
5.3.3	Spectral evolution of Optical Properties during thermal treatment	70
5.3.4	Time Evolution of Optical Properties with thermal treatment:	71
5.3.5	Discussion on the observed variations	74
5.4	Conclusions	79

6 Multi-laboratory Efforts towards Performance Assessment in Diffuse Optics - The BitMap Exercise	81
6.1 Introduction	81
6.2 Protocols, Phantoms and Implementation	82
6.2.1 Actions	82
6.2.2 Protocols and Phantoms:	83
6.2.3 Institutions and Instruments:	84
6.3 Preliminary Results from Action 1	86
6.3.1 Basic Instrument Performance:	86
6.3.2 MEDPHOT (Absolute Optical Properties)	88
6.3.3 the nEUROPt Protocol:	99
6.4 Conclusions:	101
7 Conclusions:	103
Bibliography	105
Appendix A Supplementary Information for Chapter 4	105
Appendix B Supplementary Information for Chapter 5	115

CHAPTER 1

Diffuse Optics: an Introduction

This chapter is aimed at offering the reader an introductory perspective on the theory of diffuse optics. Firstly, some of the fundamental properties are presented followed by a basic understanding of how it is employed in the field of Biomedical imaging and spectroscopy. Second, the fundamental classification of instrumentation used is discussed. Then, the different strategies and models of analysis, particularly relevant to this work, are presented. The chapter is concluded by a brief discussion of the state-of-the-art advances and the pertinent challenges of the field and the significance of this work in resolving some of these issues.

1.1 Light Matter Interaction

Matter is influenced by and interacts with light in different ways and the study of these interactions is something that spans a wide number of disciplines from optical and atomic physics, electrical and solid state physics, and recently in biology and medicine too. Depending on the number of interacting particles and the complexity of the interaction different models have been formulated to aid this study. The most accurate modelling requires a quantization of both the illuminating electromagnetic field and the matter under consideration [1]. This however gets exponentially more complex as the number of atoms or molecules in the sample increase. In such cases, a semi-classical approach is preferred. This, as the name suggests, quantizes only the material (sample) while describing the field using the well-known Maxwell's equations [2]. Further complexity arises when the matter under consideration is extremely dense and inhomogeneous at a micro-level. Such a situation demands a further simplification in the modelling. One good example of this is the highly scattering or *diffusive media*, like biological tissue. Biological tissue, which is the primary focus of most of the studies

presented in this thesis, is essentially comprised of *absorbing agents* or *chromophores* and *scattering centers*. Consequentially, these constituents are responsible for the main interactions that light undergoes as it interacts with tissue, namely *absorption* and *scattering* respectively. The interaction of light with such diffusive media is modelled as photons, which are quantized particles of light, colliding elastically with the scattering centers and being absorbed by the chromophores. Quantification of these features is then achieved by considering the probability of the occurrence of an absorption or scattering event in a unit length of the medium. These quantities are defined as the absorption μ_a and scattering coefficients μ_s , respectively.

1.2 Transparent and Diffusive Media

Matter that is completely devoid of scattering centers is labelled *transparent*. Depending upon its composition and the wavelength or 'color' of the light used it either absorbs the light or lets it pass through undeviated. This interaction can be described using the famed Lambert-Beer law, which can be expressed as:

$$I = I_0 \exp [-\mu_a L] \quad (1.1)$$

Here I_0 represents the intensity of the input light, I is the intensity of the light after the interaction and L corresponds to the thickness of the sample along the direction of propagation of the incident light. As mentioned earlier, this quantity contains information regarding the chromophores in the transparent media and the concentration of these chromophores can be obtained from the spectrum of this coefficient using the formula.

$$\mu_a(\lambda) = \sum_i c_i \varepsilon_i(\lambda) \quad (1.2)$$

This is known as the Beer's Law, and is valid as long as the intensity of the incident light is sufficiently low, to avoid any significant non-linear interactions. Here c_i is the molar concentration and ε_i is the molar coefficient of extinction at a given wavelength λ .

When the number of scattering centers in a medium start to increase, the photons tend to encounter not just absorption but scattering events as well. In particular, when the number of scattering events in a medium exceed considerably the number of absorption events then the medium is considered to be *diffusive*. At this level, the scattering centers in diffuse media tend to scramble the photons in random directions. At a microscopic level, the size of these scattering centers are comparable to the wavelength of light, with different irregular shapes and varying optical properties. This in-homogeneity at the microscopic level results in a diffusive spread of light at macroscopic level. Typically, in **biological tissue**, the tissues are composed of cells and organelles with size comparable to light wavelength making them an ideal diffuse media.

1.3 Applications of Diffuse Optics in Biological Tissue

1.3.1 Diffuse Optical Spectroscopy (DOS)

Atmospheric scattering, real-time monitoring of ocean water using optics and material science are some cases where studying the diffusion of the radiation in the material could be valuable. However, the most important contribution of Diffuse Optics is in the field of biomedical imaging and spectroscopy. Biological tissue is strongly scattering in the visible and NIR wavelength regions. Moreover, the wavelength region below 600nm is absorbed heavily by 'red' blood cells and the region above 950-1000nm by water (OH^- ions). Therefore, most studies involving biological tissue, use radiation from the 600-1100nm wavelength region, which permits for a better penetration depth into the tissue [3].

While, valuable information regarding blood oxygenation could be obtained by measuring the diffusion of light at two or three wavelengths, broadband or multi-wavelength measurements provide us with the unique possibility of estimating the tissue chromophore concentration as discussed in Eq. (1.2). As mentioned earlier, the only prerequisite here is the spectra of the extinction coefficients.

The chromophores contributing to most of the absorption in biological tissue in this wavelength region are: water, lipid/fat, collagen, oxy and de-oxy hemoglobin. The concentration independent extinction coefficient $\varepsilon_i(\lambda)$ of these chromophores is shown in Figure 1.1.

The concentration of these chromophores could be valuable in monitoring and imaging specific changes in the tissue. For instance, concentrations of oxy and de-oxy hemoglobin can be studied to monitor in real-time the functional activation of regions in the brain [4]. Similarly, studies have shown that the amount of collagen, lipid and water present in the breast is a key indicator for the assessment of the risk of breast cancer and related pathologies [5]–[8]. Recent studies have also employed diffuse optics for thyroid cancer detection by non-invasively monitoring the concentrations of tissue constituents in the thyroid region [9].

Further valuable information regarding the physical nature of the biological tissue can be obtained by analysing the scattering coefficient. Scattering of light, generally occurs due to the presence of localized non-uniformities in the medium, which tend to deviate or 'scatter' the incident light from its original direction. For most biological tissues the scattering spectra can be described by an empirical law in the form

$$\mu_s = a \left(\frac{\lambda}{\lambda_0} \right)^b \quad (1.3)$$

Using the Mie theory, the coefficients a and b can be linked to the density and effective radius of the spherical 'scattering' centers [10]. This assumption does not always hold and in such cases numerical simulations are necessary.

The technique described above is termed as Diffuse Optical Spectroscopy (DOS) and will form the crux of the measurements and results reported in this thesis. It is, however, interesting to know that an imaging analog of DOS called Diffuse Optical Tomography (DOT) exists, which basically assigns the optical and physiological properties mentioned above to multiple volume elements in the tissue sample to create a 2D or 3D map of the tissue.

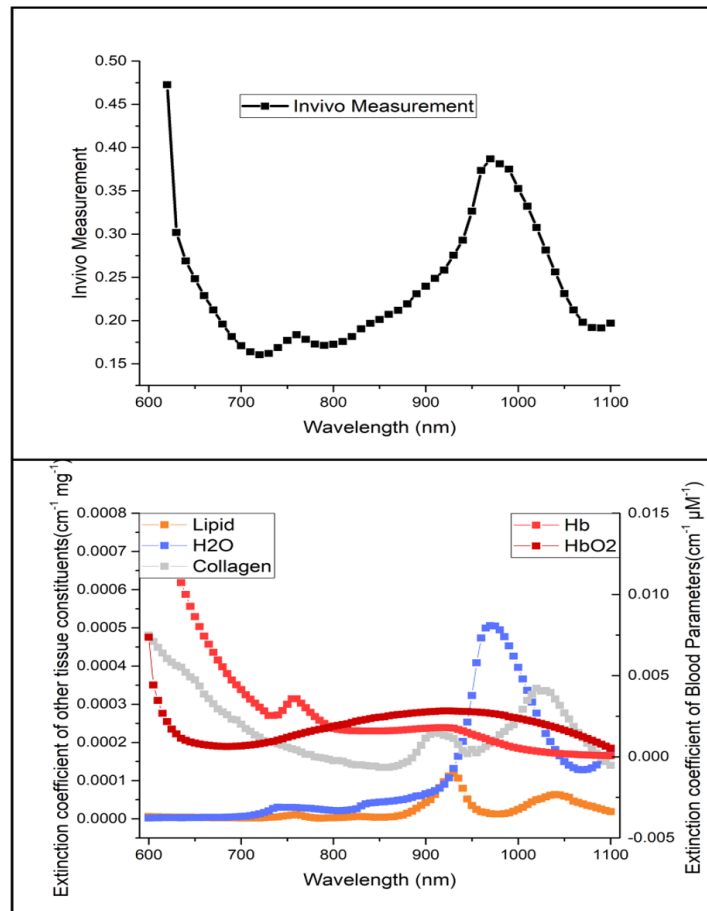


Figure 1.1: (below) Extinction Coefficients of some of the key chromophores and absorbers in biological tissue over the wavelength region of interest. (above) Absorption coefficient spectra of the human forehead. Clear correspondence can be observed between the key spectral features of the biological tissue and the outstanding features of the chromophore spectra.

1.3.2 Diffuse Correlation Spectroscopy (DCS)

More information can be obtained from the light that is diffused in tissues. The motion of the dynamic scatterers present in 'living' tissue like red blood cells (RBCs) could create fluctuations in the speckle patterns of the scattered light. The study of these dynamic light scattering measurements to measure cell movements of interest such as the cerebral blood flow (CBF), is known as Diffuse Correlation Spectroscopy (DCS) [11], [12]. This technique will not be discussed here in detail since it is out of the scope of this thesis but interested readers can find further information in the references presented.

1.4 Techniques and Instrumentation

The estimation of optical properties of diffusive media can be achieved by employing different techniques. These are classified based on the spatial distribution and temporal characteristics of the source or incident illumination and the detection strategies used. A brief schematic of four of the most common techniques or modalities employed in this

field are presented in Fig. 1.2. Here we discuss these techniques in detail with some examples of instruments developed by research groups from different parts of Europe and the World.

1.4.1 Continuous Wave

The continuous wave (CW) modality [13] utilizes CW light sources like lamps, LEDs and CW lasers to illuminate the tissue under investigation and detects the diffusely reflected light to estimate the optical properties. This modality is widely used and boasts a considerable presence in the clinics[14]–[16], due to its cost effective and scalable nature. However, a single CW measurement would measure the relative attenuation of the light which is not sufficient to retrieving both optical properties. This problem, is overcome by making multiple measurements spatially, as shown in Fig. 1.2 (a). Extensive models have been developed in this direction but are beyond the scope of this work [17]. Many successful CW systems have been developed [14], [15] and employed in various in-vivo studies [16].

1.4.2 Frequency Domain

Another modality that surpasses some of the disadvantages of the CW technique is the Frequency Domain (FD) based DOS [18], [19]. This is based on light sources that are amplitude-modulated, with modulation frequency ranging from 100 MHz up to 1 GHz. A radio-frequency oscillator is used to drive the source and also provide the reference signal for the phase measurement. Propagation of this modulated light through tissue could be envisioned as low-pass filtering: the amplitude decreases and the phase increases with increasing frequency [20]. Since the diffusion information is encoded in phase signal, it is possible to evaluate the scattering coefficient independent of the absorption, thus allowing the estimation of absolute values of the optical properties 1.2 (b). Moreover, FD instruments can provide fast sampling (up to 50 Hz) which is of great value when monitoring real-time *in vivo* signal. Apart from the complex and bulky instrumentation this technique also faces one other challenge: the in-availability of broadband frequency domain sources. This is however, overcome using a very clever trick which exploits FD and CW instrumentation together where each of the techniques can complement the other. The CW instrument performs broadband measurements and the FD measurements are performed at few points to extract the scattering coefficients of the diffusive media. These values are then extrapolated over the broadband wavelength range using the 'Mie' law discussed in 1.3, thus obtaining broadband optical properties. Some of the successful implementations of FD instruments can be found in [21], [22].

1.4.3 Time Domain

Finally, we discuss the time-domain (TD) or time-resolved modality which injects a picosecond scale pulse into the tissue or diffusive medium. The scattering and absorption events occurring in the tissue lead to a subsequent attenuation and broadening in the pulse to the nanosecond regime 1.2 (c). The early region of the peak is predominantly effected the scattering properties of the medium as the photons have travelled a relatively shorter path length and thus have a lower probability of being absorbed by

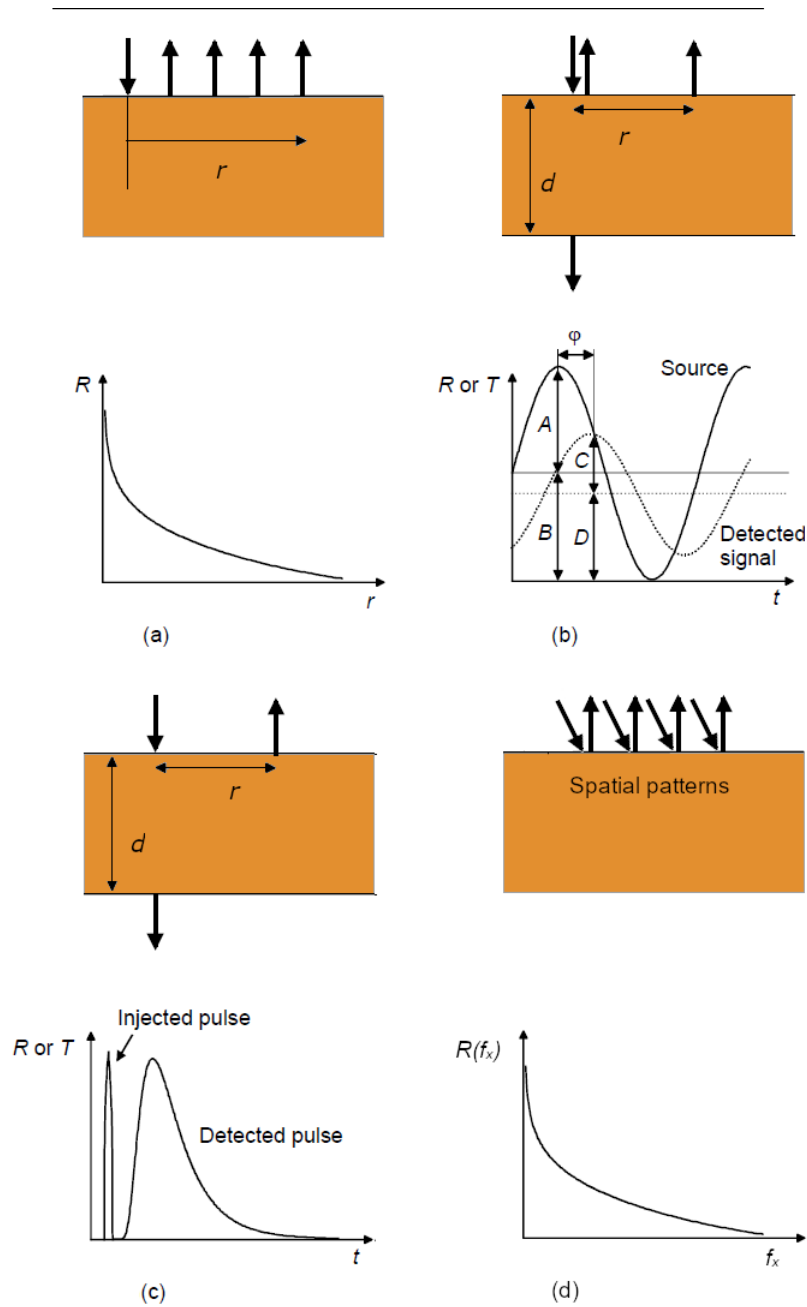


Figure 1.2: Techniques commonly used in DOS instruments (a) Continuous Wave or spatially resolved reflectance measurement; (b) Frequency-modulated or frequency domain where the phase shift ϕ and modulation depth $[(C/D)/(A/B)]$ are measured and used to obtain the optical properties (c) Time Resolved or time domain technique wherein a short temporal pulse is injected into the biological medium and the temporal point spread function is analysed to retrieve the optical properties and (d) Modulated Imaging where the source projects a pattern on the sample and the reflectance is analyzed as a function of the modulation frequencies to retrieve the optical properties

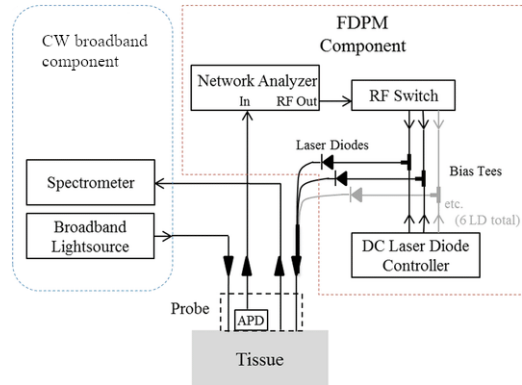


Figure 1.3: A block diagram of a frequency domain photon migration instrumentation complemented with a broadband CW instrument. (courtesy of Thomas D O’Sullivan [23])

the tissue. Consequently, the later part of the broadened curve contains information regarding the absorption events occurring within the tissue at that specific wavelength. In this way, a single measurement using TD techniques with necessary analysis allows for an independent estimation of both optical properties[19].

Instruments based on TD techniques require sources providing pulsed light and detection electronics with high temporal resolution (sub nanosecond). These detectors should also possess high sensitivity factors and should be able to detect single photon events. Two such detection technologies exist in the market currently, these are Streak Cameras and correlated single photon counting (TCSPC).

In theory, frequency domain and time domain are expected to be equivalent but in practice, the limited number of modulation frequencies limits the information content of frequency domain techniques considerably in comparison to time domain techniques. This could be utmost relevance when investigating complex heterogeneous or layered biological media.

1.4.4 Spatial Frequency Domain Imaging

One technique that has seen a rapid rise in applications, in recent times, thanks to it’s capability to provide wide field quantitative images of biological tissue, is Spatial Frequency Domain Imaging (SFDI). The basic measurement principle behind this technique is described below. A two-dimensional pattern of light is projected onto the sample and the reflected or transmitted pattern is captured on a digital camera. The multiple scattering and absorption events occurring lead to a decrease in the amplitude of the projected pattern. This amplitude is then used to obtain the spatial modulation transfer function of the sample taking into account the influence of the system’s

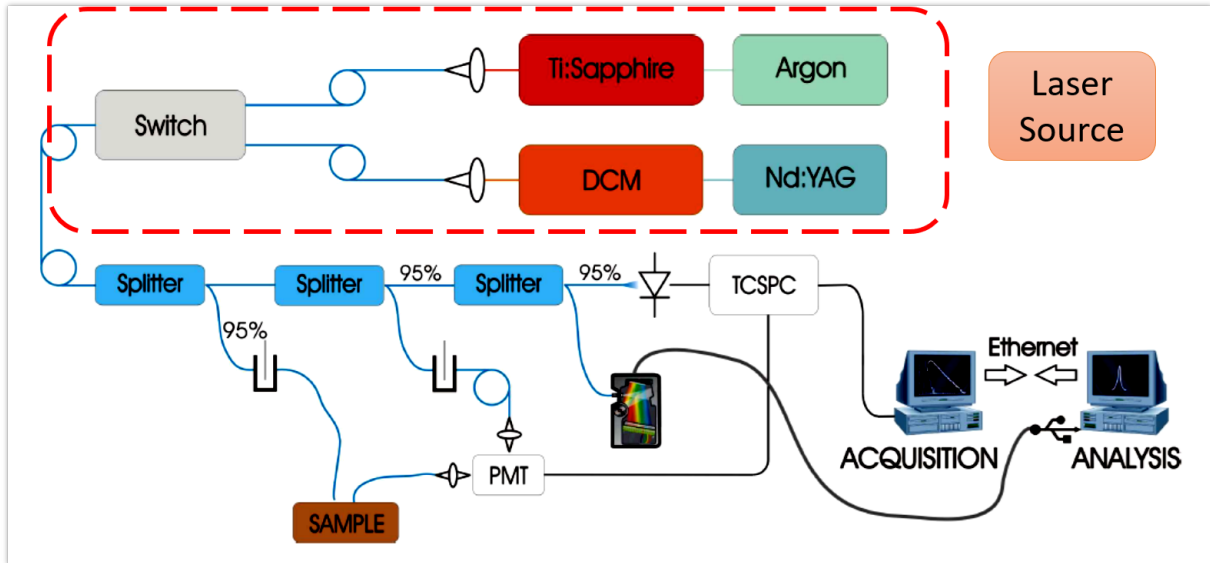


Figure 1.4: Setup for TR optical diffuse spectroscopy based on two tunable lasers and TCSPC technique[24]. (developed in the Politecnico di Milano)

response. Repeating this procedure for multiple frequencies and applying some light propagation model, the optical properties at each pixel can be recovered. Use of multiple wavelengths, either serially or in parallel, compliments the information further [25].

Single wavelength setups require a digital projector to be able to modulate the light source and a CCD or similar imaging detectors to capture the back-scattered image. Broadband systems need broadband sources and tunable filters to allow for a fast wavelength selection over a wide spectral range.

1.4.5 Overview and discussion

Each of the techniques reported above has its own advantages and drawbacks. Of all these, time resolved (TD) techniques has some interesting features such as (i) the ability to disentangle the optical properties using a single measurement (ii) better depth penetration encoded in time information and (iii) free from surface artefacts as a consequence of amplitude independent modelling. This is one of the reason to choose this technique for most of the work reported in this thesis. However, this does not imply that TD techniques dominate the field. In fact, both CW and FD modalities are highly valuable and frequently utilized for many applications.

CW techniques are often cost-effective, compact and user-friendly making them invaluable in clinical scenarios. However, they often suffer from poor spatial resolution and require multi-distance measurements to obtain comprehensive information. Also, they are fundamentally a measure of relative attenuation of the sample and hence cannot separate absorption from scattering. Finally, in some cases CW based instruments also need a reference measurement to quantify the absolute attenuation of the medium.

FD techniques, like CW, boast of a superior source stability in comparison to the TD techniques. Also the advanced electronics used for the modulated signal generation allows for a robust and quick functionality. The Fourier transform relation between time

and frequency suggests, in theory, an equivalence in the information content between TD and FD. However, in reality TD methods excite all the temporal frequencies and hence provide better information content. More importantly, FD methods, in theory can estimate the absolute optical properties but need a calibration of the system on a phantom of known optical properties which is not the case for TD instruments. In conclusion, the choice of the technique or modality is a complex one and depends on numerous factors like the application under question, the penetration depth required and time scale of the reaction/functionality that needs to be monitored.

1.5 Models of Photon Propagation in Diffusive Media

1.5.1 The Radiative Transport Theory

As discussed in 1.1 Maxwell's equations could be the ideal tool to understand the photon propagation in general. However, for diffusive media, the computational complexity involved supersedes the accuracy and exactness provided by this theory. Therefore, a heuristic model, developed originally in the field of astrophysics [26] and subsequently used for the study of energy transport of neutrons [27] in nuclear reactors was chosen as the ideal alternative for this purpose. This theory, known as *the Radiative Transport Theory*[28] considers the particle nature of light and treats the diffusive media as a random distribution of absorption and scattering centers. The theory is based on the following assumptions. First, that the no interference effects occur within the diffusive media. This is a valid assumption since the multiple scattering nature of diffusive media ensures that the coherence of the incident light is destroyed after a few scattering events. Secondly, it assumes that the scattering is elastic, i.e. the radiation does not change frequency or energy after a scattering event.

Equation 1.4 summarizes the key mechanisms that dictate the propagation of photons in a turbid medium. Known as the Radiative Transfer Equation (RTE), or the Boltzmann Transport Equation, this integro-differential equation expresses the principle of conservation of 'light' energy in a volume element of the turbid medium. Let V be a the volume of a turbid medium bound by the surface ∂V . Eq 1.4 is a balance between the incident and output radiation along the direction \hat{s} , at the time t within an infinitesimal volume element $dV \subset V$ at the position $\mathbf{r} \in V$ [28]

$$\begin{aligned} \frac{1}{v} \frac{\partial R(\mathbf{r}, \hat{s}, t)}{\partial t} = & - \hat{s} \cdot \nabla R(\mathbf{r}, \hat{s}, t) - (\mu_a + \mu_s) R(\mathbf{r}, \hat{s}, t) + \\ & + \mu_s \int_{4\pi} p(\hat{s}, \hat{s}') R(\mathbf{r}, \hat{s}', t) d\hat{s}' + Q(\mathbf{r}, \hat{s}, t) \end{aligned} \quad (1.4)$$

Here:

- $R(\mathbf{r}, \hat{s}, t)$ is the radiance (or specific intensity): the power flowing in the direction \hat{s} , per unit of solid angle and area normal to \hat{s} . Mathematically this would be:

$$R(\mathbf{r}, \hat{s}, t) = \frac{d^2 P}{d\Omega dA \hat{s} \cdot \hat{\mathbf{n}}} \quad [W m^{-2} sr^{-1}] \quad (1.5)$$

where P is the power, dA is the area element, $d\Omega$ is the solid angle element and $\hat{\mathbf{n}}$ is the unit vector normal to dA .

- v is the photon velocity given by c/n where c is the speed of light and n is the refractive index of the medium.
- μ_a and μ_s [m^{-1}] are the absorption and scattering coefficients of the medium (discussed in 1.1)
- $-\hat{s} \cdot \nabla R(\mathbf{r}, \hat{s}, t)$ is the net variation in the radiance due to energy flow.
- $-(\mu_a + \mu_s) L(\mathbf{r}, \hat{s}, t)$ is the loss in energy due to absorption and scattering
- $+\mu_s \int_{4\pi} p(\hat{s}, \hat{s}') R(\mathbf{r}, \hat{s}', t) d\hat{s}'$ is the net increase in the energy flow which is a consequence of scattering of light from the other directions. $p(\hat{s}, \hat{s}')$ is the phase function: the probability that a photon travelling in the direction \hat{s} is scattered to the direction \hat{s}' .
- $Q(\mathbf{r}, \hat{s}, t)$ [$Wm^{-3}sr^{-1}$] is the spatial, temporal and angular distribution of a radiation source within V .

Treatment of Absorption: When the source term is a delta function in time i.e. $Q(\mathbf{r}, \hat{s}, t) = S(\vec{r}, \hat{s})\delta(t)$, the effect of absorption centers in the diffusive media can be handled separately. Consider $R(\mathbf{r}, \hat{s}, t)$ as a solution of the non-absorbing medium then the absorption dependent solution could simply be expressed as:

$$R_a(\vec{r}, \hat{s}, t) = \exp(-\mu_a vt) R(\vec{r}, \hat{s}, t) \quad (1.6)$$

Here, μ_a is the absorption coefficient of the medium.

1.5.2 The Diffusion Approximation

As mentioned earlier, the presence of an integral on the right hand side of the equation makes it very difficult to obtain analytical solutions to the RTE. To overcome this difficulty, *Discretization methods* like the Discrete Ordinates Method, [29] the Kubelka Munk Method, [28] Finite Element Method, [30], [31] or stochastic methods, like those based on Monte Carlo are usually employed.

However, further simplification can be achieved using another approach involving *Expansion methods*. As their name suggests, these methods are based on a series expansion of the radiance source term and the phase function of the RTE. Spherical harmonics [32] are usually the base functions of choice. The general nomenclature for such methods is the P_N Approximation Method, where N is the maximum order l of functions Y_{lm} involved in the expansion [19], [33]. The Diffusion approximation (DA) is a special case of the simplest of these, P_1 approximation. The DA reduces the number of variables that contribute to the energy balance expressed through Equation 1.4 with the help of additional assumptions valid for cases where photons undergo multiple scattering events thereby randomizing the initial direction of photon propagation[28], [34]–[37]. The additional assumptions here are:

- **Isotropic radiance:** The predominantly scattering nature of the interaction allows for the radiance term to be re-written as:

$$R(\vec{r}, \hat{s}, t) = \frac{1}{4\pi} \Phi(\vec{r}, t) + \frac{3}{4\pi} \vec{J}(\vec{r}, t) \cdot \hat{s} \quad (1.7)$$

1.6. Analytical Solutions of the Diffusion Equation in the Time Domain

where, $\Phi(\vec{r}, t)$ and $\vec{J}(\vec{r}, t)$ represent the isotropic Fluence and small directional Flux respectively.

- **Negligible flux variation:** The time variation of photon flux in a time corresponding to a mean free path $t = (v\mu_t)^{-1}$ is negligible compared to the total flux;
- **Radial symmetry and Isotropic light source**

The assumptions on the isotropic radiance and negligible flux variation allow for a relation between the fluence and the flux known as the *Fick's Law*[38] and given by :

$$\vec{J}(\vec{r}, t) = -D\nabla\Phi(\vec{r}, t) \quad (1.8)$$

Implementing the above mentioned changes in the RTE, we realize the Diffusion Equation (DE) that is a differential equation for the fluence rate with several solutions available. The requisite mathematics is straightforward and can be found in [39]. The final equation is presented in 1.9

$$\left[\frac{1}{v} \frac{\partial}{\partial t} - D\nabla^2 + \mu_a \right] \Phi(\vec{r}, t) = q_0(\vec{r}, t) \quad (1.9)$$

where $q_0(\vec{r}, t) = \int_{4\pi} Q(\vec{r}, \hat{s}, t) d\Omega$ is the isotropic light source term, and $D = \frac{1}{3\mu'_s}$ represents the *diffusion coefficient*. $\mu'_s = \mu_s(1 - g)$ denotes the reduced scattering coefficient where $g = \langle \cos \theta \rangle = 2\pi \int_0^\pi \cos \theta p(\theta) \sin \theta d\theta$ is the anisotropy coefficient. The anisotropy on the light scattering in the tissue is given by the average cosine of the scattering angle. The inverse of the reduced scattering coefficient gives the *transport mean free path* $l' = (1/\mu'_s)$, which represents the mean distance travelled by photons in a homogeneous medium before they lose information about the initial direction. Similar to the case of RTE Eq. 1.6, the affect of absorption is accounted for in the DE using a multiplication factor. Therefore, if $\Phi(\vec{r}, t)$ is a solution of 1.9 (non-absorbing medium with a delta source), then

$$\Phi(\vec{r}, t, \mu_a) = \Phi(\vec{r}, t, \mu_a = 0) \exp(-\mu_a vt) \quad (1.10)$$

would be the extended solution to a medium with similar scattering characteristics but an absorption coefficient μ_a . Similarly, the radiant flux for this scenario can be estimated by extending this analogy to the *Fick's Law*.

1.6 Analytical Solutions of the Diffusion Equation in the Time Domain

1.6.1 Case1: Homogeneous Medium

As mentioned in 1.4.5 this work primarily deals with DOS in the Time Domain (TD-DOS). Hence, this section briefly discusses some of the solutions of the DE in the time domain for different geometries that are of particular interest to the different applications discussed in this work.

Biological systems of interest can, in general, be modelled as slabs of material, or as semi-infinite media. This finite dimensionality dictates that cases like this require reasonable boundary conditions to complete the mathematical description of the problem.

If there is no mismatch between the refractive index inside and outside V and if ∂V is a convex surface, the radiance flowing outside V is not reflected. The two commonly used boundary conditions are the Extrapolated Boundary Conditions (EBC) and Zero Boundary Conditions (ZBC), both of which approximate the source term as a sum of isotropic point sources, by defining an infinite number of pairs of positive and negative sources (sinks) that set the fluence at the boundary of choice. In the EBC, the fluence rate is assumed to be null at an imaginary surface at distance $z_e = 2AD$ from the interface, where A is the parameter that accounts for refractive index mismatch and D is the diffusion coefficient. The ZBC, on the other hand, relies on the assumption that the fluence rate is null at the physical interface. Both give similar solutions (3% variation in final output at source detector separation larger than 5mm). EBC is usually preferred due to simpler analytical expressions [40]. The Boundary conditions are discussed in detail in the following references ZBC [19], [31] and EBC [33], [40].

Assuming a δ - Dirac pulse source, the temporal distribution of photons at distance $\rho = \sqrt{x^2 + y^2}$ from the injection point, for a laterally infinite slab of thickness s is described by the reflectance (Eq 1.11) and transmittance (Eq 1.12):

$$R(\rho, t) = -\frac{1}{2(4\pi Dv)^{3/2}t^{5/2}}e^{\left(\frac{-\rho^2}{4Dvt} - \mu_{av}t\right)} \times \sum_{m=-\infty}^{+\infty} \left[z_{3m}e^{\left(-\frac{z_{3m}^2}{4Dt}\right)} - z_{4m}e^{-\frac{z_{4m}^2}{4Dvt}} \right] \quad (1.11)$$

$$T(\rho, t) = -\frac{1}{2(4\pi Dv)^{3/2}t^{5/2}}e^{\left(\frac{-\rho^2}{4Dvt} - \mu_{av}t\right)} \times \sum_{m=-\infty}^{+\infty} \left[z_{1m}e^{\left(-\frac{z_{1m}^2}{4Dt}\right)} - z_{2m}e^{-\frac{z_{2m}^2}{4Dvt}} \right] \quad (1.12)$$

where

$$\begin{cases} z_{1m} = (1 - 2m)s - 4mz_e - z_s \\ z_{2m} = (1 - 2m)s - (4m - 2)z_e + z_s \\ z_{3m} = -2ms - 4mz_e - z_s \\ z_{4m} = -2ms - (4m - 2)z_e + z_s \end{cases} \quad (1.13)$$

These quantities express the power per unit area that crosses the surface in a certain position. Here, $z_e = 2AD$ and $z_0 = (\mu'_s)^{-1}$. These equations can in practice be truncated to the first few terms since the with increasing m , the corresponding z_m (distance of the image source from the boundary) increases thereby making its contribution to the solution negligible for relatively short ρ, t .

Eq 1.10 can then be used to obtain the solution for the reflectance from a semi-infinite medium which can be considered as a limiting case of the slab geometry with the thickness s going to infinite. In this case, $z_{3m} = -z_s$ and $z_{4m} = 2z_e + z_s$, and the equation for reflectance is simplified as follow:

$$R(\rho, t) = -\frac{1}{2(4\pi Dv)^{3/2}t^{5/2}}e^{\left(-\frac{\rho^2}{4Dvt}-\mu_a vt\right)}x \times \left[z_0 e^{\left(-\frac{z_0^2}{4Dvt}\right)} - z_p e^{\left(-\frac{z_p^2}{4Dvt}\right)} \right] \quad (1.14)$$

1.6.2 Case2: Multilayered media

Here we briefly discuss the solution for TD-DE in a two-layered cylinder. A detailed description can be found elsewhere [39].

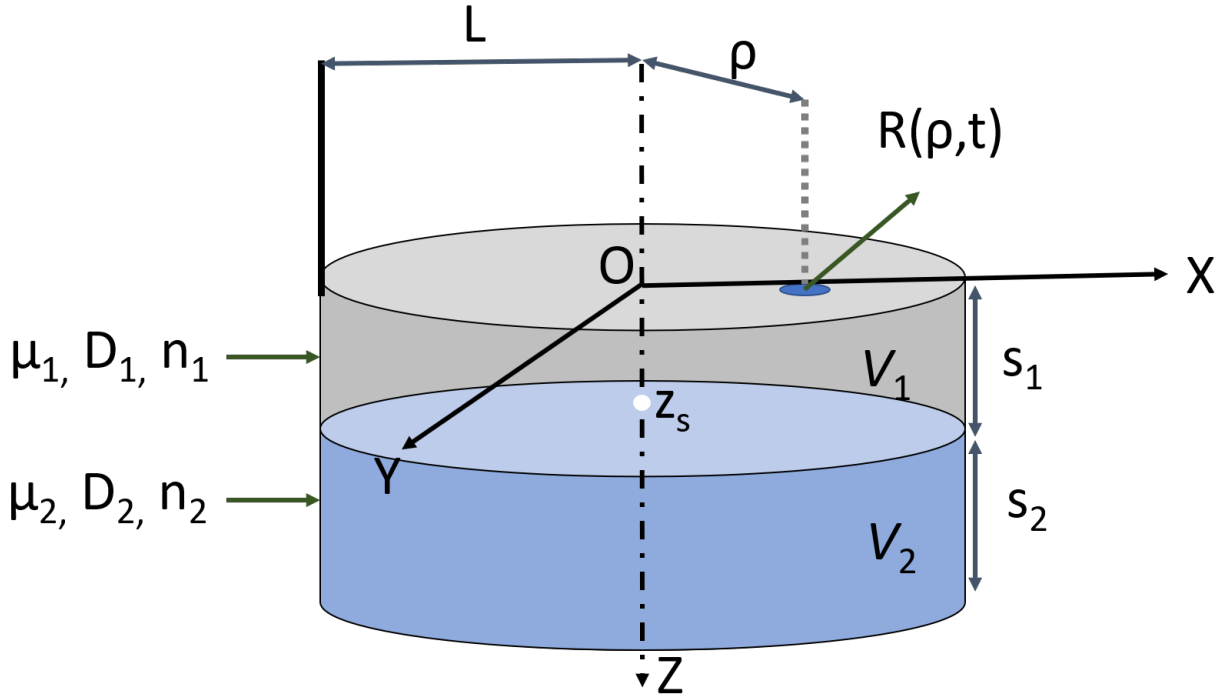


Figure 1.5: Schematic of the two layered cylinder described in the present model.

Consider a the two layer cylinder of radius L and volumes V_i as shown in Figure 1.5 divided into two regions of thickness s_1 and s_2 respectively. Each region is characterized by $\mu_{a,i}$, D_i and n_i ($i = 1, 2$) that are the absorption, diffusion coefficients and the refractive index respectively.

With a point-like source located in $\vec{r} = (0, 0, z_s)$ as:

$$q(\vec{r}, t) = \delta(\vec{r} - \vec{r}_s) \delta(t) \quad (1.15)$$

the diffusion equation for the inhomogeneous medium becomes:

$$\left[\frac{1}{v} \frac{\partial}{\partial t} - \nabla(D(\vec{r})\nabla) + \mu_a \right] \Phi(\vec{r}, t) = \delta(\vec{r} - \vec{r}_s) \delta(t) \quad (1.16)$$

The initial and boundary value problem is then formulated in terms of $\Phi_1(\vec{r}, t)$ and $\Phi_2(\vec{r}, t)$ for the two layers, as:

$$\begin{cases} \left[\frac{\partial}{v_1 \partial t} - D_1 \nabla^2 + \mu_{a1} \right] \Phi_1(\vec{r}, t) = 0 & t > 0, \quad 0 \leq z < s_1 \\ \left[\frac{\partial}{v_2 \partial t} - D_2 \nabla^2 + \mu_{a2} \right] \Phi_2(\vec{r}, t) = 0 & t > 0, \quad s_1 \leq z \leq s_1 + s_2 \end{cases} \quad (1.17)$$

and

$$\Phi_1(\vec{r}, t = 0) = v_1 \delta(\vec{r} - \vec{r}_s^{\lambda}) \quad (1.18)$$

z_{1e} and z_{2e} are the extrapolated distances at the surface $z = 0$ and at $z = s_1 + s_2$ corresponding to the surface of separation of the two regions (EBC). On the other hand, $\angle BC$ were used on the lateral surfaces of the cylinder. The injection in this case is assumed to be from the first layer.

The fluence rate is defined for each layer as an eigenfunction expansion $\Phi(\vec{r}, t)$ [39]

$$\begin{cases} \Phi_1(\vec{r}, t) = \sum_{l,n=1}^{\infty} \alpha_{ln} \xi_{ln1}(\vec{r}) e^{-\lambda_{ln} t} & t > 0, \quad 0 \leq z \leq s_1 \\ \Phi_2(\vec{r}, t) = \sum_{l,n=1}^{\infty} \alpha_{ln} \xi_{ln2}(\vec{r}) e^{-\lambda_{ln} t} & t > 0, \quad s_1 \leq z \leq s_1 + s_2 \end{cases} \quad (1.19)$$

The mathematics behind the conditions defining the eigenfunctions $\xi_{1ln}(\vec{r})$ and the solutions necessary to obtain their coefficients α_{ln} and λ_{ln} is beyond the scope of this thesis and can be found in the following reference [39]. However, the following factors must be taken into consideration to obtain the solution for $\Phi(\vec{r}, t)$. To ensure that the boundary condition at the interface between the two layers is satisfied in Eq 1.19 the temporal evolution of Φ_1 and Φ_2 needs to be the same (i.e. same coefficients α_{ln} and λ_{ln}). The sum is expressed over two independent indexes, l and n , because the solution depends on the independent parameters (ρ, z) . Transformation into cylindrical coordinates reduces the number of variables in the problem. Finally, the boundary condition at $z = s_1$ must be defined taking into account the discontinuity of the refractive index at which point the problem can be solved to get $\Phi(\vec{r}, t)$:

$$\Phi(\vec{r}, t) = \begin{cases} \sum_{l,n=1}^{\infty} v_1^2 J_0(K_{\rho l}) \sin(K_{z_{ln1}} + \gamma_{ln1}) \times \\ \times \sin^* \left(K_{z_{ln1}} z_s + \gamma_{ln1} \frac{e^{-(K_{ln1}^2 D_1 + \mu_{a1}) v_1 t}}{N_{ln}^2} \right) \\ \text{for } 0 \leq z < s_1 \\ \sum_{l,n=1}^{\infty} v_1^2 J_0(K_{\rho l}) b_{ln2} \sin(K_{z_{ln2}} + \gamma_{ln2}) \times \\ \times \sin^* \left(K_{z_{ln2}} z_s + \gamma_{ln2} \frac{e^{-(K_{ln2}^2 D_1 + \mu_{a2}) v_2 t}}{N_{ln}^2 N_n^2} \right) \\ \text{for } s_1 \leq z < s_1 + s_2 \end{cases} \quad (1.20)$$

Where J_0 is the Bessel function of the first kind of order zero; b_{ln2} is:

$$b_{ln2} = \frac{\sin(K_{z_{ln1}} s_1 + \gamma_{ln1})}{\sin(K_{z_{ln2}} s_1 + \gamma_{ln1})} \left(\frac{n_2}{n_1} \right)^2 = -\frac{\sin[K_{z_{ln1}} (s_1 + z_{e1})]}{\sin[K_{z_{ln2}} (s_2 + z_{e2})]} \left(\frac{n_2}{n_1} \right)^2 \quad (1.21)$$

The coefficients $K_{\rho l}$, $K_{z_{ln1}}$, $K_{z_{ln2}}$, K_{ln1} and K_{ln2} are obtained imposing the boundary conditions as in Equations 1.17 while N_{ln} is defined as:

1.7. Stochastic (Monte Carlo based) Solutions of the RTE in Time Domain:

$$N_{ln}^2 = v_1 \int_{v_{e1}} \xi_{ln1}(\vec{r}) \xi_{ln1}^*(\vec{r}) d\vec{r} + v_2 \int_{v_{e2}} \xi_{ln2}(\vec{r}) \xi_{ln2}^*(\vec{r}) d\vec{r} \quad (1.22)$$

and γ_{1ln} and γ_{2ln} are defined by:

$$\begin{cases} \gamma_{1ln} = K_{z1ln} z_{1e} \\ \gamma_{2ln} = -K_{z2ln} (s_1 + s_2 + z_{2e}) \end{cases} \quad (1.23)$$

Finally the reflectance and transmittance is obtained from the expression for the fluence 1.6.2 using the hybrid extrapolated boundary partial current (EBPC) [41] approach:

$$\begin{aligned} R(\rho, t) &= \frac{\Phi(\rho, z = 0, t)}{2A} \\ T(\rho, t) &= \frac{\Phi(\rho, z = s_1 + s_2, t)}{2A} \end{aligned} \quad (1.24)$$

and the Fick's law of Eq 1.8 is used to calculate the outgoing flux. The discontinuity of refractive index at the surface $z = s_1$ leads to a discontinuity in the solution of $\Phi_1(\vec{r}, t)$ and its derivatives.

1.7 Stochastic (Monte Carlo based) Solutions of the RTE in Time Domain:

While this thesis relies mainly on the analytical solutions of DE, certain applications, especially those with very low scattering probabilities warrant the use of a more reliable and accurate method. In these cases, we utilize probabilistic methods like Monte Carlo (MC) modelling to solve the RTE. This section briefly discusses the necessary workflow to achieve this. Since this technique reverts back to the RTE, there is no need for the assumptions conjectured for the DE. The accuracy in this case is limited only by the intrinsic stochastic nature of the method. Table 1.1 presents the variables, their corresponding probability distribution functions (PDFs) used for a typical MC simulations.

	Influenced by	Probability Distribution Function
Scattering step (l)	$(\mu_t = \mu_a + \mu_s)$	$P(l) = 1 - \exp(-\mu_t l)$
Scattering Phase($p(\theta)$)	g	$p(\theta) = \frac{1}{4\pi} \frac{1-g^2}{(1+g^2-2g \cos \theta)^{3/2}}$

Table 1.1: Variables and their corresponding Probability Distributions used typically in MC based modelling

Other factors like the effect of absorption on the conservation of radiant energy and the effect of boundary on the survival of the photon are factors that still need further consideration and are discussed in detail elsewhere [42]. An inversion procedure then maps the PDFs onto a uniform distribution between $[0,1]$. A pseudo-random number ξ generated in the range $[0,1]$ can then be substituted in inverse distribution to decide the step size and direction of photon propagation until it is either absorbed or reaches

a boundary where Fresnel's law and Snell's Law decide the probability of its refraction, reflection or transmission. Large number of photons ($>10^6$) are modelled in this fashion and the pathlength information of the detected photons are tabulated. This information is then converted into photon arrival times using the formula $t = l_{tot}/v$ (v = speed of light in diffusive media and l_{tot} is the pathlength) and plotted as a histogram to reconstruct the *temporal point spread function* (TPSF). The temporal resolution is determined by the bin size of the histogram.

Even though it provides a more accurate result in general, MC technique, suffers from a setback as a consequence of the central limit theorem. In brief, higher the number of received photons the better the outcome of MC simulation, making it a computational intense and time consuming process. In the simulations used in this dissertation, a standard count rate of 1 million photons was used to reconstruct the TPSF. Also, the launched photons are considered with zero absorption, later the absorption is added separately by obeying the Eq. 1.6.

1.8 Optical Properties (μ_a, μ_s) Estimation

Time resolved measurements performed using the instrumentation discussed in 1.4.3 provides the Reflectance/ Transmittance temporal distribution of the photons. The models discussed in the last two sections need then to be applied to these data to extract the optical properties of the sample. Known as the *inversion* procedure, this process involves fitting the analytical solution to the experimental data.

In practice, the real source is neither an isotropic nor a delta-function thus the convolution of the theoretical curve with the Instrumental Response Function (IRF) is carried out to take into account the temporal width of the light source injected, the response time of the detector and the dispersion in optical fibers. Since the DA does not account for the early photons, the fitting procedure is performed excluding the points of the time-resolved curve with a number of counts lower than 80% of the peak value on the rising edge. Furthermore, to avoid noise or background related distortions the tail of the curve is cut at 1% of the peak value. The freely varying parameters that are used in this fitting routine are (μ_a, μ'_s). The Levenberg-Marquardt algorithm for non-linear minimization has been shown to be the ideal optimization tool [43] and is hence the algorithm of choice. Fig. 1.6 shows an example fitting window from the in-house built fitting software employed frequently in this work.

In cases where the diffusion approximation is on the verge of breakdown (for example: high absorption and low scattering media, thin samples measured in transmittance), it would be wiser to use the numerical Monte Carlo method [44]. Here the first step is to create a library of MC simulations at different scattering coefficients of interest and null absorption; a CUDA (Compute Unified Device Architecture) accelerated Monte Carlo code [45]. In particular, pivot simulations are obtained simulating curves at different scattering values according to a geometric progression, this way we have a denser sampling for low scattering values and a less dense sampling for higher scattering values. This base set of simulations is then linearly interpolated to obtain the results for arbitrary reduced scattering with null absorption. Finally, multiplication with the factor $\exp(-\mu_a vt)$ where v is the speed of light, accounts for the absorption. Then convolution with IRF followed by Levenberg-Marquardt optimization is performed like the

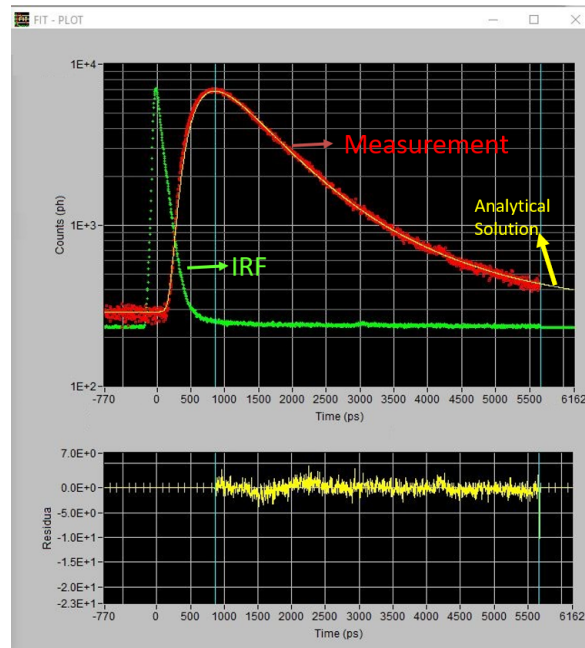


Figure 1.6: A typical example of fit. The residual at each fitted point is shown below the curves which can be used to manually check the goodness of the fit.

case with the analytical solution.

Apart from optical properties a third variable can also be considered as a free varying parameter in the fit, that is the time shift between the reference and the data. This factor is usually not set as a free fitting parameter, but is rather fixed to an optimum value, found fitting the shift together with the absorption and scattering coefficients for a sample with the lowest absorption. This procedure helps to compensate for the inadequacy of standard diffusion at early times and to account for eventual temporal drifts due to misalignment or thermal effects. This process is repeated for the different wavelengths and the broadband spectra are obtained by plotting these values against their corresponding wavelengths. The fitting procedure in case of a multi-layered model is slightly more complicated, due to the increase in the number of freely varying parameters and will be discussed in the next chapter.

Broadband Multi-distance TD-DOS Instrumentation for Clinical Use

2.1 Introduction

Though TD Diffuse Optics, in theory, can provide information on a wide range of tissue chromophore concentrations and on the microstructure of the tissue, this dimension is hardly exploited in available commercial and clinical instruments. Most instrumentation and studies, both *in vivo* and otherwise, assume only oxy and deoxy hemoglobin as the only absorbers due to usage of limited number of wavelengths. Broadband instruments, like the one discussed in this chapter, can effectively quantify other tissue constituents that are of clinical interest. Lipid, collagen and water are some of the key constituents of tissue that exhibit particular changes in the wavelength region around $1\ \mu\text{m}$. Recently other chromophores like tyrosine, thyroglobulin and iodine have been shown to be [46] important absorbers in this wavelength range and were used for the non-invasive monitoring of the human thyroid. However, the existing silicon based detectors have very low quantum efficiency in this wavelength region and hence are not the ideal choice for this. Another challenge arises from the fact that pulsed light sources covering broad wavelength range are usually expensive and bulky. Moreover, lack of suitable technologies for wavelength separation causes further problems in this endeavour. Carrying out clinical measurements *in vivo* further complicates the issue. The instrument of choice needs to be portable, robust, easy to use, well automated and safe to handle. All these parameters were taken into account while designing the broadband, multi-distance, time domain, diffuse optical spectrometer.

One key upgrade in this system in comparison to previous embodiments of broadband diffuse optical instruments [47] is its ability to automatically perform *multi-distance* measurements. This feature of the instrument is particularly interesting when dealing

with samples that are layered in nature. Some examples in this direction would be muscle tissue lying underneath a superficial fat layer[48] or in the case of human forehead with compartments like scalp, skull and brain[49]. Many layered models (such as the one discussed in 1.6.2) have been developed to handle precisely these situations. However, it has been demonstrated that having multi-distance measurements improves the accuracy of such models[50]. Depending upon the source-detector separation each of these multi-distance measurements predominantly probes a particular depth, thereby increasing the information content available to the multi-layered model regarding each of the individual layers. In this way, multi-distance measurements improve the accuracy of the retrieved optical properties of the different layers in the sample.

2.2 Design and Characteristics of Instrument

2.2.1 Optical Layout of the instrument

Fig.2.1 depicts the schematic of the portable multi-distance broadband time resolved diffuse optical spectrometer. For ease of understanding, the layout is broken into three arms.

Source arm: The source arm comprises of a supercontinuum laser source (SC450, Fianium, UK) based on photonic crystal fibers providing the broadband pulses. An F2 glass Pellin Broca prism (B.Halle Nachfl., Germany) is used to disperse the source and the minimally deviated wavelength is coupled into an optical fiber (with a core diameter of 50 μm) using a lens ($f=150$ mm). Wavelength tuning is achieved by rotating the prism. The rotation is completely automatized using an automated rotation stage (PI, USA). The fiber laser runs at repetition rate of 60MHz. The spectral bandwidth of the source ranges from 3 nm at 600 nm to 9 nm at 1100 nm which is a result of nonlinear dispersion of the prism. At this level, the source is further split into two arms in the ratio 90 : 10 using a fiber beamsplitter, the former is used as the source for measurements on the sample while the latter is used in the reference arm, which will be discussed shortly. To avoid saturation of detector, variable circular attenuation filters (NDC-50C-2, Thorlabs, Germany) are employed in both the arms. The source fiber is then provided as the input to a 1x4 fiber optic switch (Leoni, Germany) was employed to create 3 separate source points (using three out of the four outputs of the switch) to facilitate multi-distance measurements. These output fibers are then housed in the probe as shown in the figure. While most applications in this work employ 1,2 and 3 cm as the standard inter-fiber distances for multi-distance measurement, these values can be varied depending upon the design of the fiber hosting probe. This concludes the description on the source arm of the instrument.

Detection arm: Light diffusely reflected by the sample, is then collected by a detector fiber bundle made of two 1-mm diameter step-index fibers bundled together on the sample side and coupled to two different detectors. The detectors were chosen in such a way as to achieve a high and rather flat bandwidth over the broad range of wavelengths. While most applications discussed here utilize only the wavelength region of 600-1100nm, this instrument in theory is capable of a rather good responsivity all the way up to 1300nm. The two detectors chosen for this purpose are 1) A silicon photomultiplier SiPM (S10362-11-050C, Hamamatsu, Japan) with home-made front-end electronics[51], and 2) an InGaAs photomultiplier(PMT) (H10330A-45, Hamamatsu,

2.3. Novel Features:

Japan). The two detectors together have a good responsivity/quantum efficiency over the wavelength region (600-1100nm). The SiPM has a very good quantum yield from around 600 to 1000nm beyond which it gradually tapers while the PMT is functional from around 950nm all the way up to 1300nm. The signal from the detectors was processed by two time-correlated single photon counting (TCSPC) boards (SPC-130, Becker & Hickl, Germany) to produce the temporal point spread functions (TPSFs) displayed and stored on the Industrial PC.

Reference arm: A reference arm couples the source light at the selected wavelength directly to the detectors shifted in time so as to not interfere with the sample response. This enables a continuous monitoring of the instrument response and for compensating any temporal distortions or thermal drifts affecting the signal.

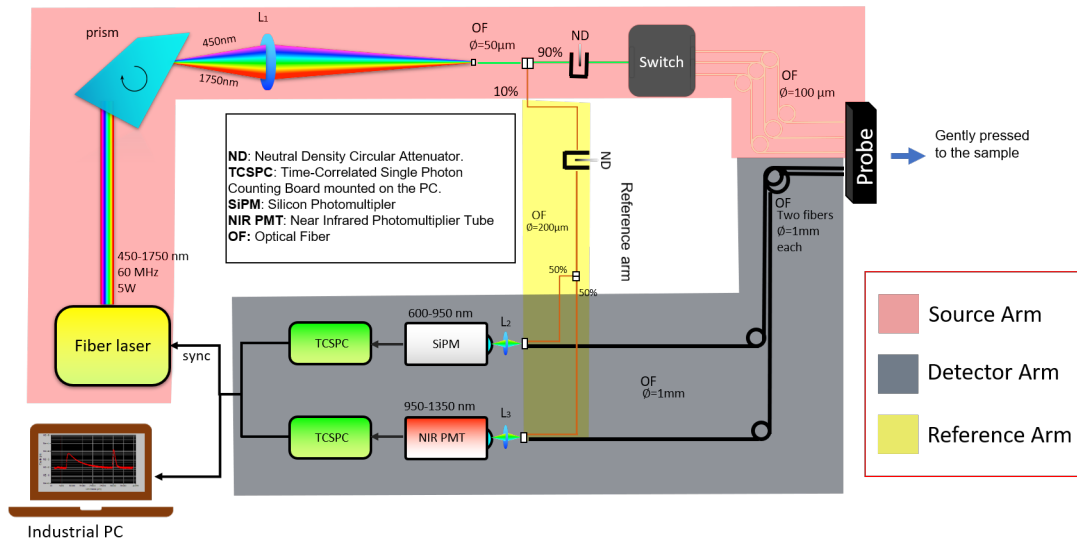


Figure 2.1: Schematic of the instrument. Legend on the bottom right represents the three arms of the instrument.

The scanning of wavelengths and the switching of the injection fibers (leading to different inter-fiber distances) is performed sequentially and not parallelly. Simply put, the $\rho = 1$ cm measurement is performed first for all the wavelengths in the range and then the source *switches* to the next injection fiber with the help of the fiber optic switch and proceeds to measure all the wavelengths at the new inter-fiber distance and so on. A typical measurement performed from 600 to 1100nm with a step size of 10nm for the three inter-fiber distances (i.e. $51 \lambda \times 3\rho = 153$ measurements) takes a measurement time of a little less than 5 minutes.

2.3 Novel Features:

The entire operation of the instrument, from the rotation of the prism and the circular attenuator, to the switching between the different injection points for the multi-distance measurement is completely automated using proprietary software developed using the LabWindows/CVI environment (National Instruments, USA). This is particular relevant for a broadband instrument, since the large number of moving parts could be handled erroneously if left to manual supervision. Apart from this, the system boasts of the

following novel features introduced during the course of this Ph.D.

Fiber Specifications: The need to be operational in a clinical scenario imposes certain restrictions on the nature and length of the different fibers used in the instrument. The three injection fibers and the collection fiber bundle need to be sufficiently long so as to be easily adaptable to the bed-side environment of the clinics. All the fibers on the source side of the instruments should be chosen so as to reduce the effective broadening of the pulse due to material dispersion. The detection fibers, on the other hand, must be chosen so as to maximize the collection efficiency by providing the highest possible field of acceptance with a tolerable amount of temporal dispersion. As mentioned earlier, the reference pulse needs to arrive at a specific time interval after the signal which is directly dependent on the length of the fibers in the reference arm. The multiple round trips that the signal and reference pulses undergo could lead to the formation of unwanted reflections in the time window of interest which could propagate with further round trips leading to distortion in the TPSFs or other inaccuracies.

# of fibers	Type	Core diameter	NA	Fiber length	Connectors	Position
3	Graded	100 μ m	0.29	1.5m	SMA and SMA	Source(from switch to probe)
2	Step	1mm	0.39	1.5m	SMA and SMA	Detection
2	Step	200 μ m	0.39	2m	FC/PC	Reference

Table 2.1: Specifications of the different fibers used for the instrument. SMA = SubMiniature version A, FC/PC = Fiber Connectors/Physical Contact and NA = Numerical Aperture

Table 2.1 summarizes the lengths and key characteristics of the different fibers used in this instrument. To solve the problem of reflections mentioned above simulations were performed to understand theoretically the influence of a selected set of fiber lengths on the round trip reflection generation and build up. PSpice A/D (Cadence Design Systems, USA), an Electronic Circuit Optimization and Simulation software was used for this purpose. This software is often used to understand the broadening and interference occurring when pulsed electronic signals from multiple transmission lines are combined. This situation can be extended to the problem of our instrument design by replacing the multiple transmission lines with the optical fibers from the different arms of our instrument and the input electronic pulse with the optical pulses generated in our instrument. Generating multiple (>10) pulses with a time gap equal to the repetition rate of the laser we could then study the magnitude and location of occurrence of any unwanted reflection/ interference between the two pulses. One minor adjustment required in this scenario is that the transmission lines in the simulation are defined by their transmission delay rather than their length, this can however be calculated in our case by dividing the length of the fiber with the speed of light in the medium. Multiple choices of fiber lengths were simulated for this purpose and the values tabulated in Table 2.1 were chosen to be the most ideal for this purpose over the entire wavelength range. Fig.2.2 shows the output of the simulations for the length of fibers presented in the Table 2.1 at the extreme operational wavelengths of our instrument. The simulations suggests that the area between the signal and reference peak is devoid of any major reflections or other unwanted signals. Also the nearest reflections of significant magnitude (1% of the signal peak) on either sides of the signal and reference peaks are at least 1.5ns apart. This is crucial since this part of the window is utilized to compute

the average background value that needs to be subtracted to obtain a better signal to noise ratio.

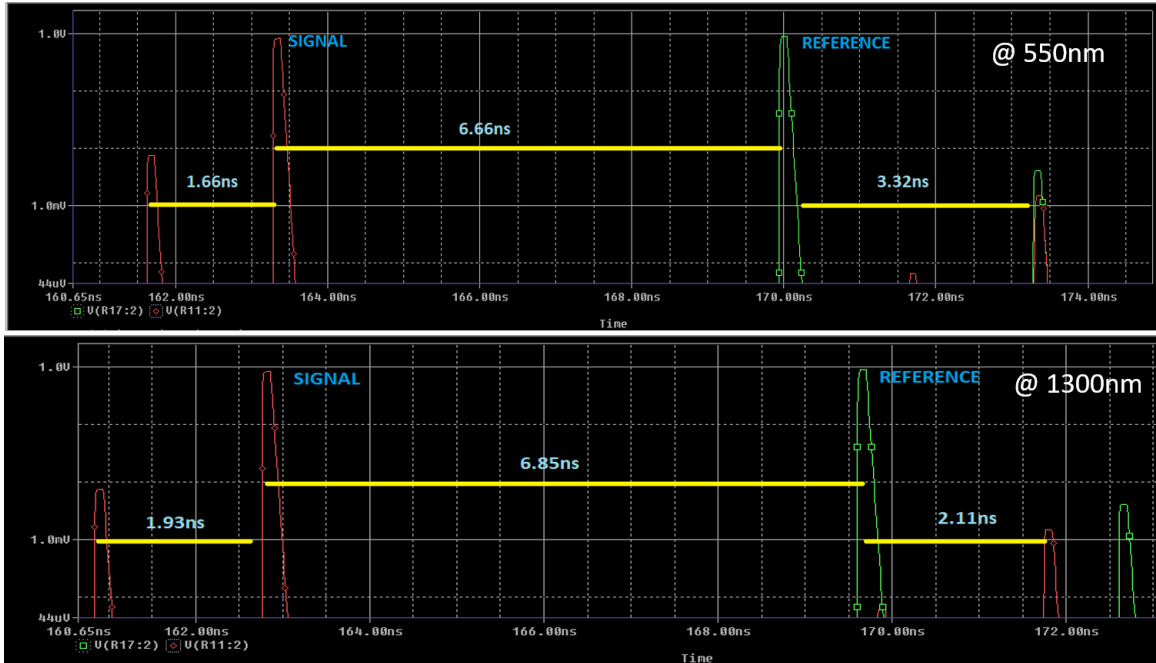


Figure 2.2: Simulated reflection profiles of the signal and reference at 550nm (above) and 1300nm (below) for the lengths of optical fibers presented in Table 2.1.

The refractive index profile of the fibers were chosen to reduce the broadening of the pulse. Graded index fibers in general have lower modal dispersion and are less lossy in comparison to step index fiber and are hence best suited for the source arm. However, since they are mainly used in communication, graded index fibers are usually manufactured with low core diameter (below $100\mu\text{m}$). Hence, the detection fiber which need good collection efficiency have a larger core diameter (1mm) and higher numerical aperture (0.39) and a step index profile.

Correction for Drift and Distortion: The stability of the instrument response function (IRF) is crucial for the stability and reproducibility of the estimated optical properties. Relatively minute drift in the IRF can lead to considerable variations in the estimated optical properties. Moreover, the clinical environment can be far more challenging compared to a controlled settings as that of a laboratory. Continuous acquisition of the reference signal using the reference arm is pivotal in tackling the inaccuracies that could arise due to these temporal drifts or distortion in the TPSF. Fig 2.3 shows the typical set of measured TPSFs (on a calibration phantom with optical properties of 0.1 cm^{-1} in absorption and 10 cm^{-1} in reduced scattering at 800nm) acquired for a particular wavelength (800nm) at the three inter-fiber distances on a phantom. The sharp peaks present at the extreme right of the time window correspond to the reference peaks.

Fig 2.4 shows a sideways view of the instrument completely assembled within a portable rack on wheels. The individual compartments of the rack are labelled. The figure also shows the fiber hosting probe and the dedicated phantom box used for the instrument. A flexible metallic support attached to the bundle of fibers at the output

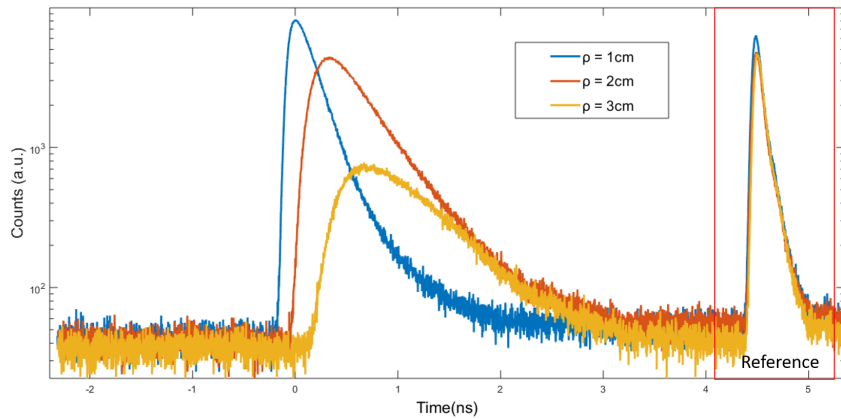
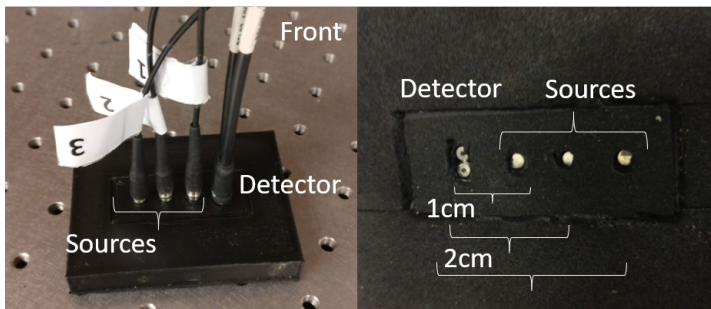


Figure 2.3: The reference arm used to correct for any unforeseen drift and distortion in the IRF (red box on the right). TPSFs correspond to phantom measurement at a particular wavelength (800nm) plotted for the three inter-fiber distances of 1,2 and 3cm

Fiber Hosting Probe



Calibrated Phantom

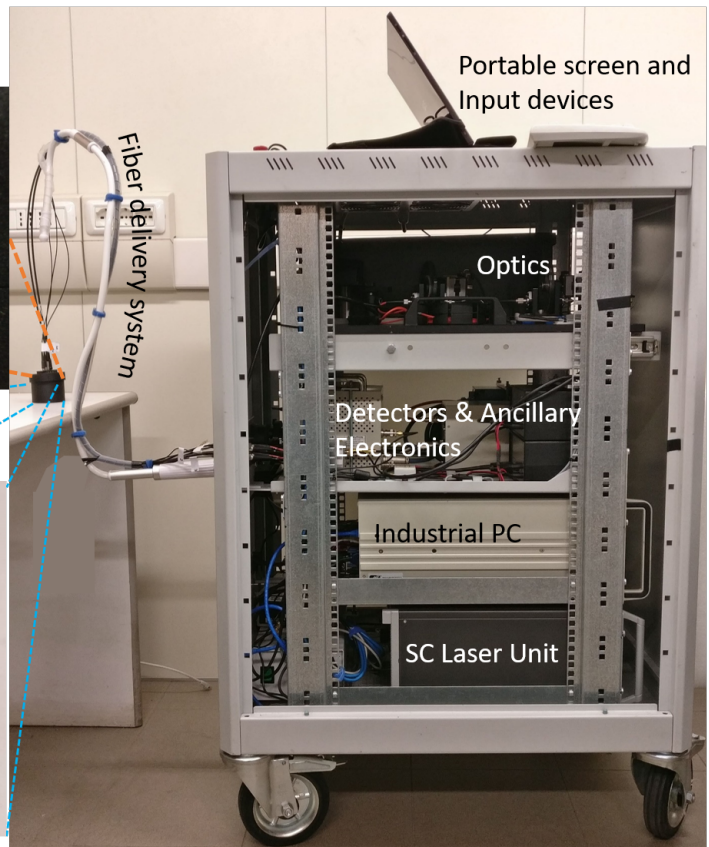
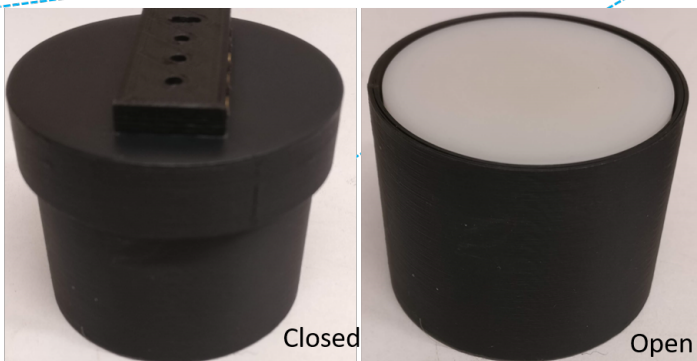


Figure 2.4: (right) Sideways view of the portable instrument developed for clinical measurement measuring a calibrated phantom with key regions demarcated. (left) Closer look at the calibrated phantom and the probe that hosts the fibers

ensures negligible pressure and a pliant delivery of the fibers, which is important in a clinical scenario. Also, the probe, the phantom and the automation software are

designed to be very intuitive to a relatively inexperienced user.

2.4 Characterization and Performance Assessment

Two well established protocols for photon migration instruments, specifically in the time domain, known as the MEDPHOT [52] and the basic instrument performance (BIP) **Wabnitz2014** protocol are generally considered to assess the performance of the system. While the BIP assesses the hardware and related parameters of the instrument the MEDPHOT is designed primarily to assess the performance of the instrument in retrieving the optical properties μ_a and μ'_s . The MEDPHOT considers the instrument along with the analysis technique used as a black box and the results are based entirely on the output μ_a and μ'_s .

The assessment of the instrument using the MEDPHOT protocol is presented here. This protocol is broadly divided into five assays/tests:

- **Accuracy:** the accuracy of estimating the absolute optical properties.
- **Linearity:** coupling or dependence of one optical property on the other.
- **Noise/Uncertainty:** uncertainty in the retrieval of optical properties.
- **Stability:** short and long term stability of the estimated optical properties.
- **Reproducibility:** comparison of optical properties on measurements performed on different days.

A set of 32 phantoms designed specifically for the MEDPHOT protocol were utilized to assess the above mentioned parameters. These phantoms were made of epoxy resin with different concentration of TiO_2 and black toner to simulate different values of μ_a and μ'_s in a controlled fashion. Fig 2.5.a shows the matrix arrangement of these 32 phantoms in increasing values of μ_a and μ'_s . The assessment was performed in reflectance geometry with the three inter-fiber distances of 1,2 and 3 cm, over the wavelength range of 600-1100 nm with 10 nm as step size.

2.4.1 Accuracy

The typical assessment of accuracy according to the MEDPHOT protocol involves the measurement of the 32 solid phantoms at a single wavelength and plotting them against the conventionally true value to understand the discrepancy/deviation from these standard values. However, the instrument under question being operable over the wide range of wavelengths (600:10:1100nm), would produce a 3 broadband spectra for μ_a and μ'_s as shown in Fig2.5(c,d) for each individual phantom (presented data is for the B2 phantom). A more interesting and useful assessment of the accuracy of the instrument would be one where it's ability to accurately retrieve the optical (more precisely absorption) spectrum of a known and well measured entity.

To this end, we use a liquid phantom made of intralipid (1% solid fraction in aqueous solution). This helps us to assess our system's performance in extracting water spectrum, which has significant variations in 600-1100 nm range. Fig.2.5.b compares

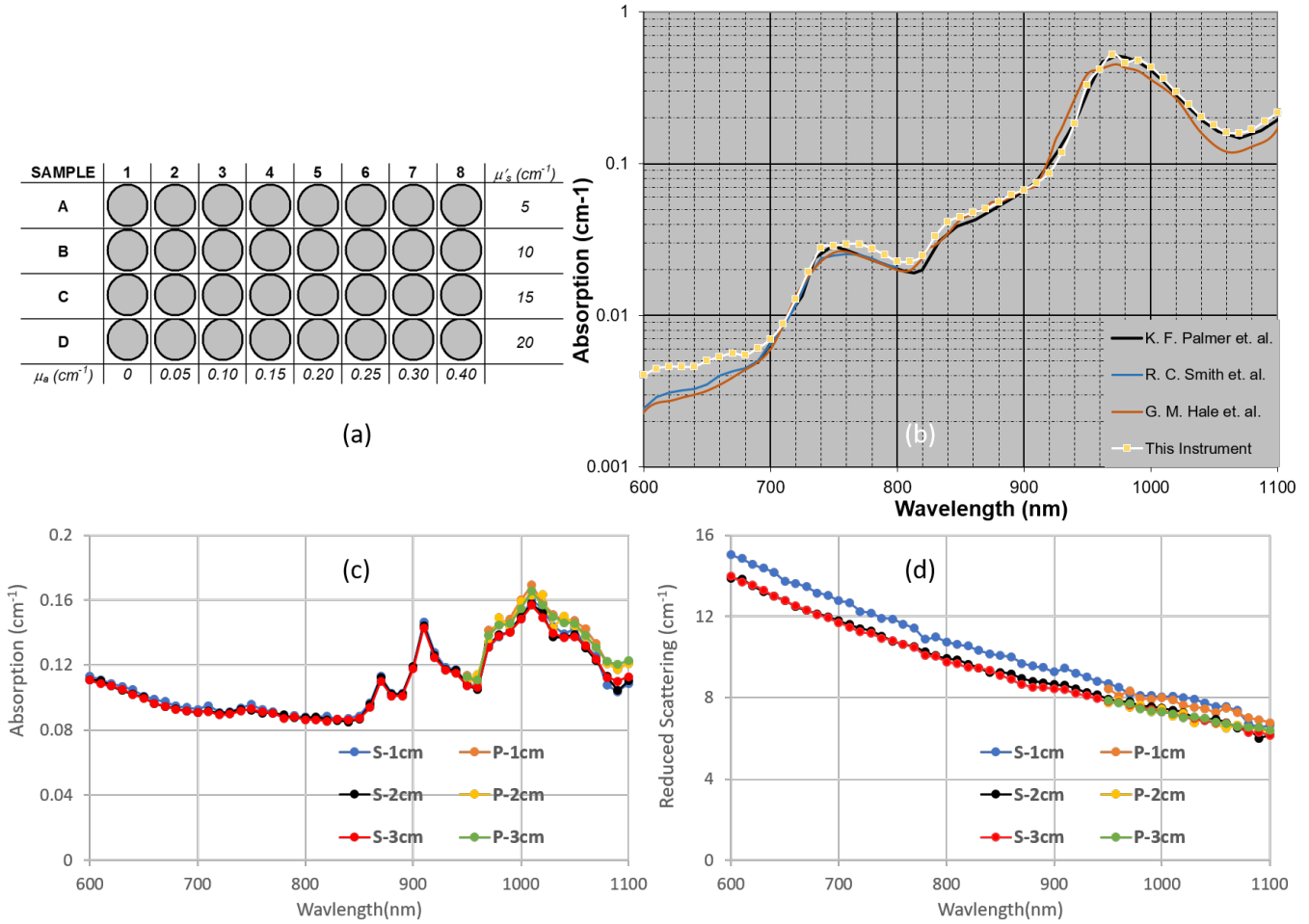


Figure 2.5: (a) The 32 phantoms measured as a part of the MEDPHOT protocol with their conventionally true values of the optical properties at $\lambda = 800nm$. (b) Absorption spectrum of pure water as measured by our instrument ($\rho = 2cm$) in comparison with [53]–[55] (c&d) Absorption and reduced scattering spectra of one of the 32 phantoms measured using this instrument (at the three inter-fiber distances). Here S stands for the response of the SiPM and P for the PMT detector.

our absorption spectrum (yellow squares) of water with the data available from literature [53]–[55]. Except for at very low values of absorption ($\mu_a < 0.004cm^{-1}$) the measurement from our instrument seems to be in agreement with the results from the other references. In the above mentioned spectra from the solid phantom (Fig 2.5(c,d)), since no depth heterogeneity is expected from the phantom the three spectra should, in principle, be identical. However, a subtle over estimation of the optical properties (more evidently the reduced scattering coefficient) is observed in the case of the $\rho = 1cm$ case. This can be attributed to the fact that for the diffusion approximation on which the analysis model depends on demands a proper dispersion or "diffusion" of the light in the medium. This may not be sufficiently achieved in some cases with the shortest inter-fiber distance. The figure plots the response from both the detectors in their relative ranges of operation. Here we see that the SiPM is operational and is in good agreement with the PMT all the way upto 1100nm. But the responsivity of the detector might hinder the operation for large values of absorption.

2.4.2 Linearity

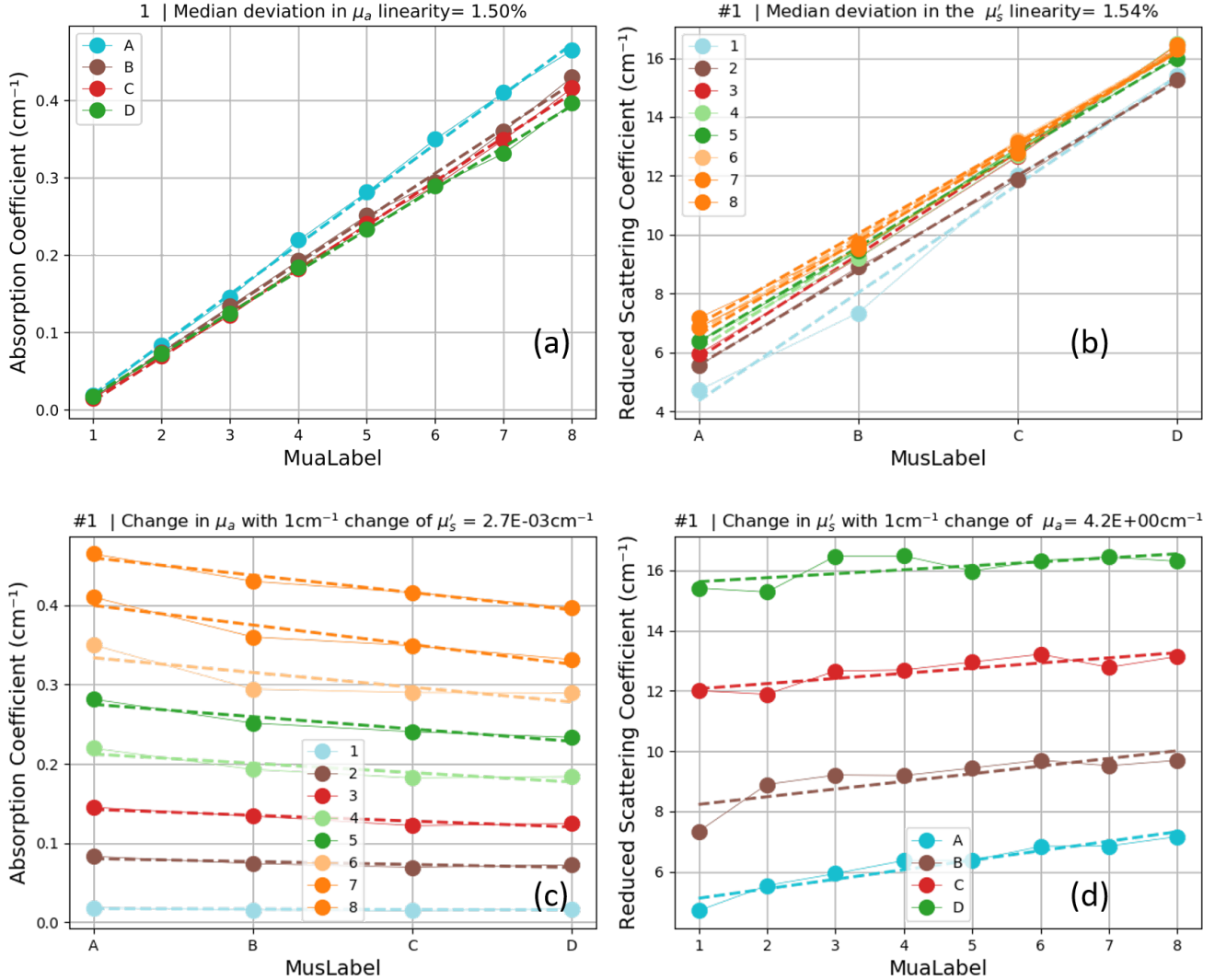


Figure 2.6: Results of Linearity tests at 800nm and $\rho = 2\text{cm}$

The results of linearity test are shown in Fig.2.6. These are all the results for a single wavelength and a single inter-fiber distance (800nm, 2cm). Fig.2.6 (a) and (b) plots, respectively, the measured μ_a and μ'_s against the conventional true values. Fig.2.6 (c) and (d) depict the coupling between the optical properties (μ_a, μ'_s). The title of each individual subplot quantitatively describes the result of the test. In case of linearity these numbers represent the median value of the deviation that each series experiences from their expected linearity (dashed line of the same color). For the coupling median value of the slope of the linear regression of the different lines (dashed lines of individual colors) is presented. Ideally, one would expect 0% median deviation for the linearity plots and 0 value of the slope of the lines in the coupling plots Fig.2.6 (c) and (d). As can be seen from their titles Fig.2.6 (c) and (d) the slope of the lines in these subplots is a measure of the dependence/change/coupling of one of the optical property (the one on

the y-axis) w.r.t a particular change in the other (the one on the x-axis). The values for our system are not very far from the ideal case scenario: about 1.5% for linearity and a $\Delta\mu_a = 0.002cm^{-1}$ for a $\Delta\mu'_s = 1cm^{-1}$ and a $\Delta\mu'_s = 0.4cm^{-1}$ for a $\Delta\mu_a = 0.1cm^{-1}$.

2.4.3 Noise/Uncertainty

The Noise test is based on very important statistical figure of merit known as the *coefficient of variation* (CV) which is defined as

$$CV = \frac{\rho(X)}{\langle X \rangle} \quad (2.1)$$

where $\rho(X)$ and $\langle X \rangle$ are, respectively, the standard deviation and mean of either μ_a or μ'_s .

To test the noise of the system, 20 repeated measurements are performed on the same phantom B2 with many different photon count rates. the choice of the B2 phantom is based on the fact that it ($\mu_a = 0.05cm^{-1}$, $\mu'_s = 10cm^{-1}$) is in close correspondence to the optical properties of biological tissues. The resultant coefficient of variation (CV) is plotted against its corresponding count rate in Fig.2.7. A decrease in CV is observed with increasing count rate, which is slightly different for the two optical properties. For a given count rate, μ'_s is found to have better CV than μ_a . As highlighted by the red box in the image to achieve a decent value of CV (around 1%), the system should be operated around 200 kcounts per second (kcps) or above.

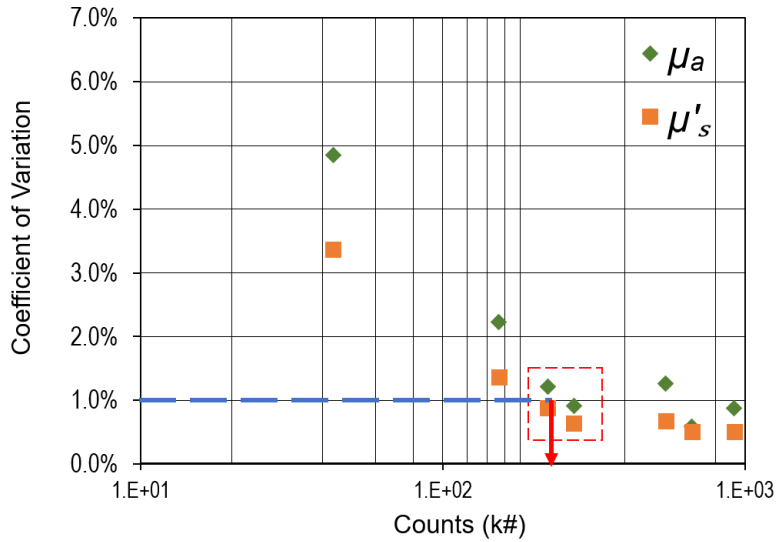


Figure 2.7: Coefficient of variation of optical properties (μ_a , μ'_s) at different photon count rates. The red arrow indicates the required number of photon counts to achieve a CV of 1%. As a general rule, the system was designed to operate at this count rate.

2.4.4 Stability

The stability of the system is assessed by running a long measurement on B2 phantom. This helps us understand the magnitude and the possible cause of any unwanted devia-

tions during long measurements, which are not unlikely in a clinical scenario. Fig.2.8 shows the stability measurement of both properties at five different wavelengths equispaced over the broad range for a time span of 1 hour. A straight line at every plotted wavelength elucidates the drift free nature of the system. The CV of the measurements was found to be under 2%. No considerable long term variation is observed and this must be attributed primarily to the presence of reference arm which ensures that the system adapts to any unwanted drifts over time.

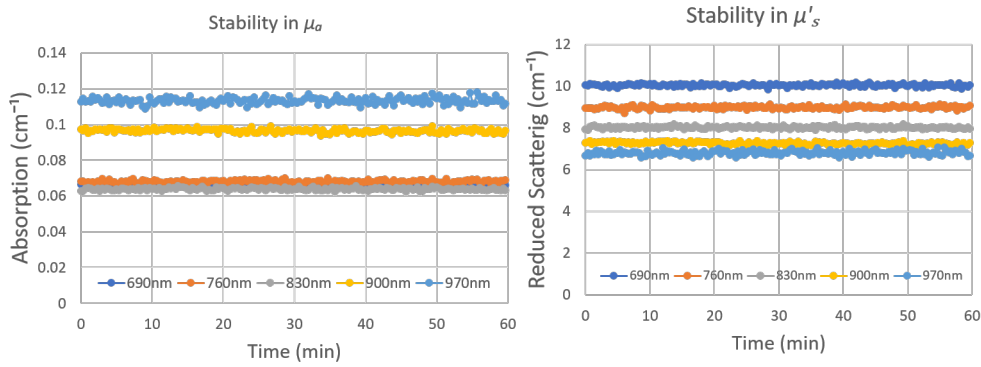


Figure 2.8: Stability of the instrument in retrieving optical properties over a time span of 1 hour long measurement

2.4.5 Reproducibility

To estimate Reproducibility the B2 phantom was measured under same experimental conditions (2 cm source-detector separation, reflectance geometry) on 10 different days. A CV of less than 4% is estimated for μ_a and μ'_s , guaranteeing the minimal uncertainties in the measured optical properties (μ_a, μ'_s) over long periods.

2.5 Clearance for clinical Use:

The electrical and optical safety of the instrument was ensured in conformity with the new EU Medical Device Regulation (EU MDR) [56] which is necessary before deploying it in clinics. The following outlines briefly the varied safety measures enacted in this direction

- **Electrical safety:** A medical grade isolating transformer guaranteed the protection of the system from unwanted fluctuations or spikes in power supply. Further, the high (220 V) and low (e.g. 12 V, 5V) supply is internally organized along different paths, following the best practice adopted in medical devices to avoid unwanted risk of electrical leakage. The transformer preceded a medical grade filter to further enhance the safety. The instrument was also subject to a professional electric isolation test using the vPad Electrical safety analyzer (Datrend Systems Inc., Canada) and was deemed safe to use in clinics.

- **Laser Safety:** The latest standard on laser safety (IEC 60825-1, “Safety of Laser Products”) was followed with regards to laser safety. In particular, regarding the limits on Maximum Permissible Exposure (MPE) for skin. The system is used in contact with the probe directly attached to the tissue under study. The maximum laser power exiting from the fiber in the whole 600-1300 nm range is <20 mW. Using a proper spacer the laser density impinging onto the tissue is regulated to be within the MPE for skin in the same range. The source emits a continuous train of pulses with a pulse width <50 ps and repetition rate of 60 MHz. Hence, both the single pulse and the whole pulse train conditions on the MPE need to be fulfilled, the latter being more restrictive than the former.
- **User Manual:** The system is equipped with a user manual, detailing the internal structure of the instrument, the controlling software and the operating procedures. Further, the manual specifies the requisite safety regulations and operational practices as described in the EU medical device directive.

Ethical Approval:All these measures ensure that the instrument is skin safe and allows for usage by clinicians and operators with minimal training. Approval was obtained from the Ethical Committee of Politecnico di Milano which allows the use of this instrumentation to perform *in vivo* measurements. The system also received a formal approval from the Ministry of Health for the use of the instrument to conduct *clinical trials*. The instrument will soon be deployed in a Hospital in Verona to non-invasively monitor the physical frailty in elderly obese.

2.6 Conclusions

In conclusion a portable time-domain diffuse optical spectrometer capable of performing relative multi-distance measurements over a broad range of wavelengths (600-1100nm) was developed and characterized. The instrument was validated with MED-PHOT and BIP protocols for accurate estimation of optical properties (μ_a , μ'_s) and, in turn, tissue composition and microscopic structure. The stability of system is found to be less than 2% (CV) and day to day reproducibility less than 4% (CV). The system received a formal approval for usage in clinics. This instrument forms an integral part of the rest of this work, as most of the results discussed in the forthcoming chapters are based on measurements performed using this instrument. The instrument will soon be enrolled in clinical trials to measure the *in-vivo* optical properties of the abdominal fat and muscle tissues in elderly obese subjects and monitor the variation of the properties with exercise and dietary interventions.

Retrieval of Absolute Optical Properties from Heterogeneous/Layered Diffusive Media

3.1 Introduction

As discussed in 1.6, conventionally, most studies assume biological media assume to be homogeneous with regard to optical properties. Thus, time resolved reflectance measurements performed in these cases are usually fitted to analytical solutions derived from the RTE for a homogeneous model in the semi infinite geometry. This is particularly inaccurate when the sample under investigation distinctly exhibits a layered structure and is even more erroneous when the layer of interest is not superficial but underneath. Pertinent examples in this regard are the case of monitoring cerebral oxygenation using non-invasive measurements on the forehead and monitoring blood parameters in muscle tissue. Extra cerebral layers including scalp and skull influence the measurements on brain while the dermal and fat layers effect measurement on muscle. To this end, analytical models based on DOS [57], [58] in general and, TR-DOS in particular, that consider the layered nature[49], [50], [59]–[65], of the sample have been developed by different research groups. While these models, in theory[48], [49], [60] utilize information from a single-distance time-resolved measurement to retrieve the properties of both the layers, most of the practical implementations use multi-distance measurements[50], [60], [62]–[65] to strengthen the information in particular for the deep layers.

Such models need thorough validation before they can be accepted and implemented into clinical devices. For this reason, most of the works mentioned above are tested against data generated by Monte-Carlo (MC) simulations[59], [65], actual measurements on tissue mimicking phantoms[59], [63], [65] and, in some cases, also on actual *in-vivo* measurements[48], [50], [66]. Also, most of these models are typically vali-

Chapter 3. Retrieval of Absolute Optical Properties from Heterogeneous/Layered Diffusive Media

dated using two to five wavelengths. However, no such validation studies of models for layered geometries exist on a broadband scale. The study closest to achieving this objective, however, would be [60] where broadband data is used to that reconstructs the absorber concentrations of layered media using multi-distance measurements and a homogeneous model. The assessment of such models over a wide wavelength window could be beneficial as 1) it adds an extra dimension over which the reliability of the model can be tested and also 2) it can provide a clearer picture of the decoupling between layers when the two layers have distinctive spectral features.

In this work we aim to test one such model proposed by Martelli et al. [50], that retrieves the optical properties from a **two-layered medium**. The model uses multi-distance, time-resolved, reflectance measurements to retrieve the optical properties of two-layered media. This model has been validated on some experimental data based on tissue mimicking liquid phantoms and some *in-vivo* data. Here, we re-validate this same model on a more robust broadband (600-1100nm) set of data generated from two different types of solid two-layered structures (i) based on phantoms made of silicone and (ii) based on different kinds of biological tissue *ex-vivo*. The model is also applied to some in-vivo data measured on the human forehead region. We also show the analysis of the same data-set using a standard model that assumes the sample to be homogeneous for comparison.

For each kind of two-layered structure, a preliminary analysis is performed using the standard model of the diffusion equation (assuming the sample to be homogeneous). The second level analysis is performed using the above-mentioned two-layered model. Finally, a spectral fitting procedure is performed to retrieve the concentration of the key absorbers of each two-layered structure.

3.2 Silicon Based Two-layer structures

Silicon based calibration phantoms designed in-house as a part different standardization protocols [52] and other collaborative projects [67] were used for the preparation of the two-layer structure of the first kind. The structure comprises of a silicone rubber-based (Sylgard) rectangular phantom (10cm x 10cm) as the top layer. This phantom was available in three thicknesses (s_0) 0.5cm, 1cm and 1.5cm thus permitting to simulate layered structures with varying top layer thickness (s_0). A 4.5 cm thick resin based cylindrical phantom (diameter = 10cm) was chosen for the bottom layer. Due to the relatively larger thickness and high absorption, the second layer could be considered as a semi-infinite medium optically. The absorption properties of both the materials were tuned by adding specific amounts of absorbers like carbon black and toner while the desired reduced scattering coefficient values were achieved using TiO_2 particles as scattering agents.

The instrumentation discussed in Chapter 2 was chosen for this study. Measurements were performed from 600 - 1100nm with a step size of 10nm in reflectance geometry for three inter-fiber distances ($\rho = 1, 2$ and 3 cm). As mentioned in the previous chapter, the entire measurement procedure was automated and thus the acquisition time per wavelength was under 1s.

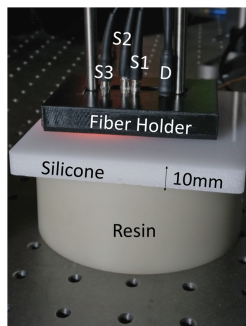


Figure 3.1: Setup for the relative multi-distance measurements on the silicon-based two-layered structure. The fiber hosting probe of the instrument discussed in the previous chapter can be seen on the top of the two-layered structure. The thickness of the top layer in this case is 1cm.

3.2.1 Analysis using Homogeneous Model

As a first step, the sample is assumed to be optically homogeneous and a homogeneous/semi infinite analysis model, (discussed in 1.6.1) is used. The boundary conditions, region of DTOF used for fitting and the optimization algorithm are discussed in Sec 1.8. A refractive index of 1.5 was used for the medium and 1 (air) was used as the refractive index of the external medium. Three spectra each for absorption and reduced scattering are obtained, corresponding to the three ρ . Fig. 3.2 shows the results using the homogeneous model. The reference spectra are plotted as a average of resultant optical properties from the multiple reflectance and transmittance measurements with the error bars representing the standard deviation.

The absorption spectra of both the materials (Top and Bottom in Fig. 3.2 (a,b and c)) show significant peaks at 905nm, a signature of silicon which forms the basis for both the phantoms. With regards to reduced scattering coefficient (Top and Bottom in Fig. 3.2 (d,e and f)) no distinctive features are observed apart from the expected power law dependence with wavelength.

The absorption coefficient values at the three ρ lie between the reference absorption coefficients of the two layers over the entire wavelength range. It can be clearly seen that with increasing ρ the absorption coefficient spectrum tends to move closer to the true bottom layer spectrum. For the top layer thickness of 0.5cm irrespective of the ρ the absorption spectra is primarily influenced by the bottom layer. This justifies the usage of this model as an approximate version even in the case of evidently layered media. However, there is a clear influence of the thickness of the top layer on the retrieved absorption spectra for the other two top layer thicknesses. This is best observed for a top layer thickness of 1.5cm where even at the largest ρ the absorption is heavily influenced by the top layer, both in terms of magnitude and spectral features. Reduced scattering spectra at all SD separations for both structures seem to be predominantly influenced by the top layer in absolute value.

3.2.2 Analysis using Layered Model

The retrieved absorption and reduced scattering coefficient spectra of the two layers using the two-layered solution of the DE (sec 1.6.2) are presented in Fig. 3.3, Fig.

Chapter 3. Retrieval of Absolute Optical Properties from Heterogeneous/Layered Diffusive Media

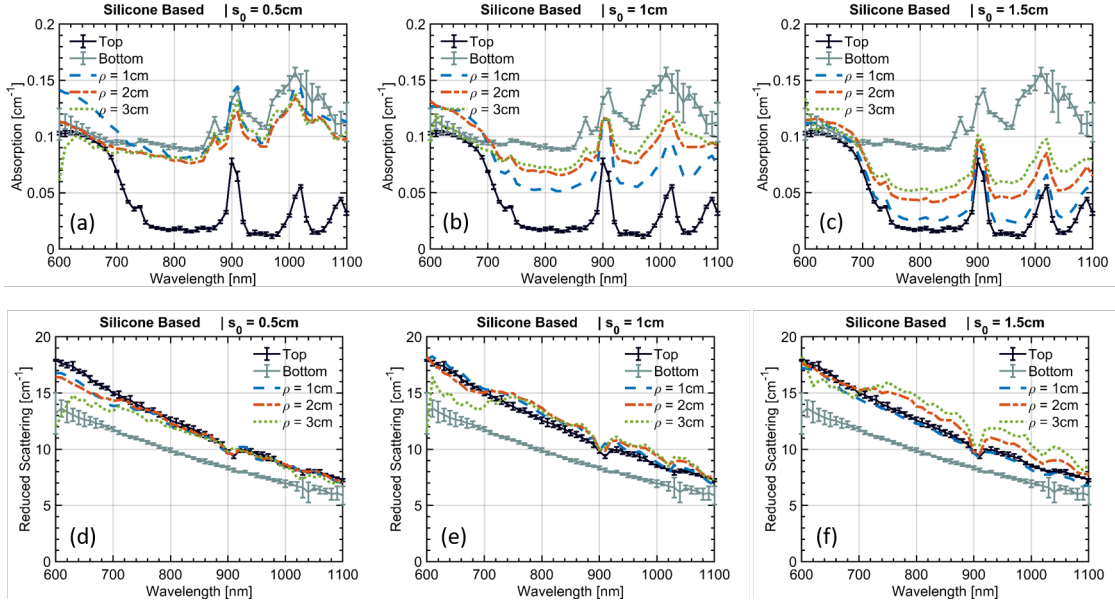


Figure 3.2: The absorption and reduced scattering spectra of the two layer structures at the three ρ analysed using a homogeneous or semi-infinite model. The reference optical properties of the two layers are provided with error bars representing the standard deviation over measurements at different ρ and in different geometries. The thickness of the top layer (s_0) is mentioned in the title of each subplot.

3.4 and Fig. 3.5 (for the three different top layer thicknesses of 0.5, 1 and 1.5cm respectively). The refractive indices were assumed to be 1.48 for the silicone and 1.55 for the resin layer respectively. As a first step the model was applied considering all the five important parameters of the fit, namely the optical properties of the top layer (μ_{a0}, μ'_{s0}), the optical properties of the bottom layer (μ_{a1}, μ'_{s1}) and the thickness of the top layer s_0 to be freely varying. The analysis was also performed with the thickness of the top layer (s_0) fixed to it's actual value for comparison.

At the very outset, it is clear that the layered model does a very good job in decoupling the optical properties of the two layer and more importantly is more reliable than the conventional homogeneous model. Amongst the four parameters related to the optical properties of the two layers, μ'_{s0} seems to be the parameter that is retrieved with extremely good accuracy. both in terms of spectral shape and absolute value. μ_{a0} is the parameter that closely follows, where the retrieval is considerably accurate. The configuration with the least top layer thickness (Fig. 3.3) sees the most inaccurate retrieval of this parameter. This could be due to the relatively small thickness (0.5cm), which is not a major concern if the parameter of interest is the optical property of the bottom layer. Moreover, as seen in the previous figure, at such low thicknesses the homogeneous approximation is reasonable. The absorption of the bottom layer, μ_{a1} , which is usually the most valuable parameter is retrieved with good accuracy for most of the spectral region. Finally, the μ'_{s1} is the parameter that is recovered with the least accuracy. The parameter undergoes drastic variations from the actual, expected values and for most practical purposes can be considered to be devoid of any useful information. On the plus side, this parameter also shows negligible influence on the retrieval of the other properties. Fixing this parameter to a known value, such as, that retrieved

3.2. Silicon Based Two-layer structures

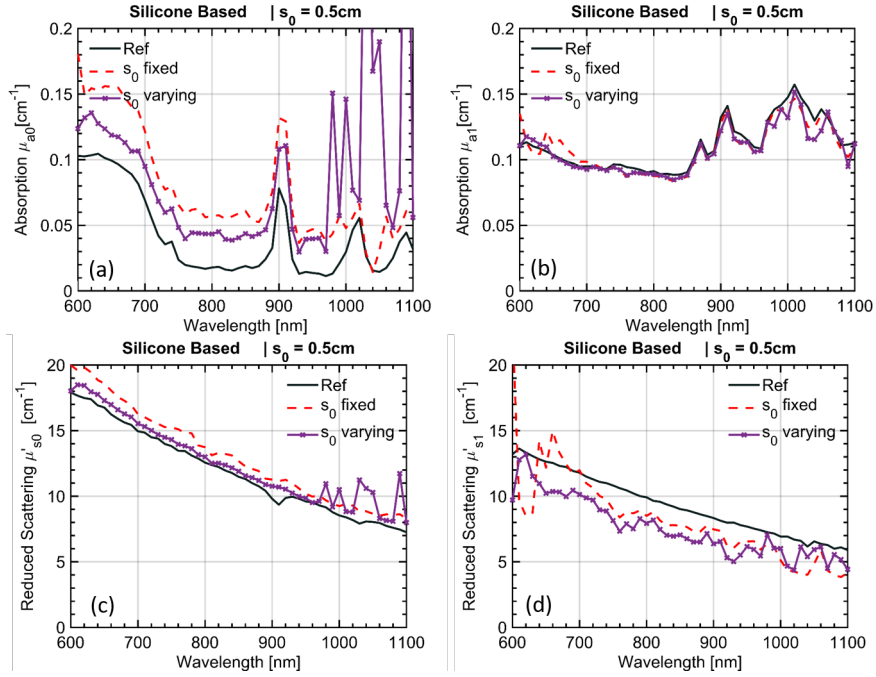


Figure 3.3: The absorption and reduced scattering spectra of the two layers of each of the silicon based two-layer structure with a top layer thickness of 0.5cm. Results obtained both by fixing s_0 to the actual value and varying it (as a free parameter in the fitting routine) are presented along with the reference data for comparison.

from the largest ρ or from an approximate value obtained from literature and following the Mie law, had a negligible impact on the recovery of the other optical properties (not shown here).

Chapter 3. Retrieval of Absolute Optical Properties from Heterogeneous/Layered Diffusive Media

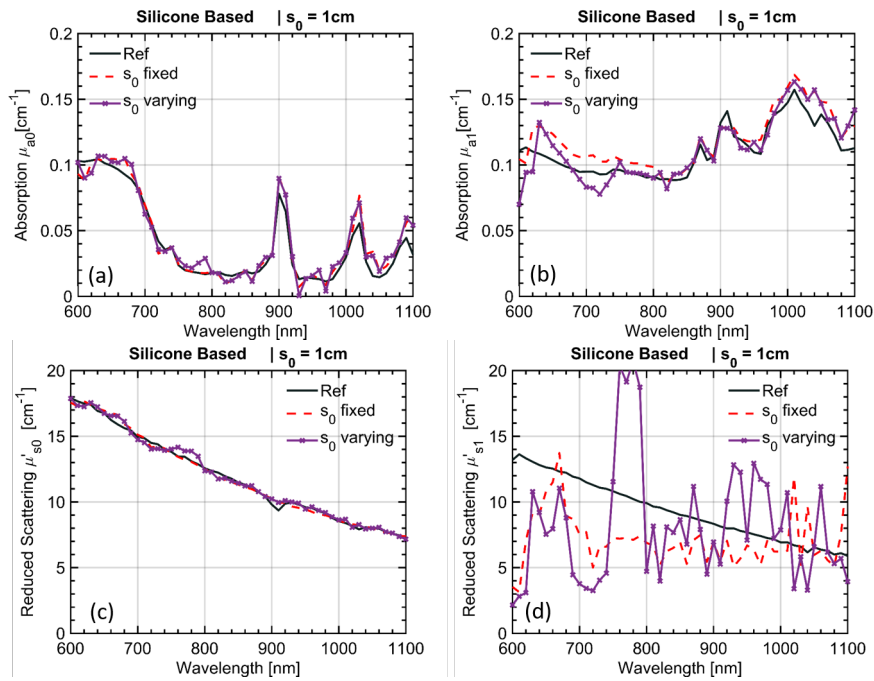


Figure 3.4: The absorption and reduced scattering spectra of the two layers of each of the silicon based two-layer structure with a top layer thickness of 1cm. Results obtained both by fixing s_0 to the actual value and varying it (as a free parameter in the fitting routine) are presented along with the reference data for comparison.

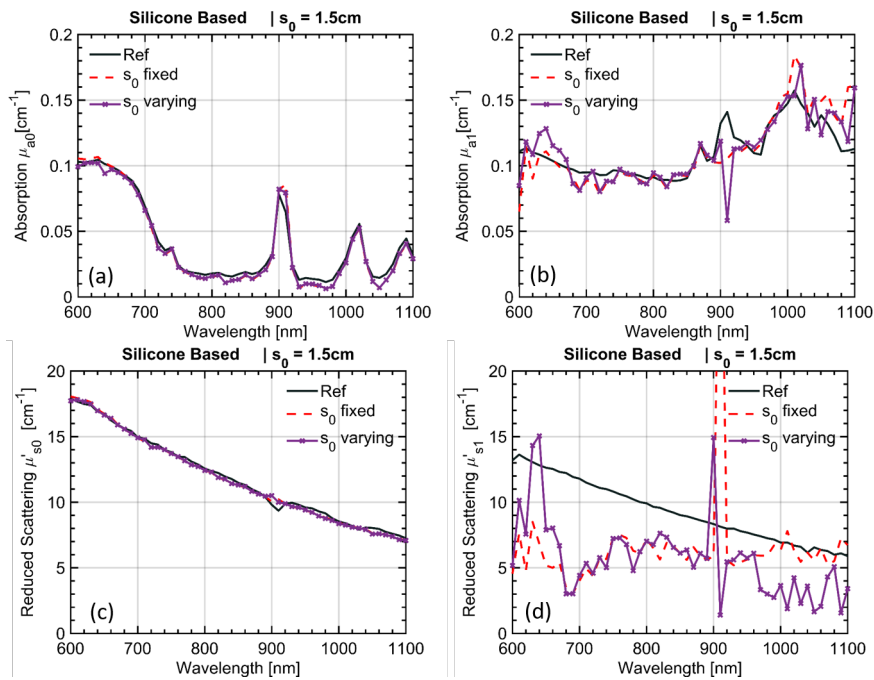


Figure 3.5: The absorption and reduced scattering spectra of the two layers of each of the silicon based two-layer structure with a top layer thickness of 1.5cm. Results obtained both by fixing s_0 to the actual value and varying it (as a free parameter in the fitting routine) are presented along with the reference data for comparison.

3.2. Silicon Based Two-layer structures

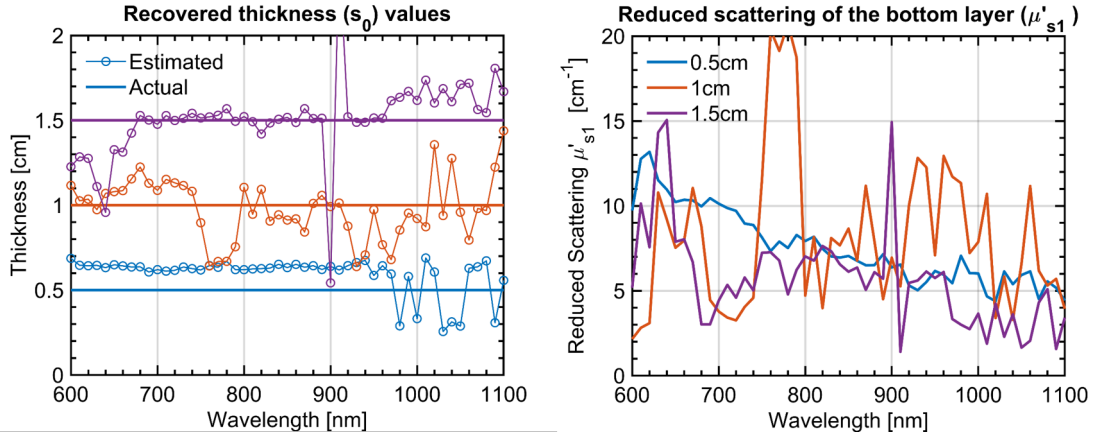


Figure 3.6: The recovered spectra of s_0 (a) and μ'_{s1} (b) for the three cases presented above.

The recovered values of thickness of the top layer (s_0) are plotted in Fig. 3.6(a). This parameter suffers a 20% over-estimation for the lowest top layer thickness (0.5cm) but is retrieved with decent accuracy otherwise. Fig. 3.6 also suggests some co-relation between s_0 and μ'_{s1} when all the five parameters freely varying. This parameter is also relatively less relevant to the the recovery of the other optical properties. Fig. 3.7 plots the recovered μ_{a1} of for the case where the actual top layer thickness of 1cm, was estimated fixing s_0 to five different values (0.8, 0.9, 1.0, 1.1 and 1.2cm). A 20% deviation of s_0 from the true value effects the recovery of μ_{a1} on an average by about 7%.

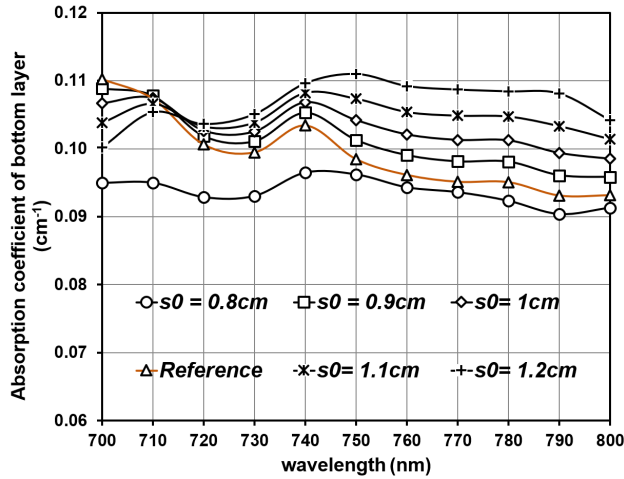


Figure 3.7: Effect of misevaluation of s_0 on the recovery of the other optical properties. μ_{a1} from Fig. 3.4 retrieved for 5 fixed thickness values within a 20% range of the true value of s_0 (1cm) in comparison with the reference data.

3.2.3 Spectral Fitting – Quantification of Absorber Concentrations

The wealth of spectral information available from broadband DOS allows us to quantify the concentration of the different absorbers present in the sample under investigation. To estimate the concentration of the different absorbers present in the sample, the well

Chapter 3. Retrieval of Absolute Optical Properties from Heterogeneous/Layered Diffusive Media

known *Lambert Beer law* is used. The measured absorption coefficient is assumed to be a linear combination of the extinction coefficients of components weighted by their concentration. Thus, by fitting a linear combination of the extinction coefficient spectra of (i.e. the absorption of the pure substance, typically reported in the literature) of the individual absorbers are to the the measured absorption spectrum it is possible to retrieve the concentration of the different absorbers.

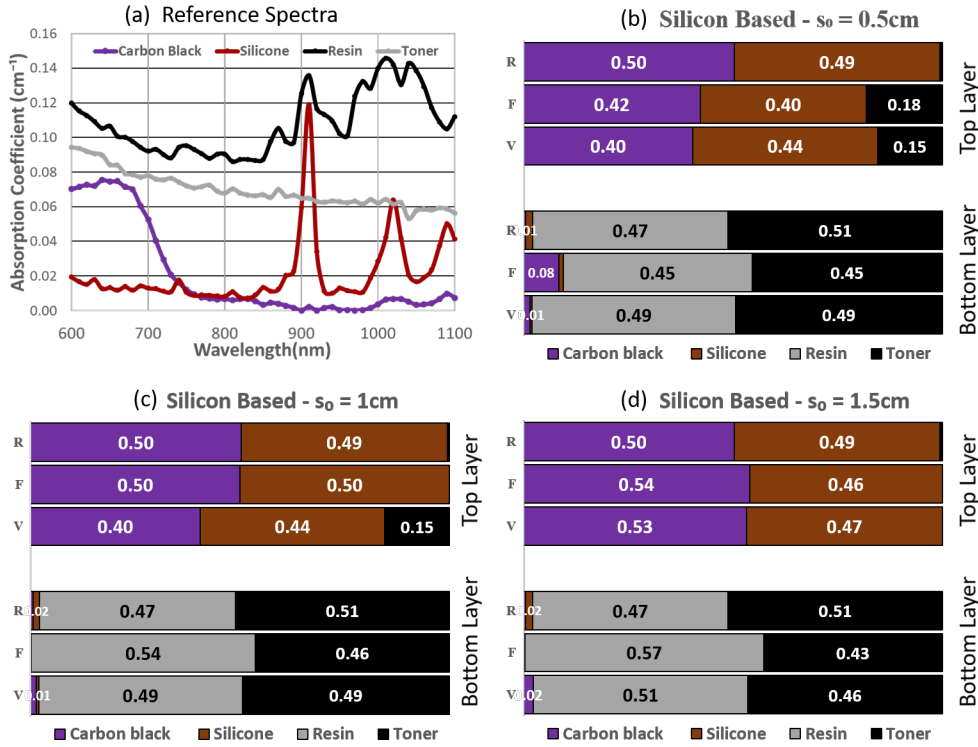


Figure 3.8: Absorption spectra (a) of the different absorbers for the silicon based two layer structures. (b,c and d) recovered concentrations of the different absorbers for the three configurations corresponding to the three top layer thicknesses (specified in the title of the subplot). The values of concentrations are obtained from the recovered absorption spectra for the top (μ_{a0}) and bottom (μ_{a1}) layer. The letters **R**, **F** and **V** on the left side of each bar plot correspond to the normalized concentration retrieved from the **reference** spectrum, spectrum with **fixed** s_0 and spectrum with **varying** s_0 respectively. The color coding for the individual absorbers in the bar plot is given underneath the individual subplot (purple- carbon black, brown - silicone, gray - resin and black - toner)

The absorption spectrum of the different constituent absorbers of the two layered structure are presented in Fig. 3.8(a). The retrieved concentrations of the individual layers are normalized in a manner such that the two absorbers of the specific layer (carbon black and silicone for the top layer and toner and resin for the bottom) represent 50% contribution to the layer's absorption i.e. half of the bar plot. Since the absolute concentration of the components in the individual layers is of little interest here, such a normalization allows for a better visualization and easy comparison.

The results once again showcase the success of the model in retrieving the concentrations. The recovered concentrations both with fixed and varying s_0 are in very good agreement with the reference values. This is true even in the case the $s_0 = 1.5$ cm.

3.3 *Ex-vivo* Biological Tissue Based Two-layer structures

The two-layer structure of the second kind was designed using two different kinds of *ex-vivo* biological tissues. In this case the top layer was a 1.25cm thick porcine fat tissue (Lard) and a 5cm thick muscle tissue from a young bovine (Veal) was considered for the bottom layer. Both the tissues were freshly purchased from a local grocery store and were cut into cubes with the measurement surface having the dimensions of about (10cm x 10cm), to avoid boundary effects. The layer of Lard was placed on top of the Veal tissue, similar to the silicon based two-layer structure (Fig 3.1).

3.3.1 Analysis using Homogeneous Model

Fig. 3.9 presents the results for the tissue based two-layer structure obtained using the homogeneous model. The reference spectra are plotted as a average of resultant optical properties from the multiple reflectance and transmittance measurements with the error bars representing the standard deviation. The refractive index of the medium in this case was assumed to be 1.4.

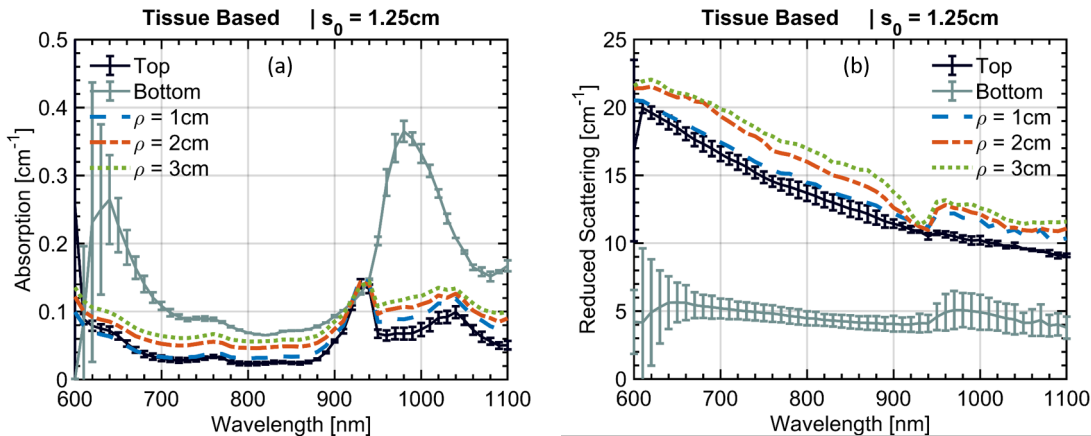


Figure 3.9: The absorption and reduced scattering spectra of the two layer structures at the three ρ analysed using a homogeneous or semi-infinite model. The reference optical properties of the two layers are provided with error bars representing the standard deviation over measurements at different ρ and in different geometries. The thickness of the top layer (s_0) in this case is 1.25cm.

The reference absorption and reduced scattering coefficient values (Fig. 3.9 Top and bottom) were obtained (similar to the previous case) by performing multiple measurements and averaging the resultant spectra. Key absorbers with known spectral features are, (a) de-oxy hemoglobin (spectral signature at 760nm), (b) water (peak at 970nm) and (c) lipids or fat (double peak at 930nm and 1030nm).

Here too, as in the case of the other structure, the absorption at $\rho = 3\text{cm}$ is heavily influenced by the top layer. Reduced scattering spectra is mainly influenced by the top layer in absolute value. A substantial dip in the reduced scattering spectra at 930nm is due to a co-relation with the sharp rise in the absorption at that wavelength from the lipids present in the Lard tissue.

3.3.2 Analysis using Layered Model

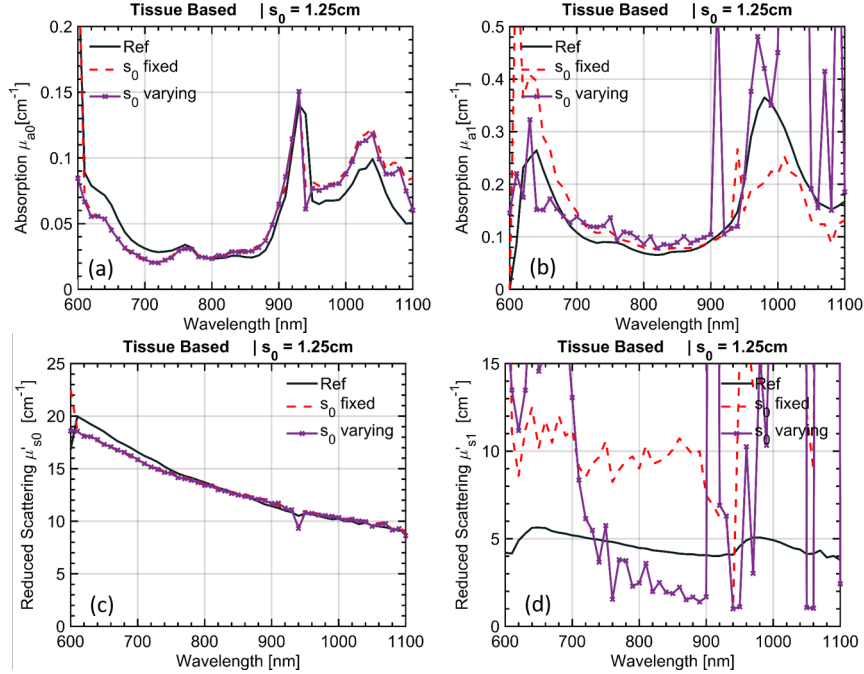


Figure 3.10: The absorption and reduced scattering spectra of the two layers of each of the *ex-vivo* tissue based two-layer structure with a top layer thickness of 1.25cm. Results obtained both by fixing s_0 to the actual value and varying it (as a free parameter in the fitting routine) are presented along with the reference data for comparison.

The retrieved absorption and reduced scattering coefficient spectra of the two layers using the two-layered solution of the DE (sec 1.6.2) are presented in Fig. 3.10. All the observations made in the case of Silicon-based two layer structures are equally valid in the case of the *ex-vivo* biological tissue as well. The recovery of absorption in the bottom layer (μ_{a1}) in relatively high absorption region i.e. beyond 970nm is deviated the most from the reference value. As in the case of the Silicone based two-layered structure, fixing the s_0 to the actual value and varying it hardly influences the recovery of three out of four parameters. (μ_{a0} , μ'_{s0} and μ_{a1}).

3.3.3 Spectral Fitting – Quantification of Absorber Concentrations

The usefulness of the quantification of absorber concentration can be appreciated more in the case of the *ex-vivo* biological tissue. The key absorbers in this biological tissue in this wavelength range are the different tissue constituents like blood, water, lipid and collagen. The extinction spectra of these constituents are presented in Fig. 3.11 (a) and obtained from literature [68]–[70].

Since, in this case, the top layer (Lard) is porcine fat it is expected to mainly consist of fatty lipids which is what is reflected from the reference data. On the other hand, Veal, (bovine muscle) tissue is comprised of water and protein which could be both collagenous and non-collagenous[71]. Both of these expectations are well reflected in the results from the reference data and are once again recovered with a fair amount of accuracy with two layered analysis model. The recovered concentrations of the upper

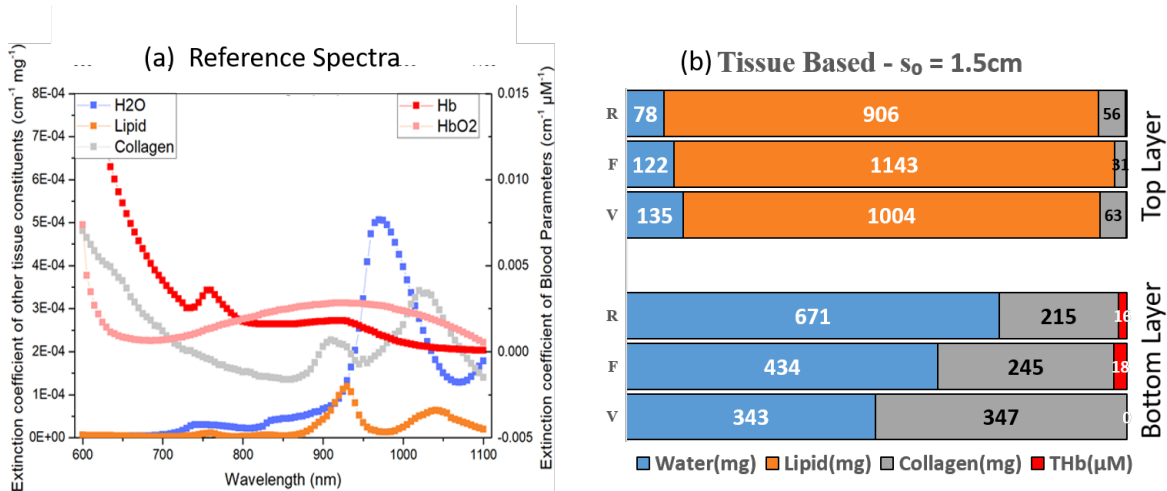


Figure 3.11: Absorption spectra (a) of the different tissue constituents in biological tissue. (b) recovered concentrations of the tissue constituents for the ex-vivo tissue based two-layered structure. The values of concentrations are obtained from the recovered absorption spectra for the top (μ_{a0}) and bottom (μ_{a1}) layer. The letters **R**, **F** and **V** on the left side of each bar plot correspond to the normalized concentration retrieved from the **reference** spectrum, spectrum with **fixed** s_0 and spectrum with **varying** s_0 respectively. The color coding for the individual absorbers in the bar plot is given underneath the Fig 3.11(b) (blue- water, brown - lipid, gray - collagen and red - blood)

layer with varying s_0 are more consistent with the reference values with a deviation of about 10 % while the lower layer with it's large absorption peak is better represented in the case where s_0 was fixed (deviation of about 30 % from the reference value). The total hemoglobin content in the tissue (THb) is obtained by summing the recovered oxy (HbO₂) and deoxy (Hb) hemoglobin. 16 μM of THb is expected to be present in the bottom layer and about 18 μM of THb is recovered (with the s_0 fixed). It is interesting to note that the sum of the resultant concentrations of all the constituents for each individual layer is close to 1000 mg. This implies that the density of the tissue is 1000 mgcm^{-3} or 1 gcm^{-3} which is not far from the expected value for different animal and human tissue types *ex-vivo* [72].

3.4 Initial Application *In-vivo*

As a final step the performance of the model was assessed on some in-vivo data. Multi-distance broadband measurements similar to the those described in the last sections (with the same instrumentation as discussed in Chapter 2) were performed on the forehead of a healthy adult volunteer while lying on a bed in supine position. The same choice of inter-fiber distances was maintained ($\rho = 1,2$, and 3cm). The time necessary to perform the complete measurement was under 5 minutes.

Here too, the data is first analysed using the homogeneous model, followed by analysis using layered model and finally spectral fitting to recover concentration of tissue constituents. The key difference here is the lack of knowledge regarding the thickness of the top layer s_0 and the lack of any reference values.

3.4.1 Analysis using Homogeneous Model

The refractive index of the medium is assumed to be 1.4. The in-vivo absorption and reduced scattering spectra are presented in Fig. 3.12. A clear increase in the absorption is observed with increasing ρ which is indicative of an increase in the blood and water content with increased ρ . This increase may be regarded as a hint that with increasing ρ the underlying brain tissue (which is richer in blood and water content relative to the extracerebral tissue) is being probed. The reduced scattering spectra shows no major variation with ρ .

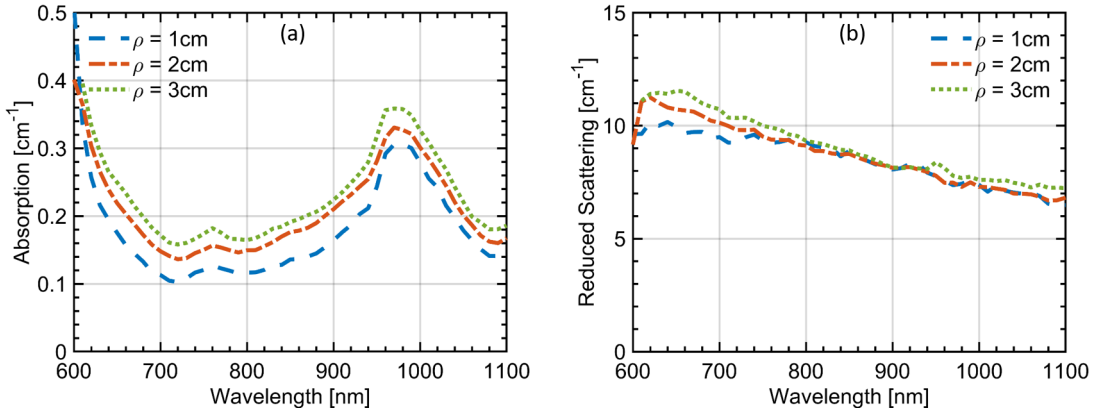


Figure 3.12: The absorption and reduced scattering spectra of adult human forehead region in-vivo at the three ρ analysed using a homogeneous or semi-infinite model.

3.4.2 Analysis using Layered Model

The data is then analysed using the two-layered solution of the DE (sec 1.6.2) with the following initial conditions. The top layer thickness (s_0) was fixed to be 13mm, which corresponds to a typical value of thickness of the extracerebral tissue (from literature) [73]. This way the top layer could be assumed to be extra-cerebral tissue and bottom layer to be the brain tissue. The refractive indices for the two layers were taken from literature (1.55 for the extracerebral tissue [74] and 1.4 for the brain tissue [75]). The fitting procedure was first performed with all the other four parameters (μ_{a0} , μ'_{s0} , μ_{a1} and μ'_{s1}) varying. The resultant spectra are displayed in Fig. 3.13.

The recovered absorption spectrum shows a higher value on an average for the bottom layer (μ_{a1}) compared to the top layer (μ_{a0}). The recovered reduced scattering spectrum of the top layer μ'_{s0} is similar to the values retrieved using the homogeneous model. CSF (Cerebrospinal fluid), a relatively thin, transparent layer lying between the skull and the brain matter, is well known for its "light guiding" effect [76] and its structural composition that strongly influences the light scattering [77]–[80]. This could be a possible explanation for the relatively low reduced scattering spectra of the bottom layer (below 1 cm^{-1} beyond 900nm).

3.4.3 Spectral Fitting – Quantification of Absorber Concentrations

The key absorbers/ tissue constituents for the case of the *ex-vivo* tissue based (discussed in 3.3.3) are exactly the same absorbers in the case of in-vivo measurements as well.

3.4. Initial Application *In-vivo*

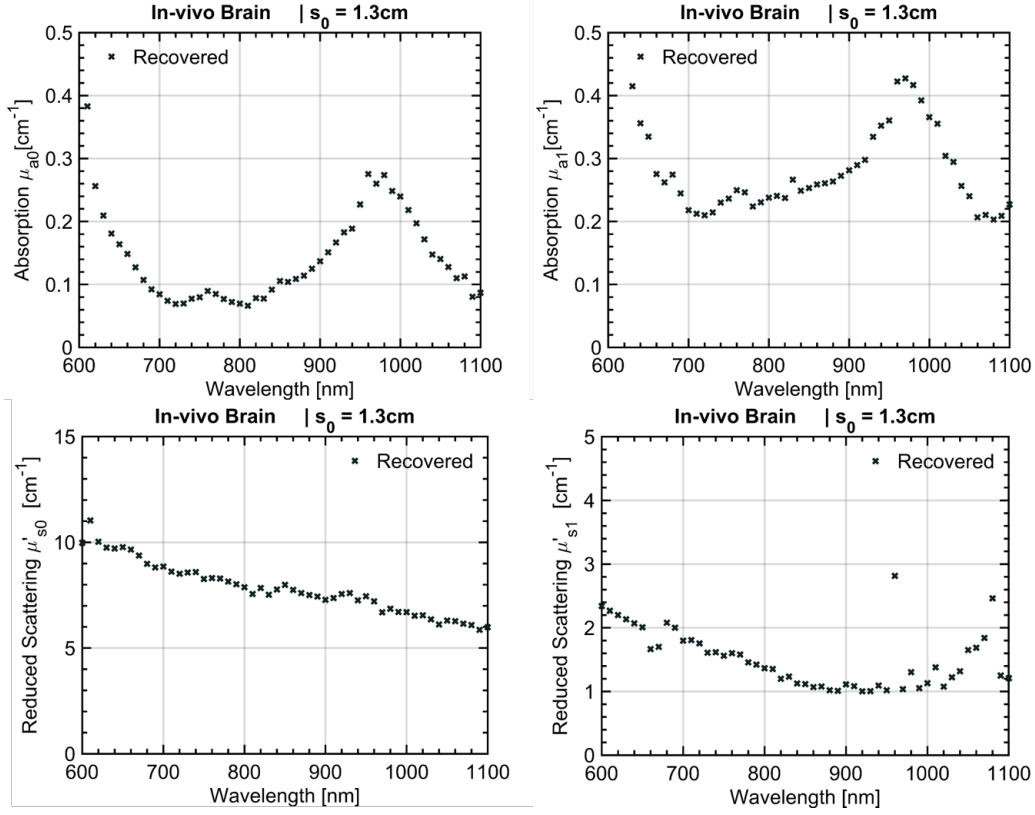


Figure 3.13: The absorption and reduced scattering spectra of the adult human forehead region *in-vivo* obtained using a two-layered model. The thickness of the top layer is assumed to be 1.3cm. The top layer represents the extra-cerebral tissue and the bottom layer corresponds to the brain tissue.

Thus, we perform follow the same procedure to retrieve the absorber concentrations for the human forehead *in-vivo*. However, since there is no reference against which the recovered concentrations can be compared, the concentrations for the constituents obtained using the spectra from the homogeneous model will be used to understand and compare the results from the layered model.

The resultant concentrations obtained from the absorption spectra of the two layers and the absorption spectra at the three inter-fiber distances (ρ) when analysed using the homogeneous model are tabulated in 3.1.

Firstly, the results from the standard homogeneous model (*Homo*) suggest that the total blood content recovered increases with increasing ρ further confirming the assumptions made earlier about probing the deep-lying brain tissue at larger ρ . However, more interestingly, we observe an two other interesting features with the results from the homogeneous model. An increase in collagen content is observed at $\rho = 2$ cm from $\rho = 1$ cm, followed a decrease in the value at $\rho = 3$ cm. However, the opposite is true in the case of the water and lipid content, i.e. the concentration of these constituents decreases from $\rho = 1$ cm to $\rho = 2$ cm but experiences an increase from $\rho = 2$ cm to $\rho = 3$ cm. Put together, these finding suggest that for this particular subject, at $\rho = 2$ cm the tissue being probed by the measurements is bony region of the skull. This is because $\rho = 2$ cm we see an increase in collagen (a signature of the calcenous bone tissue) while at the larger $\rho = 3$ cm we see a decrease in collagen accompanied by an increase in water,

Chapter 3. Retrieval of Absolute Optical Properties from Heterogeneous/Layered Diffusive Media

Table 3.1: Concentrations of tissue constituents obtained from the absorption spectra recovered using the layered model (top and bottom corresponding to extra-cerebral tissue and brain tissue respectively) and the absorption spectra at the three ρ considering the sample (forehead region) to be homogeneous.

Model		Hb	HbO ₂	THb	H ₂ O	Lipid	Collagen
		μM	μM	μM	ml	mg	mg
Layered	Top	8.2	17.8	26.0	334	311	161
Homo	$\rho = 1\text{cm}$	7.8	19.4	27.2	400	215	146
Homo	$\rho = 2\text{cm}$	5.9	24.3	30.2	318	149	228
Homo	$\rho = 3\text{cm}$	10.0	23.0	33.0	375	199	161
Layered	Bottom	17.4	42.9	60.3	406	128	0

Hb - Deoxy hemoglobin, HbO₂ - Oxy hemoglobin, μM - micromolar (unit of concentration), Homo - Homogeneous Model, Layered - Two-Layered Model.

blood and lipid indicating the fleshy brain tissue.

Concentrations retrieved from the layered model suggest that the "top" layer corresponding to the extracerebral tissue has a total Hb of 26 μM and a roughly 40:40:20 ratio of water, lipid and collagen, while the "bottom" layer corresponding to the brain tissue comprises of 60 μM total Hb and an 80: 20 ratio of water and lipid with *zero collagen*.

While further validation on a larger set of in-vivo measurements is necessary, the larger quantity of water and blood in the bottom layer relative to the superficial layer and the confinement of all of the collagen primarily in the superficial layer indicate that the layered model distinguishes the influence of the collagen rich 'skull' (which is expected to dominate the superficial or extracerebral layer in terms of optical properties) from the underlying brain tissue.

3.5 Conclusions:

In this chapter, the development and validation of an analytical technique to recover the absolute optical properties of the different layers of layered media using broadband relative multi-distance time-resolved DOS in reflectance geometry is presented. The instrument designed as a part of this thesis and discussed in the previous chapter is ideally suited for this purpose.

Two types of multi-layered structures with reliable reference values were designed and used for this purpose. Reliable recovery of 4 out of 5 parameters ($\mu_{a0}, \mu_{a1}, \mu'_{s0}$ and s_0) was achieved over the entire spectral range for both structures (median deviation $\leq 15\%$ from the reference values over the entire spectrum). Large inaccuracies were found in the retrieval of scattering coefficient from bottom layer (μ'_{s1}), but these can be overcome by fixing this parameter to values obtained from literature or through other methods. The thickness of the top layer (s_0) was another parameter that was recovered with a reasonable accuracy, but faster convergence and smoother fit of the other parameters were achieved by fixing this parameter to a reasonable value (within 20% of the actual value). The retrieval of the optical coefficients of the two-layered structures with a standard, semi-infinite model was also investigated for different inter-fiber distances. However, without a two-layer model, these absorption values are a combination of the

top and bottom layers.

Spectral fitting was performed to reconstruct the absorber concentration for each of the layer in the two structures to understand the spectral features are preserved during the retrieval. In terms of retrieval of absorber concentration as well, the two-layer model distinguishes the primary absorbers for each individual layer and is consistent with the reference values.

Final the layered model is applied to a set of relative multi-distance measurements performed on the human forehead region *in-vivo*. The resultant absorption spectra and the recovered constituent concentrations suggest that, taking into consideration the a proper value of top layer thickness (s_0) the optical properties of the superficial (extracerebral) tissue can be disentangled from those of the underlying brain matter.

***In vivo* Application of Broadband DOS for Layered Media: Abdominal Adipose Tissue**

4.1 Introduction

Obesity, simply defined as excessive, unhealthy amount of fat mass (FM) in the body, is a pathological condition that affects a significant number of adults. Paradoxically coexisting with malnutrition, an escalating global epidemic of overweight and obesity – “globesity” – is taking over many parts of the world[81]. This pathological condition is significantly related to the type and amount of adipose tissue (AT) present in our body. In fact, “adiposity-based chronic disease” (ABCD) is an alternative name for obesity which clearly outlines the influence of the adipose tissue on this pathology.

Obesity, especially among the elderly, leads to an impaired functioning of adipose tissue (AT). Recent studies have equivocally ascertain that the total AT present in the human body displays a very self-dependent, 'organ' like functionality composed of different kinds of cells, having a clearly defined anatomy and endocrine properties and a good tensility to physiological and environmental stimuli [82]–[84]. Thus a good understanding and racking of this "organ" continuously is necessary to keep obesity and related pathalogies under check.

An in depth comprehension of the physiology of AT is beyond the scope of this thesis, and is available for reference here. It is sufficient to know that AT has multiple sub divisions one of which is the subcutaneous AT (SAT), located directly underneath the skin. This comprises more than 80% of the body fat. While distributed through out the body, it is found in higher proportions at three locations namely Gluetal SAT, Femoral SAT and Abdominal SAT. Abdominal Fat is characterized by rapid uptake and storage of energy from the diet and a high lipid turnover (i.e., lipolysis). Healthy AT usually expands by a combination of increase in adipocyte size and number. However,

obesity could affect this expansion which is necessary to store the energy surplus. This could consequently lead to fat deposition in other tissues such as skeletal muscle and liver leading to metabolic dysfunctions.

Thus, it becomes essential to take into account such metabolic and phenotypic parameters while dealing with obesity and related pathologies to optimize disease prevention and treatment strategies. Body Mass Index or BMI (calculated as the weight in kilograms divided by the square of the height in meters) is the closest such index considered for this purpose. However, it has been shown that BMI does not show a very strong correlation with body fat in obese individuals and older subjects with lower muscle mass. Further information of fat compartmentalization is missed out in this case. Better alternatives include, waist circumference, hip circumference, waist-to-hip ratio, and waist-to-height ratio which are still indirect indices for AT valuation. Computerized tomography and magnetic resonance imaging are the most accurate techniques available for the measurement of fat sub-compartments, however they are highly expensive, not portable and have huge limitations in clinical practice[1].

Diffuse Optics opens up a very interesting net of possibilities at this juncture. It is non-invasive, portable and inexpensive with considerable sensitivity and specificity. Diagnostic techniques based on diffuse optics are potentially good candidates to meet that need, as they allow the development of relatively simple and inexpensive instruments, suitable for use both in a clinical environment and in the doctor's office, and providing the non-invasive and objective assessment of tissue optical properties (absorption and reduced scattering). In turn, the knowledge of the optical properties at several wavelengths enables the estimate of diagnostically relevant tissue properties: tissue composition in terms of its major constituents (water, lipid, and collagen), physiological parameters (blood volume and oxygenation level), and microstructural information derived from scattering parameters.

However, as highlighted here, adipose tissue is a complex organ, showing a highly stratified structure, which might prove more difficult to characterize with a simple model. Thus, in this chapter, we investigate the performance and limitations of using the homogeneous model to interpret multi-distance DOS data and characterize abdominal adipose tissue. While it is evident that the abdominal region poses a three layered structure, one of the two-layered models discussed in the previous chapter is applied to the data initial results with a two-layered model are also discussed.

4.2 Broadband optical properties of the human abdomen *in-vivo*

The instrument developed in Chapter 2 is intended ultimately to be employed in a clinical study on the frailty of the adipose tissue in the elderly and obese. As a first step in this direction, a feasibility test was conducted where the instrument was used to perform multi-distance measurement in the abdominal region of a small group of healthy volunteers.

4.2.1 Subjects, Measurements and Analysis

A cohort of 10 healthy adult male volunteers was chosen for this study. The recruited volunteers were all staff and Ph.D students of Politecnico di Milano (Milan, Italy). They were informed on the main study objective, the protocol of TD-DOS measurements

4.2. Broadband optical properties of the human abdomen *in-vivo*

Subject	Age (y)	Height (m)	Weight (kg)	BMI (kg/m ²)	WC (cm)	Thickness (mm)
#1	53	1.75	67	21.9	86	24.6
#2	74	1.73	78	26.1	106	18.4
#3	25	1.91	87	23.8	88	7.8
#4	24	1.7	64	22.1	74	6.6
#5	37	1.8	76	23.5	63	14.3
#6	41	1.8	86	26.5	103	28.6
#7	48	1.83	100	29.9	115	35
#8	58	1.73	59	19.7	79	6.6
#9	38	1.78	74	23.4	85	4.1
#10	47	1.9	115	31.9	110	26.4

Table 4.1: Demographics of the subjects involved in the study here, BMI = Body Mass Index | WC = Waist Circumference and Thickness corresponds to Thickness of the SAT layer measured using an ultrasound echo-graph

and the safety of the instrument. General anthropomorphic data of the subjects was recorded. Waist circumference was taken by the operator at the mid-point between iliac crest and the last rib, along the auxiliary middle line. A commercially available echo-graph was used to estimate the thickness of the skin and SAT layers. Table 4.1 summarizes the general anthropometric data for the ten subjects involved in the study.

Measurements were performed with the subject lying in the supine position. The choice was the wavelength range was once again restricted to 600 - 1100nm with a step size of 10nm. Measurements were performed at the three inter-fiber distances $\rho = 1, 2$ and 3cm. A total of 5 positions:

- 2 cm left to the navel(2L);
- 2 cm to the left and 2 cm below the navel(2L2D);
- 4 cm left to navel(4L);
- 4 cm to the left and 2 cm below the navel(4L2D);
- and 8 cm left to the navel(8L)

were chosen with the navel of the subject as the point of reference. All distances were taken with reference to source 2 with the probe positioned vertically with the detector downwards. The locations and probe positioning are pictorially represented in Fig 4.1. Total acquisition time per location was under 5 minutes.

The analysis performed for this study assumed the sample under investigation to be a homogeneous medium. Both the Diffusion Approximation (DA) and the stochastic Monte Carlo (MC) model described in Chapter 1 were used for the analysis. But, only the results obtained using the MC analysis model will be presented here. This is because, analysis using the DA was found to be prone to inaccuracies, especially in cases with very low absorption and for short inter-fiber distances. In cases where the diffusion approximation is valid (i.e. high scattering and large inter-fiber distances) both the models are in good agreement.

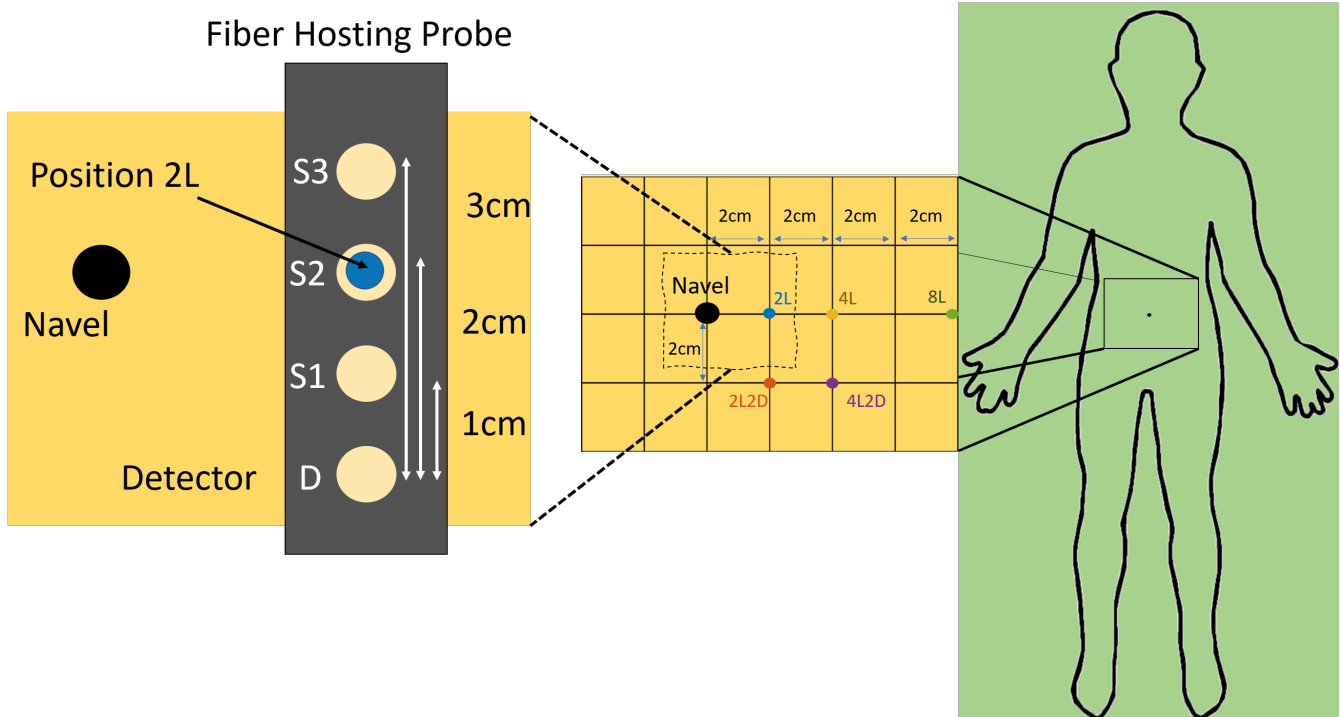


Figure 4.1: A representative figure of the different positions, relative to the navel, considered for the study and the position of the fiber hosting probe.

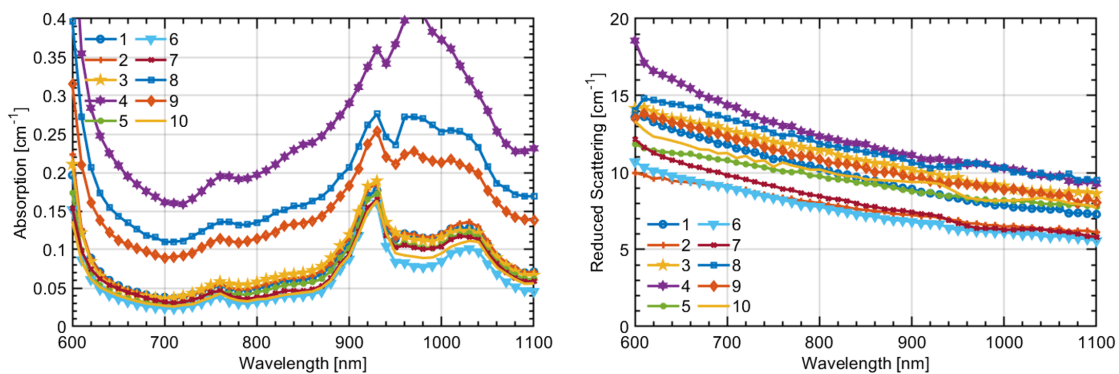


Figure 4.2: Absorption and reduced scattering spectra measured on the abdominal region of the 10 subjects enrolled in this study. The measurements were performed at an inter-fiber separation $\rho = 2$ cm at a location 8 cm to the left of the navel.

4.2.2 Absorption and Reduced Scattering spectra

The absorption (left) and reduced scattering (right) spectra of all the subjects at inter-fiber distance (ρ) = 2 cm in the same location (8 cm right of the navel) are shown in Fig 4.2. Clearly, there is a wide variability, both in spectral features and the absolute values of both the quantities. This is an evidence of the heterogeneity of the stratification of the abdomen and the inter-subject variability. The key features with respect to the absorption spectrum are the tail of hemoglobin – mainly Hb – below the wavelength of 700 nm, the peak of Hb overlapped to a the very small water shoulder around 760 nm,

4.2. Broadband optical properties of the human abdomen *in-vivo*

the clear peak of lipid at 930 nm with a second smaller one at 1020 nm, and, in some cases, the water contribution around 980 nm. HbO_2 is definitely present, but less evident since its decreasing tail in the red is superimposed to Hb, and the broad maximum around 900 nm is overlapped to the other sharper features (e.g. lipid). For relatively small values of upper layer (skin+SAT) thickness, the overall absorption increases with the marked contribution of water and blood as a clear sign that the underlying muscle tissue is reached by the measurement.

With regards to the reduced scattering spectrum, there are no distinct spectral features. The expected power-law dependence of μ'_s on lambda for biological tissues in this spectral range is clearly visible. However, the data represents a considerable inter-subject variability both in amplitude and in slope of the scattering spectrum.

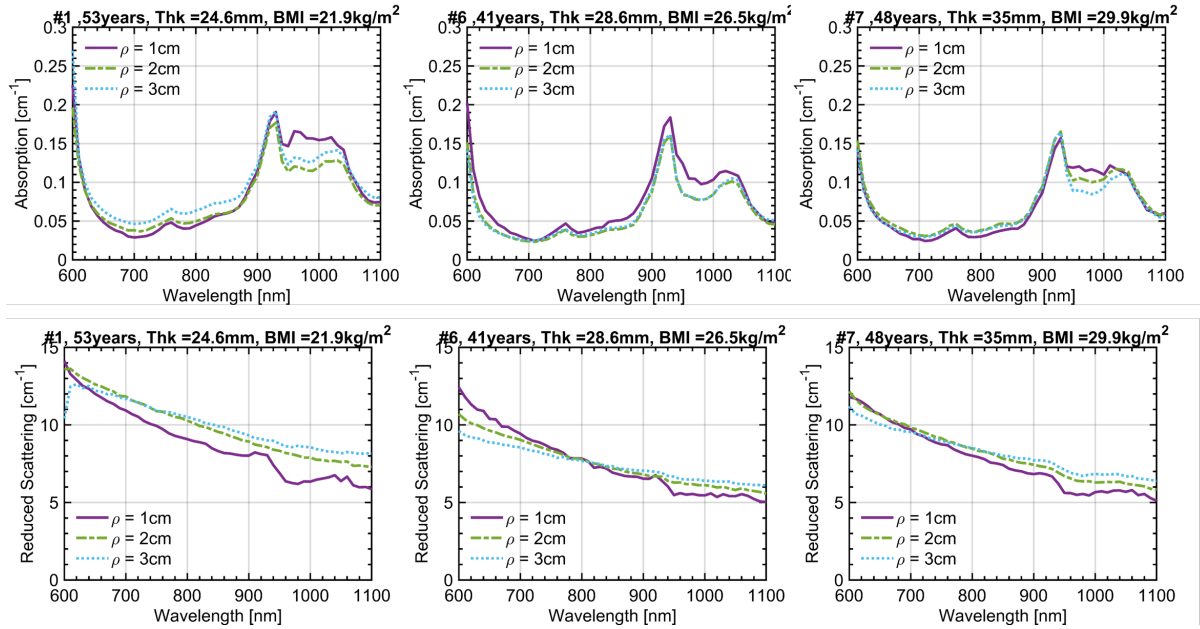


Figure 4.3: Absorption and reduced scattering coefficient spectra at the three inter-fiber distances $\rho = 1, 2$ and 3 cm. Results are presented for 3 subjects with further information about the subject in the title of each subplot (Thk = Thickness of the skin and adipose tissue layer). The measurement was taken 4 cm to the left of the navel.

To gain more insight into the effects of the heterogeneous adipose structure on the absorption and scattering spectra, we present in Fig 4.3 the absorption (top) and reduced scattering (bottom) spectra for all the 3 inter-fiber distances again at 4 cm right of the navel. For the sake of brevity data from 3 most representative subjects is shown. The data for all the 10 subjects is available in the Appendix (refer Fig. A.4). With regards to the absorption two main effects are observed. The first and most obvious one is the progressive increase in μ_a upon increasing ρ . This effect is more evident in Subject #4 (center) as compared to the other 2 cases. It can be ascribed to the increased relevance of the muscle layer upon increasing ρ (and therefore depth of probing).

A more unexpected observation is the mild increase in μ_a around the water peak (980 nm) for the shortest $\rho = 1$ cm, as observed in Subject #1 (left) and #7 (right). Since a shorter ρ is more sensitive to shallower regions, the leading hypothesis attributes this

Chapter 4. *In vivo* Application of Broadband DOS for Layered Media: Abdominal Adipose Tissue

increase to the contribution of the skin that is more hydrated (70%) [85] as compared to the underlying adipose tissue. Still, the relatively small thickness of this layer calls for some caution in a straightforward attribution. In-fact, very thin superficial layers are not expected to affect much the temporal shape of the diffuse photon distribution, and consequently of the estimated μ_a .

The reduced scattering spectra display a clear increase of slope upon reducing ρ , for all subjects, also for the middle one where the SAT thickness is small. Again, an increased influence of the superficial layer (dermis) can be speculated due to the expected steepest scattering spectrum caused by collagen fibrils. In particular, a bi-component scattering spectrum is observed for Subject #1 (left) and #7 (right) for $\rho = 1$ cm, with a steepest slope in the red (<700 nm). This observation is consistent with the small dimension of collagen fibrils, which are expected to cause a behavior close to Rayleigh scattering [86].

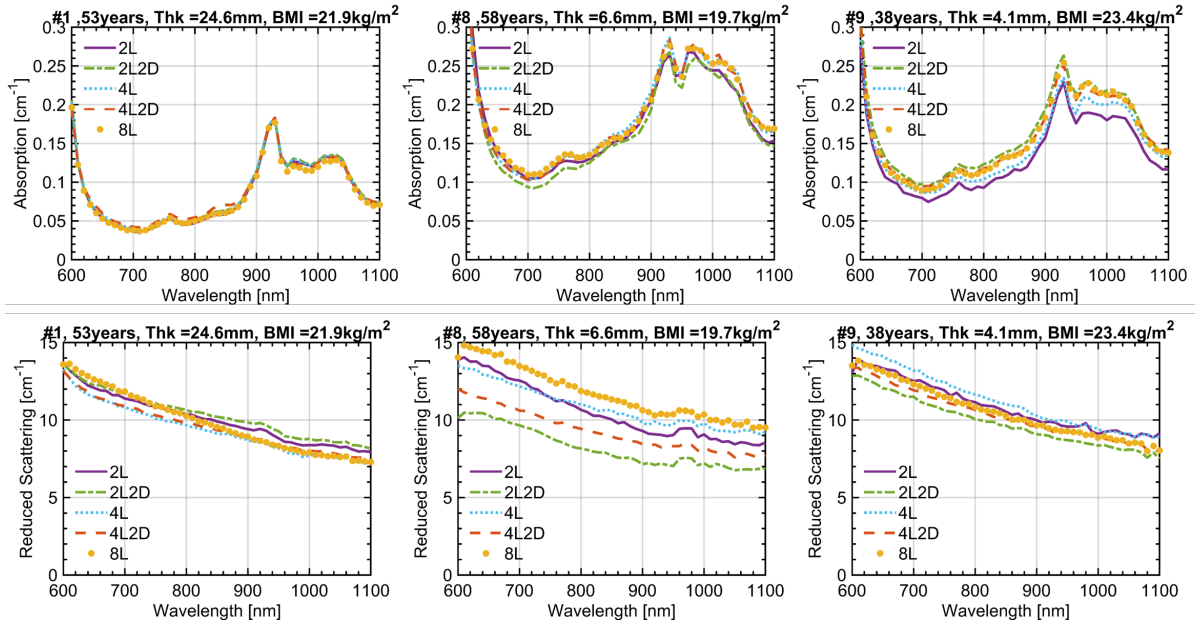


Figure 4.4: Absorption and reduced scattering spectra at five different locations in the abdominal region. The legend identifies the measurement position with reference to the navel. For example: (4L2D – corresponds to a point 4 cm to the left and 2 cm below the navel). Results are presented for 3 subjects with further information about the subject in the title of each subplot. For all the measurements $\rho = 2$ cm.

The variations in absorption (top) and scattering (bottom) spectra for different locations on the abdomen are shown in Fig 4.4 for 3 subjects, representative of the whole study, while all data are reported in the Supplementary data (refer Fig. B.1). In general, all key spectral features are preserved for different locations on the same subject. Yet, some intra-subject variability is observed which is more marked in the case of thinner adipose layer. In detail, the coefficient of variation CV is 5.2%, 4.0%, 11.0% for μ_a at 800 nm (left to right) and 3.9%, 14.1%, 5.4% for μ'_s . Considering the whole set of subjects, the median / max CV is 8.6% / 18.0% for μ_a and 6.6% / 18.1% for μ'_s .

4.3 Tissue Composition:

The absorption and reduced scattering spectra were further analyzed to retrieve the concentration of key absorbers (Hb, HbO₂, lipid, water collagen) as well as the scattering amplitude and power (a, b). The method used for the retrieval of the absorber concentrations is similar to the one described in Chapter 3. A spectral constraint is added to this procedure as described in [87] to further enhance the reliability of the results. Results for all subjects and all ρ distances for the location 4cm the left of the navel are reported in Table 4.2. It is important to remind that the optical properties were derived using a purely homogeneous tissue model. Due to the heterogeneous nature of the abdomen, these numbers are meant as averages over different volumes depending on the source-detector distance. Further, spectral distortion is expected due to different spatial sensitivity maps for different wavelengths. Therefore, these values must be taken with caution, not considering them as absolute reliable estimates, but rather as indications of qualitative trends observed in the spectra.

The key observations made in the analysis of the spectra for different ρ are confirmed. In subjects where the SAT thickness is < 8 mm (#4, #8, #9) the total Hb content is high and increases for increasing ρ , as a clear indication that the muscle tissue is probed (tHb >30 μ M for $\rho = 3$ cm). This is an expected effect and of course must be carefully considered when studying the adipose tissue to avoid contamination from the underlying muscle.

The more unexpected contamination from the thin superficial skin layer seems to be confirmed by the tabulated values, since in subjects with a greatest thickness (>10 mm, that is all cases except the three subjects mentioned above) an increase in water content is observed for the shortest ρ , with the only exception of Subject #6 at $\rho = 30$ mm). For the previous 3 subjects the muscle contamination is possibly dominant and overwhelms the water increase at shorter ρ .

The comments on the scattering spectra reflect in Table 4.2, where $\rho = 1$ cm always shows the highest value for b, supporting again the contamination of the skin. Indeed, $b > 1$ is an indication of steep scattering spectrum arising from small scattering centers as for collagen fibrils [86], whereas adipose tissue with large adipocytes (where a lipid droplet can represent up to 90% of the cell volume) exhibits a flatter ($b < 1$) spectrum.

4.4 Broadband Simulation of Multi-distance measurements on the Abdomen:

To help interpret the results from this campaign, simulations were performed assuming a simple three-layered model of the abdomen with the three layers being i) skin ii) SAT and iii) underlying muscle layer. The base optical properties and constituent concentrations of the individual layers were fixed to values obtained from literature. The average refractive index values for the three layers were assumed to be constant over the wavelength range of interest and chosen to be 1.38 for skin, 1.44 for the SAT and 1.37 for muscle. Regarding the optical properties spectra, the values for the skin or dermal layer were obtained from literature [88] while those for the muscle were estimated assuming the constituent concentrations to be 14.5 g/dL of blood, 5% lipids, 80% water and 15% collagenous protein [71]. Finally, the SAT was assumed to comprise 95% of lipids

Chapter 4. *In vivo* Application of Broadband DOS for Layered Media: Abdominal Adipose Tissue

and 5% water with negligible concentration of blood. The estimated absorption and retrieved scattering coefficient spectra have been plotted in Fig. 5.

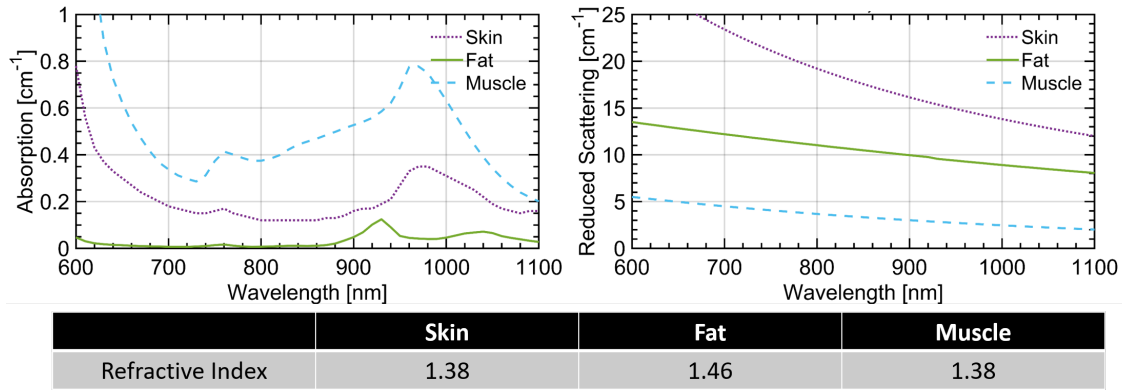


Figure 4.5: Absorption (left) and reduced scattering (right) spectra of the three primary layers of the abdominal tissue (namely skin, SAT and underlying muscle) used in the simulation studies. Tabulated below are the refractive indices for each of the layers.

The key trends observed in the *in vivo* measurements are

- increase in blood-related absorption for the largest ρ when the SAT is thin (< 8 mm);
- increase in water content for short ρ ;
- and, increase in scattering slope for short ρ

The first effect is consistent with the probing of muscle tissue, while the other two with a contribution from the skin. Since this latter statement is less obvious, we ran a set of Monte Carlo simulations on possible scenarios in order to corroborate our hypothesis. We tried to match as much as possible the measurement conditions (e.g., convolution with the IRF, number of counts, geometry) and analysis (homogeneous model, fitting range) so to closely replicate the experiment. As for the tissue structure (layers) and optical properties we inferred values from the literature or from realistic assumptions displayed in Fig 4.5. Four possible scenarios are considered, spanning over all combinations of thin (15 mm) and thick (40 mm) SAT layer with thin (1 mm) and thick (3 mm) skin.

The resulting fitted absorption and reduced scattering spectra are displayed in Fig 4.6 and Fig. 4.7 respectively. The increase in absorption due to the underlying muscle for a thin fat layer (trend I) is confirmed (Fig. 4.6c and Fig. 4.6d). The water contribution from the skin arising at $\rho = 1$ cm (trend II) is consistent with a skin thickness of 3 mm (Fig. 4.6b) and is possibly masked for the same skin thickness when the muscle is visible (Fig. 4.6d), similarly to what observed *in vivo*. Finally, the increase in scattering slope for $\rho = 1$ cm (trend III) possibly due to skin collagen is definitely observed for any skin thicknesses when the fat layer is thick enough to isolate from the muscle. Instead, contamination from the muscle is masking this effect for thin fat layers.

Overall, the simulations confirm the proposed hypothesis that the superficial skin yields a tangible effect in the *in vivo* measurements at least for a thickness of 3 mm

4.4. Broadband Simulation of Multi-distance measurements on the Abdomen:

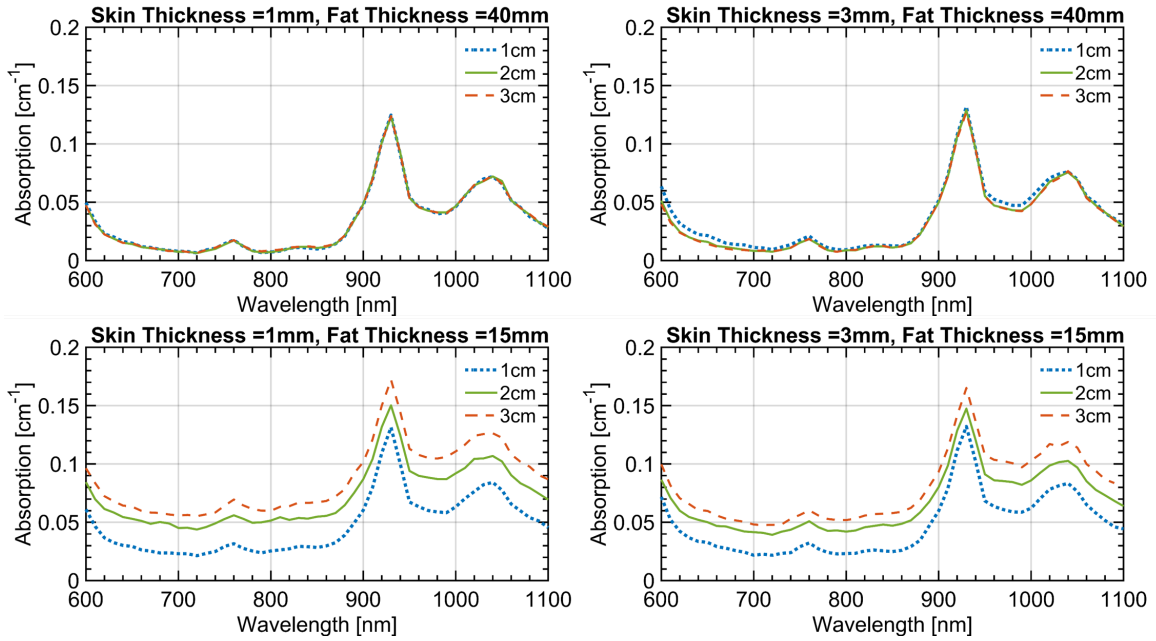


Figure 4.6: Multi-distance absorption spectra retrieved from the simulations for the four different combinations of layer thicknesses. The assumed thickness of the first two layers in each case is mentioned in the title of the corresponding subplot. The third layer was assumed to be infinitely thick in all cases.

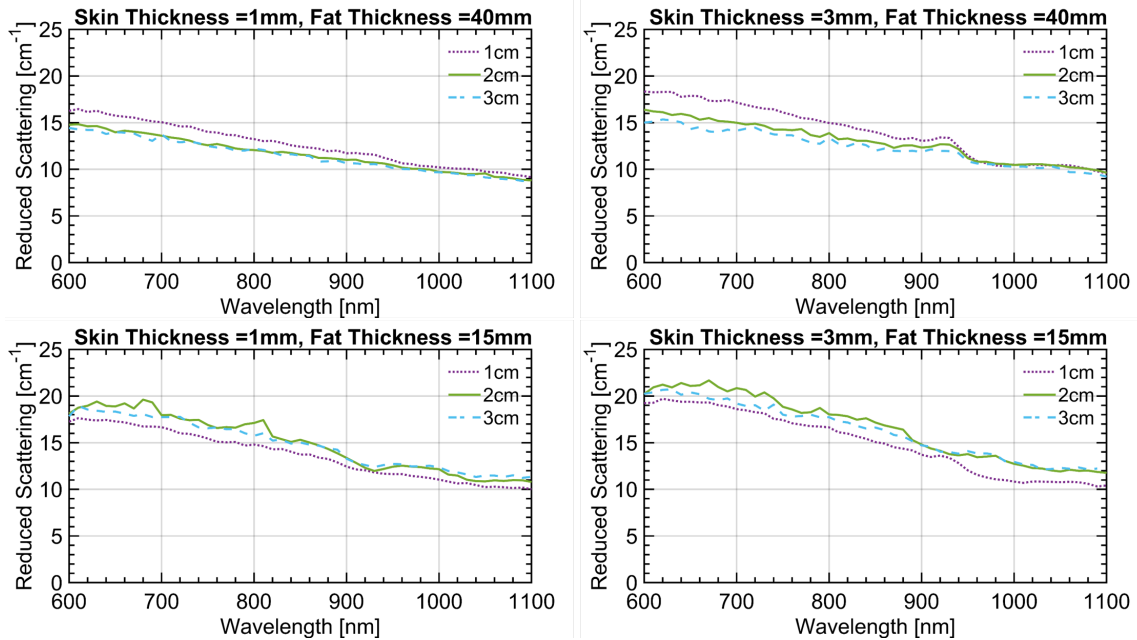


Figure 4.7: Multi-distance reduced scattering spectra retrieved from the simulations for the four different combinations of layer thicknesses. The assumed thickness of the first two layers in each case is mentioned in the title of the corresponding subplot. The third layer was assumed to be infinitely thick in all cases.

or greater. Surely, these simulations are derived using simplified assumptions on the geometry and using literature data for the estimate of layered absorption. Still they

provide an indication of plausibility of our interpretation. Indeed, the *in vivo* effects both on the water increase and, on the scattering slope seem to be stronger than what predicted based on literature information. This may suggest either that the skin thickness is larger than 3 mm or that the skin scattering is higher than the values depicted in Fig.4.6. Incidentally, while these findings make data interpretation more complex, they also indicate that time domain diffuse optical spectroscopy is sensitive enough to skin properties and could be studied more specifically for the non-invasive *in vivo* sensing of skin properties, such as hydration or collagen content.

4.5 Initial application of the two-layered model

The *in vivo* measurements and simulations, both confirm the influence of the superficial dermal layer and the underlying muscle layer in the accurate monitoring of the sandwiched SAT layer. Thus in principle, using a three layer analysis model that could estimate not just the optical properties of the three layers involved but the thicknesses of the first two layers too, would be the most optimal solution. Such models are scarce[89] and computationally intense. Hence we chose to employ the two-layered analytical model discussed in the previous chapter to these measurements. For this purpose, we chose the data from Subject #7 who has the largest value for SAT layer thickness (35mm). In this case, the situation could be approximated to a two layered one with dermal layer being the superficial one and the SAT being the (optically) infinitely thick bottom layer.

Echograph measurements estimate an average value of about 2.1mm for the thickness of the abdominal derma (skin) for this subject. This value was chosen as the top layer thickness. Analysis was also performed assuming the top layer thickness of 5mm for the sake of comparison. As discussed in the previous chapter, the reduced scattering of the second layer μ'_{s1} was fixed to the value of reduced scattering recovered from the largest ρ . The results of this analysis (only absorption spectra for the layered model) are presented in Fig 4.8. The reference values (used for the above mentioned simulations) are plotted for comparison.

The recovered top layer (Skin) spectra show a clear presence of the water peak. The resultant μ_{a0} spectra recovered at $s_0 = 2.1$ mm shows a narrower peak at centered around 980nm, mimicking the shape of the reference spectra. The analysis at $s_0 = 5$ mm, still shows a significant influence of water peak but with an additional broadening on the left (suggesting a mild influence of the lipid peak at 930nm). Also for $s_0 = 2.1$ mm the model recovers null absorption in the top layer until 900nm. This could possibly be due to a breakdown of the model. The reader must remember that the model ultimately relies on the diffusion "approximation", which necessitates that light is sufficiently diffused in every layer. The very small s_0 makes it difficult to meet this criteria.

The recovered bottom layer absorption spectra shows negligible change between the two fixed s_0 values. These spectra differ from the reference in spectral features mainly at the 980nm. The recovered spectra reflect a presence of water (higher value at 980nm) which is not seen in the reference data. This could be due to contamination from the underlying muscle layer which is not taken into account in this analysis. The magnitude difference between the retrieved spectra and the reference values could be attributed to inter-subject variation or other issues in the model.

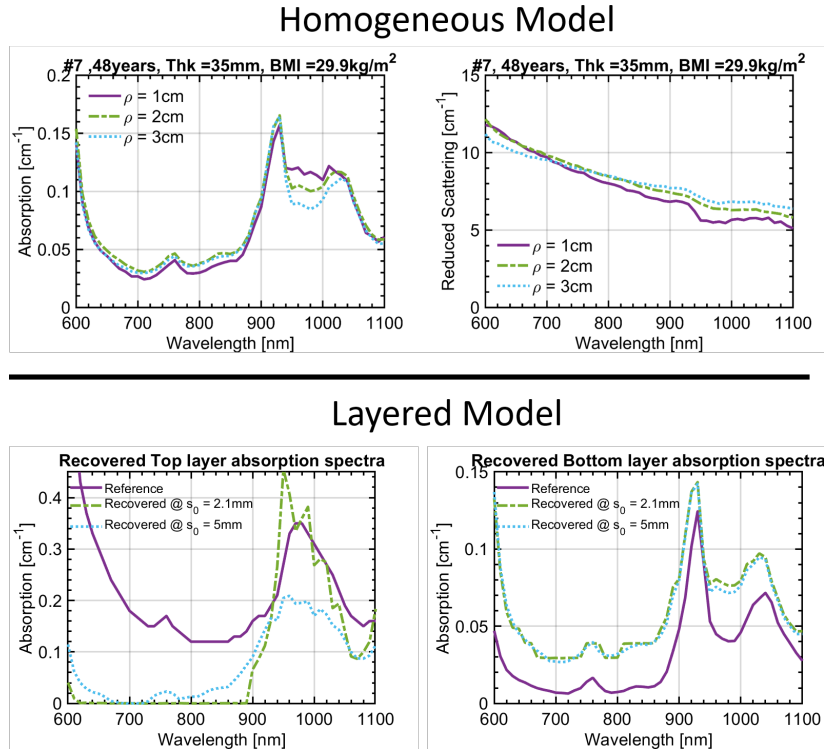


Figure 4.8: Homogeneous and Layered Models of Analysis performed on the data from the subject #7 at the position 8L. The analysis with the layered model was performed fixing the thickness of the top layer to (a) the value estimated using the echograph (2.1mm) and (b) 5mm. The thickness of the bottom layer was assumed to be infinite (echograph estimate = 35mm).

4.6 Conclusions

In conclusion, we have investigated the optical spectroscopy of the abdomen on 10 subjects in vivo using time domain broadband diffuse optics at 3 source-detector distances (ρ). A wide inter-subject variability was observed, related to the specific subject's constitution. Upon changing ρ , three effects were observed, that is: i) the increase in the overall tissue absorption at large ρ ($\rho = 3$ cm), when the superficial adipose tissue thickness is < 8 mm; ii) the increase in water absorption for short ρ ($\rho = 1$ cm); and iii) the increase in the scattering slope again for the shortest ρ . All these findings are consistent with a 3-layer model of the abdomen comprising the skin, the adipose tissue, and the underlining muscle. A proper optical investigation of the adipose tissue should cope with this multi layer structure in order to properly disentangle true fat properties from contamination from the skin or the underlying muscle.

The systematic study presented here was performed primarily using a simple homogeneous model and sets the ground for a more advanced analysis including multi-layered geometries. The two layer model discussed in the previous chapter was applied to the data from a single subject in a purely exploratory fashion. While this further cements the impression about the superficial derma being the key contributor to the water content in the absorption, it is clear that the retrieval of 3 layer properties with proper accuracy is not straightforward and demands a more robust three layer model for better

Chapter 4. *In vivo* Application of Broadband DOS for Layered Media: Abdominal Adipose Tissue

results. Therefore, we are currently validating spectral multilayered approaches for a second-level analysis of the experimental data-set.

In the era of personalized and precision medicine, increasing our knowledge on adipose tissue might enable us to overcome the limitations of the traditional anthropometric indices of obesity and sarcopenia. The availability of a non-invasive technique to monitor adipose tissue status in response of nutrition, lifestyle habits or medical treatment is fascinating for the possibilities of providing feedback and non-invasive insight. Diffuse optics is a potentially powerful option, also in view of the wealth of information it can provide – related to both tissue composition and microstructure. Yet, preliminary understanding of the origin of optical measurements is a pre-requisite for proposing diffuse optics in clinical studies. The present work sets a first observational ground on fat spectroscopy clearly identifying the next step to provide accurate and quantitative optical characterization of adipose tissues.

4.6. Conclusions

Table 4.2: Tissue composition, blood oxygenation, and scatter parameters for all the subjects at the three source detector separations for location at 4 cm to the left of the navel. The scatter parameters are obtained in the wavelength region 650-900 nm.

Subject	Rho	Hb	HbO2	THb	StO2	Lipid	Water	Collagen	Bkg	a	b
	(cm)	μM	μM	μM	%	mg/cm^3			cm^{-1}	cm^{-1}	
#1	1	0.83	10.83	11.66	93	955	216	90	0.001	14.5	1.26
	2	0.2	15.89	16.09	99	969	185	88	0.02	18.7	0.38
	3	0.13	14.4	14.53	99	884	141	75	0.019	13.7	0.44
#2	1	2.86	5.29	8.15	65	664	221	0	0.01	12	1.21
	2	0.09	18.6	18.68	100	1164	154	54	0.02	15.5	0.03
	3	0.07	16.14	16.21	100	1188	43	71	0.015	12.3	0.52
#3	1	2.89	4.9	7.79	63	605	197	0	0.01	13.6	1.08
	2	0	17.08	17.08	100	930	136	22	0.021	14.9	0
	3	0.23	15.56	15.79	99	977	85	30	0.015	12.2	0.43
#4	1	0.33	33.3	33.64	99	994	281	140	0.036	22.2	1.56
	2	0.08	42.52	42.61	100	483	535	143	0.073	23.2	0
	3	0.05	50.25	50.3	100	1247	291	205	0.084	18.9	0.24
#5	1	2.84	5.52	8.36	66	690	236	0	0.01	15	0.83
	2	0.05	19.25	19.3	100	994	108	33	0.024	17.3	0
	3	0.01	18.11	18.12	100	1046	57	43	0.019	13.1	0.29
#6	1	2.9	4.72	7.63	62	574	185	0	0.01	12.4	1.42
	2	0.33	12.21	12.54	97	950	132	35	0.018	16	0.29
	3	2.66	6.62	9.28	71	720	286	0	0.011	11.8	0.67
#7	1	2.9	4.69	7.59	62	568	182	0	0.01	10.3	1.41
	2	0.07	9.96	10.03	99	1171	116	86	0.006	16.7	0.7
	3	0.15	7.89	8.03	98	1085	106	77	0.003	12.9	0.74
#8	1	2.02	32.19	34.21	94	811	10	56	0.031	15.7	1.07
	2	0.01	43.62	43.63	100	824	368	141	0.075	25.7	0.15
	3	0.74	40.71	41.46	98	899	202	133	0.06	15.6	0.18
#9	1	0.27	15.89	16.16	98	1028	145	132	0.002	18	1.48
	2	0.12	25.95	26.07	100	888	312	131	0.062	26.7	0.43
	3	0	30.24	30.25	100	997	203	143	0.049	16	0.36
#10	1	2.9	4.76	7.66	62	583	186	0	0.01	18.6	1.37
	2	0.03	10.81	10.84	100	984	101	57	0.015	19.3	0.33
	3	0.02	8.51	8.53	100	985	75	59	0.008	13.7	0.51

Bkg = Wavelength independent value added as a fitting parameter to account for possible tissue absorbers not included in the fitting procedures and for limitations of the theoretical model | THb = total hemoglobin content | StO_2 = oxygen saturation

CHAPTER 5

Optical Signatures of Thermal damage in Biological tissue - an exploratory study on ex-vivo biological tissue

5.1 Introduction

Thermotherapy, or the use of heat for therapeutic intervention, has shown considerable promise in cancer treatment. Depending on the required localization of the treatment and the severity of the condition, the heat is delivered either non-invasively or in a minimally invasive manner. Based on the nature of the heating source different modalities have been developed such as Radio Frequency Ablation (RFA), Micro Wave Ablation, High Intensity Focused Ultrasound, Laser Ablation, and Cryoablation [90]. RFA is a minimally invasive treatment where a needle probe is inserted percutaneously into the tumor or malignant tissue. An alternating current is then applied through the needle probe inducing ionic agitation and localized heating of the tumor site. This controlled heating, administered properly, could then lead to coagulative necrosis [91] confined to the malignant tissue. Thermotherapy in general and RFA in particular have garnered sufficient interest in the last decade and are now routinely used to treat cancers in the liver, lungs, breast, and bone[92]–[94]. The minimally invasive nature of the RFA technique makes it particularly attractive at a time where quality of life and minimizing discomfort of the patient are key priorities.

However, with the possibility of incomplete ablation of the target tissue, there is a high chance of recurrence of disease. A study on liver cancer treatment with RFA reported a recurrence rate as high as 47% [95] and about 20-40% of the patients treated for atrial fibrillation underwent a second ablation [96]. This kind of incomplete treatment could primarily be attributed to two factors. The first one is the cooling of the

Chapter 5. Optical Signatures of Thermal damage in Biological tissue - an exploratory study on *ex-vivo* biological tissue

ablation region by large blood vessels known as the heat sink effect while the second one is the carbonization around the electrode due to desiccation at high temperature inhibiting further heating[97]. To overcome these issues there is a definite need to accurately monitor the RFA procedure in real time and have reliable markers demarcating the degree of thermal damage sustained by the tissue at a given point of time during the treatment. Different imaging based techniques like Ultrasound, Computed Tomography and MRI are routinely used in real time for guidance in needle placement. However these modalities provide limited success in the direct assessment of the extent of thermal damage and underestimate the lesion size [98], [99]. Methods based on temperature or tissue impedance are also considered for this purpose. Using thermocouples a continuous feedback on the temperature at the ablation/treatment site can be obtained during the treatment, similarly impedance measurement detects the end point of treatment by the variation in resistance provided by the tissue to current. These methods too suffer from inaccuracies arising mainly due to the heterogeneous nature of the tissue and the variation in the tissue properties during treatment [100].

Optical spectroscopy of tissue could offer an interesting alternative in this regard. As discussed earlier, optical techniques are sensitive to the tissue morphology and physiology of the biological tissue and do not depend on the cellular energetics. Thus different optical techniques have been utilized to study the effects of thermal damage on tissue and multiple studies have demonstrated the ability of such techniques in distinguishing thermally damaged and native tissue. Notable among these are diffuse reflectance and transmittance [101]–[103], fluorescence [101], visible light spectroscopy[104] and in some cases optical properties[105]–[110] (obtained using CW techniques). Constant temperature saline baths and Laser induced thermotherapy were some of the techniques used initially to induce heat into the sample (tissue) while the later studies used RF based techniques for this purpose. Thus investigating the capability the TD-DOS technique and particularly, the use of a broadband instrument like the one developed in Chapter 2 could be of great interest and has the potential to open up a range of novel applications for TD-DOS instrumentation. Thus, in this work, we employ a broadband TD-DOS instrument to investigate real-time changes in the optical property spectra of a variety of *ex-vivo* animal tissue as they undergoing thermal treatment.

Prior to this, a database of optical properties of different porcine tissue and organs *ex-vivo* was accumulated measuring the optical property spectra of nearly all the organs and tissue that sufficiently describe the porcine anatomy. This characterization was performed maintaining the tissue or organ at room temperature. This initial undertaking permitted us to understand the spectral features and average values of optical properties of the different organs and tissue. Based on this information, we chose a subset of organs and tissues (*ex-vivo*, bovine) which were then used to study the influence of thermal damage on the optical properties. A detailed description of the kind of tissues and organs and the method of heat delivery will be discussed in the forthcoming sections. Bovine tissues and organs, on an average, are larger than porcine ones and thus provide more volume of tissue that would be necessary for the more intensive experiment on thermal damage.

The systematic characterization of the optical properties of porcine organs *ex-vivo* is an interesting study by itself since the knowledge can be put into designing biological phantoms (similar to the one used in 3.3). In comparison with the synthetic phantoms

5.2. Optical characterization of *ex-vivo* Porcine Tissue

(like those discussed in 3.3) these phantoms might be difficult to prepare and maintain. However, synthetic phantoms mimic rather poorly the mechanical properties and real and complex heterogeneities present in human organs. In contrast, biological phantoms, made from animal tissues, demonstrate better the degree of heterogeneity and morphological complexity common in biological tissues [111]. Further, they have a set of major chromophores typically present also in human tissues that are not easily modelled with synthetic phantoms. *Ex-vivo* animal tissue (e.g. porcine) is thus a valuable alternative as it is easy to procure and presents a relatively lower level of hazard as compared to human tissue *ex-vivo*

This work was performed in collaboration with our partners from the Multi-Modality Medical Imaging (M3I) research group of University of Twente and STFC Rutherford Appleton Laboratory, Didcot, United Kingdom. The measurements were performed within the range of 650-1100 nm. The first, room-temperature characterization of the was performed with nine different porcine organs. The second phase of the study, aimed at monitoring the thermal treatment was then performed on four types of tissue, which are *ex-vivo* bovine liver, heart(myocardium), muscle and brain. the study was performed at two target temperatures corresponding to critical treatment (70°C) and over-treatment (105°C) scenarios. The optical properties of the tissues were also monitored during the passive cooling of the tissue for a time span of about an hour. Key variations are observed in both absorption and reduced scattering spectra which could be particularly interesting in the non-invasive, real time monitoring of the RFA procedure.

5.2 Optical characterization of *ex-vivo* Porcine Tissue

5.2.1 Measurement Setup, Samples and Analysis

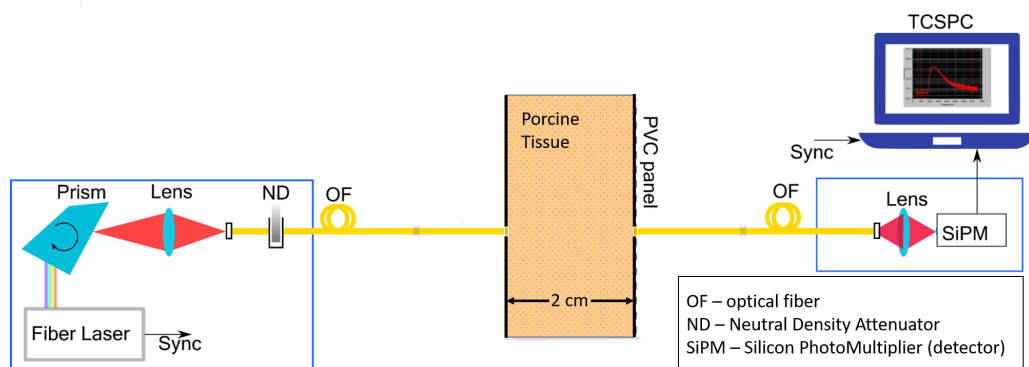


Figure 5.1: Schematic of the of time resolved diffuse optical instrumentation used for the preliminary characterization of the porcine tissues.

Fig. 5.1 shows a schematic of the instrument used for the preliminary, room-temperature characterization of the porcine tissue. The system is a slightly different realization of the instrument described in Chapter 2 with only the SiPM (Silicon PhotoMultiplier) detector and the capability to perform the measurements in transmittance. A brief de-

Chapter 5. Optical Signatures of Thermal damage in Biological tissue - an exploratory study on ex-vivo biological tissue

scription of the setup is given here. A fiber-based supercontinuum laser (SuperK EXTREME (EXW-12), NKT Photonics, Denmark) was used as the illumination source. Broadband picosecond pulses (450 – 1750 nm, repetition rate = 40 MHz) from this source were impinged on a dispersive Pellin-Broca prism that achieved wavelength selection through rotation. This wavelength-selected light was then focused into a 50 μm graded-index fiber. A set of neutral density circular attenuators were used to control the light power. Thus, after sufficient attenuation, the light was coupled to a 1 mm step-index fiber in gentle contact with the sample. Light diffusively *transmitted* from the sample was then collected using another 1 mm step-index fiber and was focused into a custom made Silicon PhotoMultiplier (SiPM) module with a good photon harvesting capability over the wavelength range of interest (650 – 1100 nm). The sample is sandwiched between two black PVC panels locked in place using nylon screws on all four corners. This helped to keep the thickness intact and avoid any movement or sliding of the sample. Care was taken not to squeeze the sample, which could change its structural and optical properties. The PVC panels had two small openings of 1mm diameter at their centers to house the injection and collection fibers on either side of the sample.

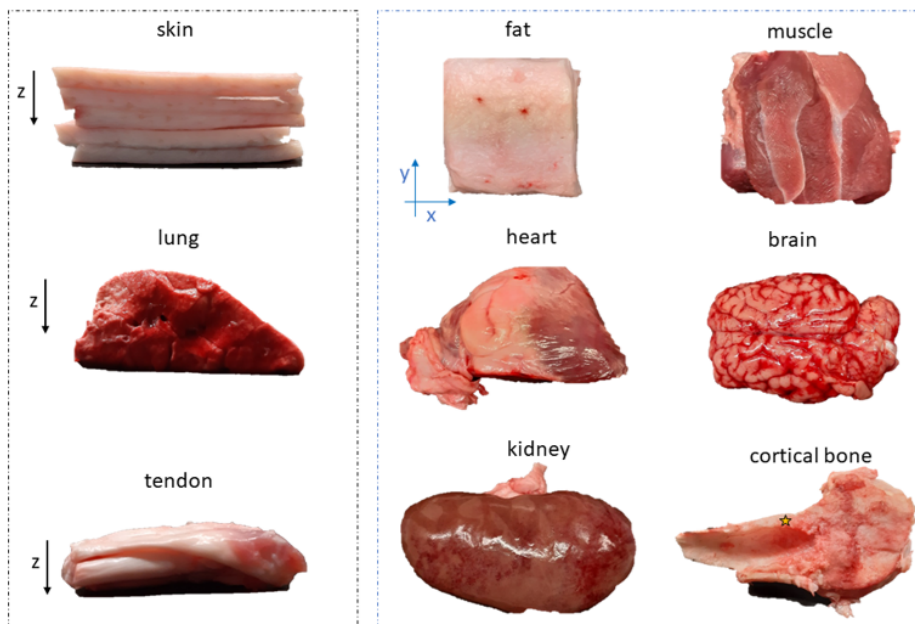


Figure 5.2: Images of the different porcine samples considered for the study. The measurements were always performed in transmittance along the z -direction. The position along which the measurement was performed on the cortical bone is demarcated with a yellow star

Samples: Images of the different ex vivo porcine samples considered for this study are presented in Fig. 5.2. Samples were refrigerated until before measurement (approx. 4°C). Just before the measurements they were allowed to passively return to the room temperature (21°C). The different repetitions for all the tissues were performed in three days, within six days of sacrificing the animal. The measurements were performed on a portion or on the whole organ tissues. The measurements were performed along the z -direction (refer to z values reported in Table 5.1). The values of the thickness were chosen after some initial trails, as a good compromise between the signal level over the

5.2. Optical characterization of *ex-vivo* Porcine Tissue

entire spectrum and the validity of the diffusion equation. Also, the lateral dimensions (x and y in Table 5.1) were chosen to be as large as possible to avoid boundary effects.

Samples	Geometrical dimensions (cm)			Comment
	z	x	y	
Skin	2.2	5.5	6	Overlap of 5 layers
Fat	2	6.3	6.5	Overlap of 2 layers
Muscle	2	7.5	6.5	Portion
Lungs	2	7.5	6	Portion
Heart	2	4.5	5.5	Portion
Brain	2	9.8	6	Whole organ
Tendon	1	6.1	2.1	Overlap of 6 cuts
Kidney	2.5	14	8.5	Whole organ
Bone	0.8	4.5	2.7	*Refers to a cortical bone segment

Table 5.1: List of porcine samples. All measurements were performed along the z - direction.

Measurements and Analysis: The measurements of the *ex vivo* porcine tissues were performed in transmission geometry along the z dimension of the sample (Table 5.1) in the spectral range from 650 nm to 1100 nm with a step-size of 10 nm. Measurements were performed on three different locations of each tissue to account for intra-sample spatial variation of the optical properties.

The acquired TPSFs at each wavelength were fit to an analytical solution of the Radiative Transport Equation under the Diffusion Approximation with extrapolated boundary conditions to retrieve the optical properties of the tissue (described in 1.6.1). The sample is considered to be a homogeneous infinite slab, i.e. a fixed thickness along the z-direction while infinitely expanding in the other two directions.

5.2.2 Optical Property Spectra

The absorption (black dots) and reduced scattering (red squares) spectra of the nine types of tissue considered for this study are presented in Fig. 5.3. The mean values of the three spatially separated measurements are plotted with the standard deviation represented as error bars. Two spectral peaks are observed consistently over most of the tissue types considered (except for the fat tissue). These are, i) a clearly distinguishable peak at 980 nm and ii) a relatively smaller and subtler peak at 760 nm. Both peaks have been well characterized and have been attributed to the water and blood content of the tissue, respectively. Other specific features are the double peak at 930 nm and 1040 nm for the fat tissue. This was discussed briefly in the previous chapter and is representative of the lipid content. The relatively broader peak around 980 nm for the bone which could be due to a combination of water and high amount of collagen present in this type of tissue. Also, the high absorption observed in some of the tissue types close to the red spectral range (around 650 nm) can be a signature of a higher blood content in these tissues.

A smoothly decreasing trend with wavelength is observed for the reduced scattering coefficient spectra, in general, for all the tissue types. The slope of the reduced scattering spectra shows a marked variation amongst the different tissue types (red dots in Fig. 5.3). Tendon and Skin tissues display a steep decrease in the reduced scattering coefficient with wavelength compared to the other tissue types. The lung tissue, on the

Chapter 5. Optical Signatures of Thermal damage in Biological tissue - an exploratory study on ex-vivo biological tissue

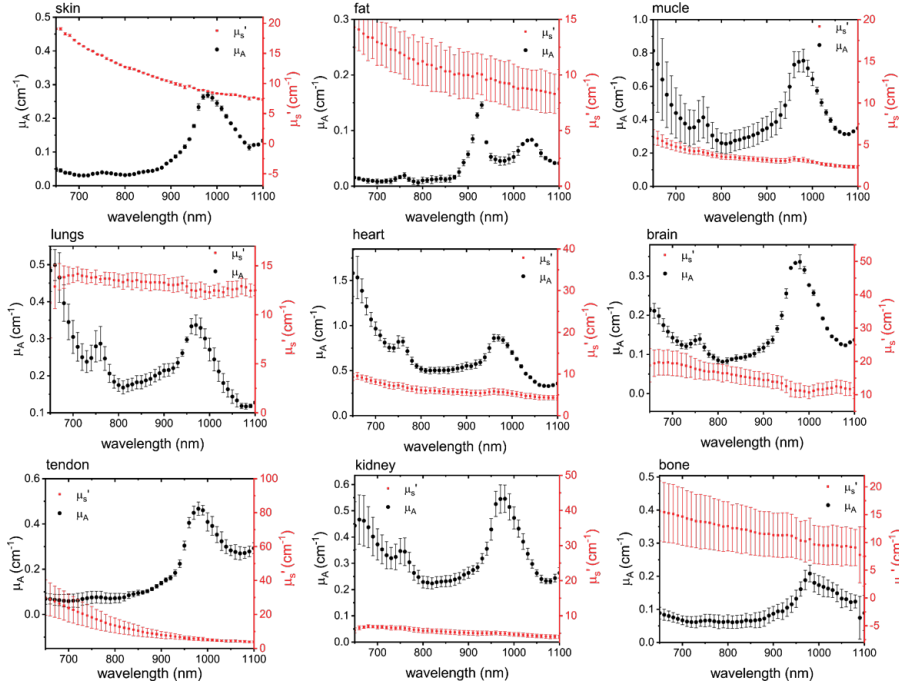


Figure 5.3: Absorption (black dots) and reduced scattering spectrum (red squares) of the 9 porcine samples. Values results as average of three repetitions, y-error bars display the standard deviation.

contrary, shows the least change in the reduced scattering coefficient with increasing wavelength. Sufficient dispersion is observed in the magnitude of the reduced scattering coefficient spectrum. The brain tissue presents a higher magnitude of reduced scattering ranging between 20 to 15 cm^{-1} . This could be attributed to the unique structure of the brain tissue. The muscle tissue has a reduced scattering coefficient under 5 cm^{-1} over the entire range. This huge variation, both in the magnitude and shape of the reduced scattering coefficient spectra, among different tissues could be due to the difference in the shape and structure of the scattering centers of the different tissues considered.

This first phase study on the room temperature characterization of the different organs proves the capability of our instrument to measure with good accuracy the optical properties of any of these organs. Hence, we chose the following subset of tissues and for the experiment on monitoring the thermal damage in the tissue: the muscle tissue, heart (myocardium) tissue and the brain tissue. Another tissue type not present in the characterization presented above but used for the thermal damage study is the liver tissue. The choice of these tissue types was based on the applicability of the proposed method of heat treatment used for this study. In this experiment, we chose to employ the radio frequency ablation (RFA) technique to instigate the thermal damage in tissue. This technique has gained sufficient interest for the treatment of cardiac arrhythmias [112] and is a common treatment methodology employed for liver tumors [113]. RFA is also performed for pain relief and lesion treatment in soft tissue and musculoskeletal system validating our choice of studying the muscle tissue [114]. Moreover, the minimally invasive nature of the technique makes it really interesting for the treatment of brain tumors and is currently being tested on animal models [115], [116]. However the

5.3. Optical characterization of thermal treatment using Radio Frequency Ablation (RFA)

brain tissue is very delicate and this calls for a high degree of safety while implementing this procedure. This makes the cerebral cortex and other regions of the brain an interesting choice for our study as well.

5.3 Optical characterization of thermal treatment using Radio Frequency Ablation (RFA)

5.3.1 Measurement Setup, Samples and Analysis

A schematic of the measurement setup is shown in Fig. 5.4. The schematic is exactly the same as in the previous case (for the characterization of the porcine meat samples). The instrument is used in conjunction with the RFA instrument as seen in the figure.

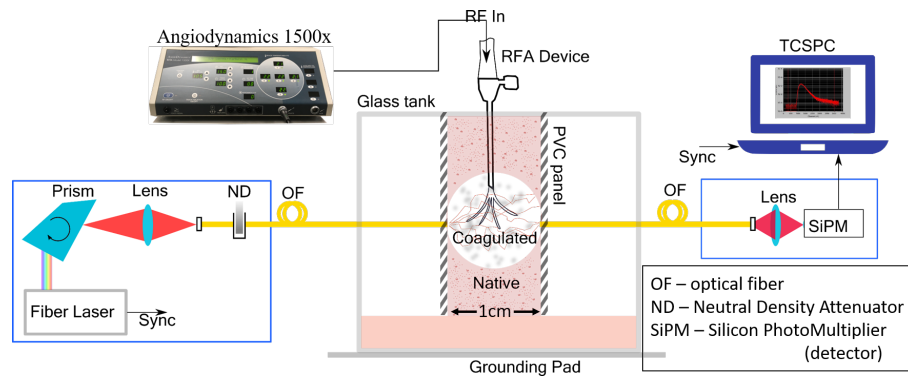


Figure 5.4: Schematic of the setup. The ex vivo tissue sample was held between two PVC plates and the Radiofrequency (RF) needle/electrode was inserted to the center. A grounding pad was attached to the aluminum base of the glass tank as the second electrode. A layer of chicken breast tissue on the grounding pad allows for a uniform dissipation of the electric current. An alternative current was applied between the two electrodes to heat the tissue and optical measurements were performed simultaneously.

The RF instrument (Angiodynamics, USA) used comprised of an RF generator 1500X, generating an alternating current of 460 kHz through the applicator device (Starburst XL, Angiodynamics) towards the grounding pad completing an electric loop. The applicator device, a metal electrode, is inserted into the tissue, which is placed on a bed of chicken breast tissue which is then placed on the grounding pad. The bed of chicken breast tissue ensures a uniform dissipation of electric current and consequently heat energy through the sample before draining into the grounding pad. The RF applicator device is equipped with multiple tines which can be deployed once it is in the tissue. This ensures a uniform distribution of energy in a spherical region of ablation/treatment. Five thermo-couples present on the tip of the tines allow for a constant monitoring of the average temperature of the treated region. The presence of the metallic electrode had a negligible influence over the tissue optical properties, moreover, since the aim of the experiment is to monitor the evolution of optical properties of the tissue during the treatment, the relative variation w.r.t their native values is of greater interest than their absolute value.

Sample Preparation: Four ex-vivo tissue types were used in the ablation measurements: Veal muscle and bovine: brain, heart(myocardium) and liver. The tissues were

Chapter 5. Optical Signatures of Thermal damage in Biological tissue - an exploratory study on ex-vivo biological tissue

taken from a local butcher and moved in a portable refrigerator to the laboratory. Contact with water was avoided. Samples for investigation were pre-cut into slices of 1 cm thickness and roughly 7x7 cm to match the dimensions of the PVC slabs which held them in place. Samples which were not used immediately after procurement were placed under vacuum and refrigerated at a temperature of 1.5-2°C. The maximum wait period between procurement and usage was 5 days.

Geometry: As in the case of the porcine tissue, transmittance geometry (along the 1 cm thick dimension) was chosen since that would allow for a precise and easy localization of the treated area from the measurement point of view and also ensure complete interaction of the detected light with the region of tissue undergoing treatment. This can also be achieved in reflectance (depending on the inter-fiber distance) and would be the more practical choice when this objective is realized in an *in-vivo* scenario.

Temperatures: Treating a tissue at temperatures between 60 -100°C, leads to immediate coagulation but beyond 100°C the tissue suffers from charring, which influences the efficiency of the ablation procedure. Since this is aimed to be avoided it would be essential to observe and record the optical property evolution of the different tissue types at this temperature. Therefore two temperatures were chosen for the experiment, 105°C corresponding to an over-treatment scenario for the above mentioned reason and 70°C corresponding to a regular treatment scenario.

Types of treatment: For each tissue type two kind of measurements were performed.

- *Spectral Evolution:* a total ablation time of 10 minutes was considered (after about 3 minutes of time necessary to reach target temperature). The settings of the instrument were optimized to achieve a spectra in the region 650-1100 nm with a step size of 10 nm in exactly 60 seconds. Thus a total of 13 spectra were obtained during the 10+3 minutes of treatment time, with a spectral measurement obtained before (on the native tissue) and at the end (completely ablated tissue)
- *Temporal Evolution:* The previous set of measurements, while abundant in spectral information are sparsely placed in time (once every minute). To overcome this, measurements were performed at only 5 wavelengths (770 nm, 840 nm, 910 nm, 970 nm, 1060 nm). The limitation on the wavelength allowed for measurement once every 10 seconds over a span of 10 minutes. The choice of wavelengths will be discussed in a later section.

Analysis: The stochastic Monte-Carlo (MC) based fitting routine, outlined in Chapter 1 and utilized in Chapter 4 for the fitting of the data from the abdominal SAT measurements, was employed in the case of these experiments as well. As in Chapter 4, the data was fit initially both to the analytical solution based on the diffusion approximation and the MC method, but the MC method was found to be more in-line with the requirements especially since the measurements were performed in transmittance (thickness of 1cm, which means lower 'diffusion' in the direction of propagation relative to measurements in reflectance) and the samples under consideration exhibit relatively lower values of reduced scattering.

5.3.2 Spectra of Optical Properties before and after thermal treatment:

Fig. 5.5 summarizes the absorption and reduced scattering spectra of the four different tissue types after 10 minutes of treatment at the two target temperatures of 70°C and

5.3. Optical characterization of thermal treatment using Radio Frequency Ablation (RFA)

105°C. The spectra of the native tissue (with the needle in position) are also presented for comparison.

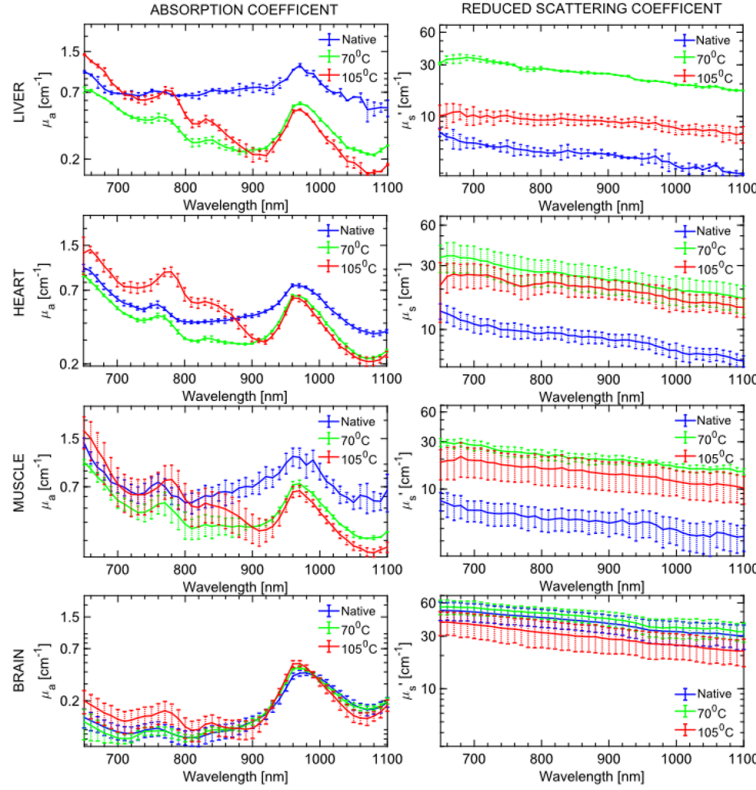


Figure 5.5: Optical properties of native and coagulated tissue. Broadband absorption and reduced scattering coefficient spectra of native (blue) and coagulated bovine (a) liver, (b) heart, (c) muscle and (d) brain tissues. The treatment was performed at two temperatures 70°C and 105°C (green and red respectively). The spectra represent mean values of measurements performed on 3 different samples for each tissue type and the error bars show the standard deviation over the three measurements.

While the liver, muscle and myocardium tissues present on average a higher absorption (0.6cm^{-1}) and lower reduced scattering coefficient (6cm^{-1}), the brain tissue exhibited lower absorption (0.2cm^{-1}) and a much higher scattering coefficient (40cm^{-1}) in the native state. The spectral features that stand out in the case of the absorption spectrum of the native tissue, irrespective of the tissue type, are the well-known blood and water peaks (@ 760 and 980 nm) respectively.

In general absorption coefficient experiences an evident reduction with thermal treatment (with the exception of the Brain tissue). The key variations in the absorption spectra can be observed to clearly effect two wavelength windows, the region from 650-900 nm and the 900-1100 nm region. In the former, treatment at either of the temperatures leads to formation of a new peak at 830 nm. Also the blood peak (@760 nm) seems to experience a subtle 'red' shift which increases for the higher temperature. In the wavelength region (900-1100 nm) key variations are observed around the water peak in the form of a drastic reduction in absolute value, a very subtle 'blue' shift of the peak. Also the peak tends to narrow with thermal treatment. One key difference between the treatment and the over-treatment scenarios is that in the 600-900 nm region the absorp-

Chapter 5. Optical Signatures of Thermal damage in Biological tissue - an exploratory study on ex-vivo biological tissue

tion seems to experience a further increase in absolute value on over-treatment (105°C), most of the times overshooting even the native tissue's absorption value.

On the other hand, the reduced scattering coefficient is devoid of any spectral features over the entire wavelength range and follows the expected power law dependence on wavelength given by the Mie's law of scattering. With treatment this coefficient uniformly experiences an increase. Again here the spectra at (105°C) seems to have a value slightly lower than that of treatment at (70°C) suggestive of a further decrease with over-treatment.

The differences between the optical properties of the native and coagulated tissue become more evident when observed with the spectral evolution during the treatment and hence will be discussed in detail in the next section. In the interest of brevity data and figures presented hereafter will be focused on the bovine myocardium (heart muscle) tissue, however, they conclusions are more or less true for all the tissue types considered.

5.3.3 Spectral evolution of Optical Properties during thermal treatment

Fig. 5.6 shows the time evolution of the optical property spectra of bovine heart tissue during the ablation procedure at two temperatures, 70°C and 105°C over a period of (3 + 10) 13 minutes. In both the cases a treatment time of a little under three minutes is required to reach the necessary target temperature. Following this, the tissue is ablated at the target temperature for a span of 10 minutes.

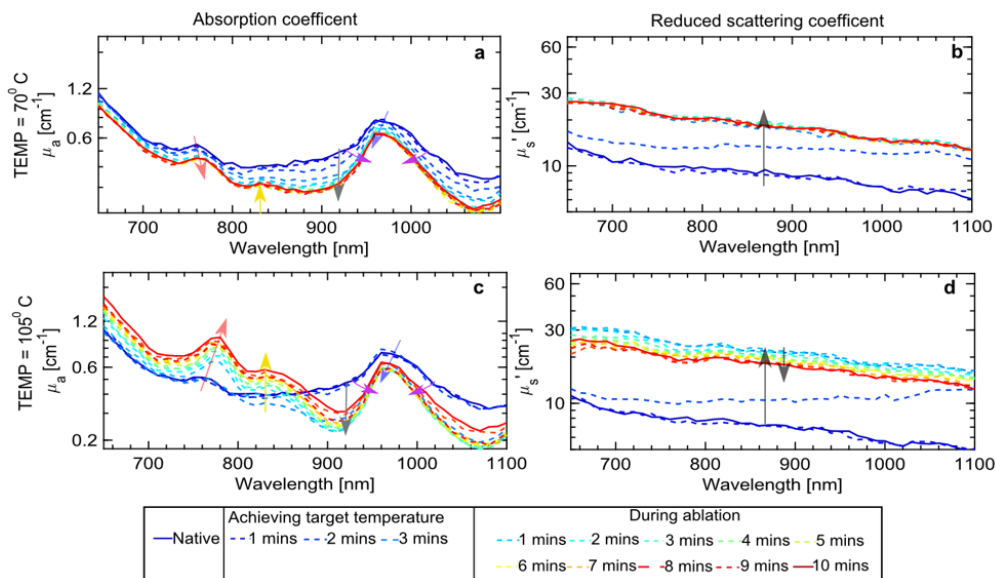


Figure 5.6: Evolution of optical property spectra with RF treatment - Broadband absorption (a and c) and reduced scattering coefficient (b and d) spectra of bovine heart tissue during the RF based thermal treatment at the two temperatures. The native tissue spectra are always plotted in blue line. As mentioned earlier, the acquisition time per one spectrum is 1 minute. The RF instrument takes a time of less than 3 minutes to achieve either of the target temperatures. Once the target temperature is achieved the RF device treats the tissue by fixing the temperature for a span of 10 minutes. Hence in total a set of 13 spectra are acquired during the RF based thermal treatment.

The absorption spectrum, in general, experiences a decrease in absolute magnitude

5.3. Optical characterization of thermal treatment using Radio Frequency Ablation (RFA)

with increasing treatment time. Four key features are observed commonly for both the treatment temperatures albeit with different magnitudes, these are:

1. 'Redshift' of the deoxy-hemoglobin (Hb) peak with increased treatment time.
2. A mild 'Blueshift' of the water peak (980 nm) along with the reduction of the absorption peak width.
3. A reduction of the absorption coefficient value around the water peak region (980 nm)
4. Occurrence of the new peak at around 840 nm, more evident in the case of treatment at 105°C

Additionally, over treatment (@ 105°C) leads to a fifth interesting change in the absorption spectra which is the

5. **further increase in the magnitude** of the absorption coefficient with increased treatment time.

This increase too, is not uniform over the wavelength region but seems to have an almost exponential dependence on the wavelength, overshooting the native value below the 850 nm wavelength while the increase is relatively lower at the longer wavelengths.

The reduced scattering spectra, in both cases (Fig. 5.6(b) and Fig. 5.6(d)), mainly exhibit a visible increase in their magnitudes with the RF treatment. For both treatment temperatures, a **drastic increase** in the reduced scattering is observed during the first three minutes (time taken to achieve the target temperature). When treated at 70°C, the reduced scattering coefficient spectrum reaches a maximum value within the first 3 minutes, i.e. the time required to achieve the target temperature and hardly experiences changes beyond that. However, over treatment leads to an increase in the reduced scattering for the first three minutes which is then followed by a **gradual decrease** in value over the entire spectral range. In both cases, the spectral shape of the reduced scattering spectrum at two minutes is different from the expected power law dependency but this could simply be attributed to the rapidly transitioning tissue structure during the one minute of time needed for the acquisition of this particular spectrum.

The above mentioned features are, for the most part, consistent with the other three tissue types (in Supplementary Data, refer Fig. B.3). The evolution of the optical property spectra of the muscle tissue is in very good agreement with that of myocardium. In the case of liver tissue, the results are consistent for treatment at 70°C but when treated at 105°C the further decrease in the reduced scattering spectra is substantially larger. Finally, in the brain tissue, contrary to the other three tissue types, we observe an increase in the absorption coefficient and reduction in the reduced scattering coefficient.

5.3.4 Time Evolution of Optical Properties with thermal treatment:

The evolution of the optical properties at specific wavelengths as a function of treatment time, for the two treatment temperatures, is plotted in Fig. 5.8, this highlights the superiority of TD-DOS technique for this application by showcasing the ability to recover the absorption and reduced scattering values independently and in *real-time*. The variations in the broadband absorption spectra with thermal treatment suggest that

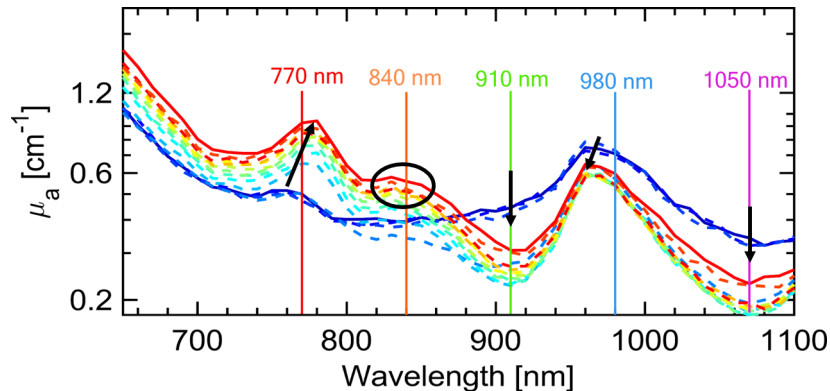


Figure 5.7: Five wavelengths indicative of key variations encountered by the absorption spectrum mentioned above. Continuous, real-time monitoring of the optical properties at these wavelengths are presented in the following section.

the time evolution of the optical properties is very much dependent on the wavelength at which it is followed. To closely observe key effects observed in the absorption coefficient, the time course was measured for the following five wavelengths: 770(*redshift*), 840(*peak formation*), 910(*maximum reduction*), 980(*blueshift*) and 1060 nm (Fig. 5.7). For each of these wavelengths, the measurements were obtained once every 10 seconds for a span of 600 seconds. The 600 seconds of measurement also include the initial three minutes required to reach the target temperature for thermal treatment.

Fig. 5.8(a) and (b) compares the time evolution of both the optical properties at 770 and 910 nm for a treatment temperature of 70°C and 105°C. The reader is reminded that the horizontal time axis (bottom) is plotted in logarithmic scale to better appreciate the time evolution of the heating process which is non-linear. The temperature (average of the four times) is marked (top) at specific points in time. The temperature follows a rather linear increase till the target temperature is reached and remains constant beyond. The absorption and reduced scattering at the two wavelengths are plotted to the left and right axes respectively (normalized to the corresponding native tissue values)

To summarize, key features observed here are with treatment at 70°C (Fig. 5.8(a)) are:

- a gradual decrease is observed in absorption coefficient with increasing treatment time. The trend is similar at both wavelengths.
- The target temperature is reached around 150 seconds into the treatment but the absorption coefficient continue to decrease.
- During the first 50 seconds, the reduced scattering coefficient remains constant and almost equal to the value of the native tissue.
- Beyond this, and at a temperature of about 50°C it observes a sharp increase until the target temperature (70°C) is reached and continues to increase (at a lower pace) beyond. This is sustained for the length of treatment time (600 seconds).
- In general, the evolution of reduced scattering is mostly independent of wavelength.

5.3. Optical characterization of thermal treatment using Radio Frequency Ablation (RFA)

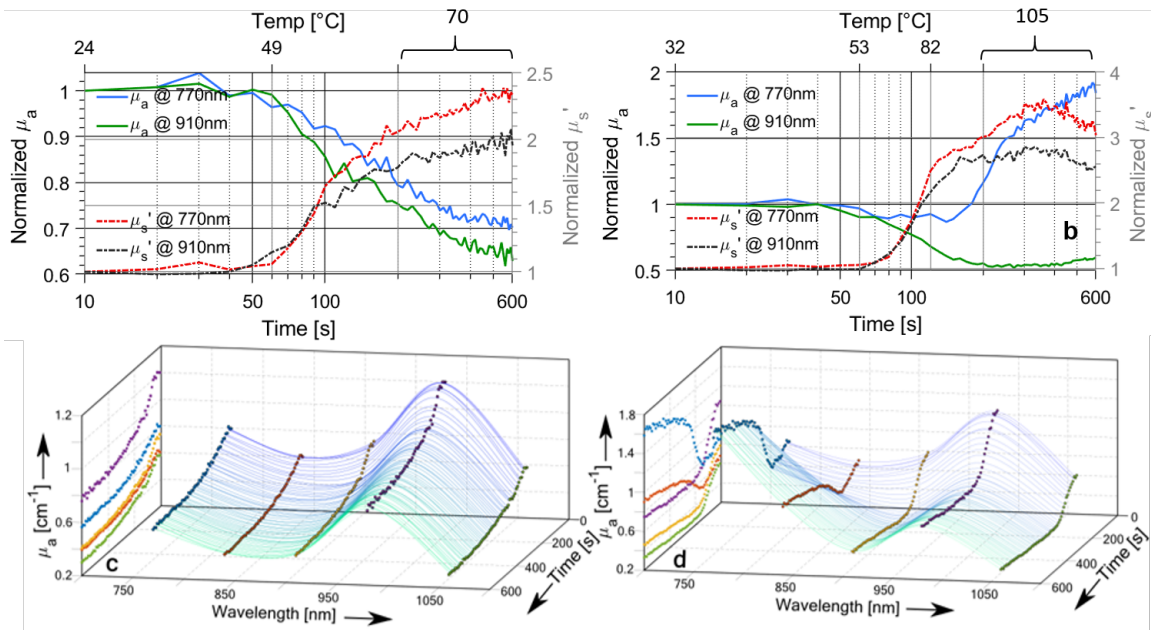


Figure 5.8: Time evolution of optical properties at select wavelengths with RF treatment A total of five wavelengths (770,840,910, 980 and 1060 nm) were chosen to monitor closely the key spectral changes observed in Fig. 5.6. Fig. 5.8 a and b chart the variation of both the optical properties at two (770 and 910 nm) of these five wavelengths for the 70°C and 105°C respectively. The time axes (x-axis) in these graphs are logarithmic and the y axes represents the value of the optical property normalized to the value of the native tissue. The average temperature of the RF electrode at specific time points is given on the temperature axis on the top of each graph. Fig. 5.8 c and d plot the variation of the absorption coefficient over all the five wavelengths with temperatures of 70 and 105°C respectively

- The reduced scattering coefficient at the end of the treatment is a little more than twice the value of the native tissue for both the wavelengths. While the absorption reduces by about 40% for both wavelengths.

In addition to the characteristics mentioned above, the time evolution of the optical properties 105°C (Fig. 5.8(b)) has the following features:

- The absorption at the two wavelengths show distinctive features, while @910 nm the coefficient experiences a decrease with treatment time @770 nm it remains constant for about the first 100 seconds and then gradually increases. Absorption at 910 nm experiences is constant, followed by a period of decrease and finally reaches a plateau region at around 150 seconds thus forming a sigmoid like pattern.
- After 150 seconds when the target temperature is reached the increase in reduced scattering becomes negligible and it reaches a plateau.
- after about 300 seconds from the start of treatment the reduced scattering at both wavelengths seems experience a subtle reduction with treatment time.
- The reduced scattering coefficient at the end of the treatment is a about three times the value of the native tissue for both the wavelengths. While the absorption

Chapter 5. Optical Signatures of Thermal damage in Biological tissue - an exploratory study on ex-vivo biological tissue

reduces by about 50% @ 910 nm and increases by 100% at 770 nm.

As in the case of the evolution of the broadband spectra with treatment, here too we observe a similarity of trends for the cases of liver and muscle tissue (in Supplementary Data, refer Fig. B.4). For reduced scattering both tissues display the sigmoidal shape with time as discussed above. However, the decrease of the value at later times for treatment at 105°C is very evident for both these cases. In the case of brain tissue, we again observe a variation in the trends. At 70°C the relative change between the native and coagulated tissue's absorption coefficient is negligible. The reduced scattering still follows a similar evolution as for the other tissue types at 70°C but experiences only a 20% increase in magnitude over the treatment time. At 105°C, the optical properties of the brain tissue do not follow the sigmoidal evolution observed in all the tissue types. Rather the absorption at 910 nm and reduced scattering at both the wavelengths monotonically decrease with time with a minor change around the 100 second mark. The absorption at 770 nm on the other increases monotonically. The relative magnitude of change in both the optical properties is under 10% over the entire measurement duration.

Fig. 5.8(c) and (d) plot the time evolution of absorption coefficient at all five wavelengths considered for this experiment for a treatment time of 70°C and 105°C respectively. The projections on the time vs optical property plane (left plane for each figure) compares the time courses for all five wavelengths. Since the chosen wavelengths were equidistant for the most part, such a visualization describes both the temporal evolution and spectral evolution of the optical properties, albeit at a lower spectral resolution. Such a plot for the reduced scattering coefficient would be unnecessary since no major spectral variation is expected of the reduced scattering coefficient with treatment.

5.3.5 Discussion on the observed variations

A quantitative description of some of the key variations observed in the optical properties for all the tissue types is summarized in Table 5.2. Since the spectral measurement was performed with a step size of 10 nm the resultant shifts described in the Table 5.2 were obtained on spectra obtained by interpolating the measured spectra with a cubic spline interpolation [117].

Tissue Type		Liver			Heart			Muscle			Brain			
Temperature[°C]		23	70	105	23	70	105	23	70	105	23	70	105	
Red Shift (@760 nm)	(cm^{-1})	-	4	15	-	4	13	-	4	18	-	3	14	
Blue Shift (@970 nm)	(cm^{-1})	-	4	5	-	3	3	-	4	5	-	6	9	
Scatter Parameters	A	(cm^{-1})	5.6	38.2	12.4	6.9	32.4	21.8	12.5	39.5	33.5	49.8	55.8	47.9
	b		1.39	1.53	0.71	1.18	1.35	1.23	1.30	1.44	1.26	1.36	1.30	1.32

Table 5.2: *Quantification of some of the features observed in the different tissue types with RF based thermal treatment at the two temperatures. The scatter parameters A and b are related to the density and size of the scattering components in the medium. From the absorption spectra the relative red-shift in the Hb peak, relative blueshift in the water peak and percentage decrease in the absorption coefficient at 970 nm ('Dehydration') are quantified*

Molecular spectroscopy suggests that changes in the biochemical nature of the tissue constituents would lead to characteristic shifts or formation of new peaks in the spectra while changes in the concentration of the constituent would result primarily in a relative increase or decrease of the property at that wavelength. With this context, it would

5.3. Optical characterization of thermal treatment using Radio Frequency Ablation (RFA)

be reasonable to assume that the peak shifts occurring at 760 nm, and 980 nm and the peak formation at 840 nm could be attributed to changes in the biochemical nature of the different chromophores and constituents of the tissue while the reduction in value around 970 nm could be a consequence of the reduction of water (dehydration) in the tissue with treatment. With the help of existing literature we attempt to understand each of these observations individually and provide some theoretical reinforcements wherever necessary.

With regards to the absorption, in general a decrease is observed in the overall absorption coefficient spectrum with thermal treatment. This result is in compliance with previous studies performed both at specific wavelengths [118]–[120] and broadband spectra [105], [110]. Some of these studies suggest the destruction of different absorbing chromophores like hemoglobin and cytochrome oxidase with heating as a possible reason for this general decrease in the absolute value. Specifically, significant variations in the absorption occur at three spectral regions 1) Around 760 nm 2) Around 830 nm and 3) Around 970 nm. We consider each of these regions individually and discuss these variations in further detail below.

Firstly, the wavelength region around 760 nm. Table 5.2 shows that a *redshift* of roughly 5 nm and 15 nm of the Hb peak is observed in all the tissue types when treated at 70°C and 105°C respectively. A study performed on the chemical and structural changes of whole blood undergoing photo-coagulation [121] come to a similar conclusion regarding a bathochromic shift in the absorption spectra. Integrating sphere pump probe experiments were performed on blood samples undergoing laser photo-coagulation using seven probe wavelengths in 550-1100 nm range. While the observed properties are the reflectance and transmittance profile and the sample itself was pure blood (and not biological tissue), this is the only study (other than the current work) that employs pulsed lasers to study the influence of thermal agitation in biological media. The authors of this work invoke the photo-physics responsible for the electronic absorption bands in hemoglobin to explain this observed redshift. Simply put, they suggest that the redshift is a consequence of "hot bands", i.e. the overlap of vibrationally excited levels of the first electronically excited state with those of the ground state at high temperatures, leading to transitions with lower energy i.e. shift towards the longer wavelength near-infrared. Interested readers can find further explanation about this in the following reference [122]. Since higher temperatures qualify more vibrational states for such transitions, this theory suggests a much intense peak with larger magnitude of redshift at higher temperatures which is in good agreement with our data.

Another interesting feature observed over the entire wavelength region in general but with substantially larger magnitude around 760 nm is the further increase in magnitude of the absorption with over-treatment. Two key thermally induced biochemical changes known to occur at elevated temperatures are speculated as the possible roots for this increase. First, at elevated temperatures (above 75°C), blood chromophores have been shown to undergo a transition into a modified species known as methemoglobin (metHb)[123], [124], a form of hemoglobin in which the iron exists in the Fe(III) oxidation state incapable of exchanging molecular oxygen in tissue. This conversion is further confirmed *in vivo* by studies performed on subjects with port-wine stain and

telangiectasia [125]. MetHb has a greater absorptivity over the other two blood chromophores (Hb and HbO₂) in the wavelength region of 600-1100 nm (refer Fig. 5.9). The increase in absorptivity as a consequence of this conversion could explain the further increase in absorption coefficient that we observe for all the tissue types when treated at a temperature of 105°C. A further confirmation of this hypothesis is seen in the Fig. 5.8b where the absorption at 770 nm sees an increase when the treated region attains an average temperature of 82°C. Second, the over treatment scenario (target temperature = 105°C) for 10 minutes usually resulted in the formation of a blackish layer (charring) in the treated area for all the tissue types. This carbonization, which has been shown to have an exponential dependence with wavelength on the absorption [126], i.e. larger influence in the visible than than NIR wavelength region (refer Fig. 5.9), could result in the further increase in the absorption. Finally, the *redshifting* of the absorption bands of the hemoglobin (discussed in the previous paragraph) means that the characteristic high absorption bands are now shifted a little more to the right further increasing the value of absorption in this region. Thus the substantially high increase in absorption observed in the region between 650-800 nm can be attributed to a combination of these three factors.

To the best of our knowledge, the formation of peak at 840 nm, a feature consistent among all the tissue types and more evident for the over treatment case, has been reported here for the first time. The origins of the peak remain unclear at this point. The only observable peak at 840 nm is one from the water absorption spectrum [127]. But this peak, even at large temperatures, is of negligible magnitude and hence cannot explain the relatively high value of absorption observed in this study. One other hypothesis for the occurrence of this peak is presented graphically in Fig 5.9. As discussed in the previous paragraph, conversion of Hb to metHb is a well established occurrence at elevated temperature. The spectral features of these two chromophores (see Fig. 5.9) suggest that this conversion, when considered in isolation, implies a net reduction in the absorption below 780 nm (since metHb has a lower absorption compared to Hb. The opposite is however true in the 780-900 nm range where metHb dominates in absorption over the other two chromophores. Finally, beyond 900 nm water becomes the key absorber and as a consequence of dehydration of the tissue with over-treatment, the absorption in this region experiences a drastic reduction. Put together, these variations could, to an extent, justify the occurrence of a peak in this region of the spectrum which is devoid of any major spectral features at room temperature. While this hypothesis needs further confirmation, monitoring the generation and evolution of this peak could give useful information about the conversion of blood chromophores into metHb.

The blue shift and narrowing of the peak at 970 nm which are consistently observed in all the tissues studied could be attributed to the chemical changes that the water content of the tissue undergoes with temperature. Table 5.2 suggests that this shift is roughly 5 nm when the tissue is treated at 105°C and a 4 nm when treated at 70°C. Since the absorption in the spectral region around 970 nm is dominated by water it could be hypothesized that both these effects could be a reflection of some biochemical change in the water with treatment. The broadband absorption of pure water was measured for different temperature in multiple studies [128], [129] and the results sug-

5.3. Optical characterization of thermal treatment using Radio Frequency Ablation (RFA)

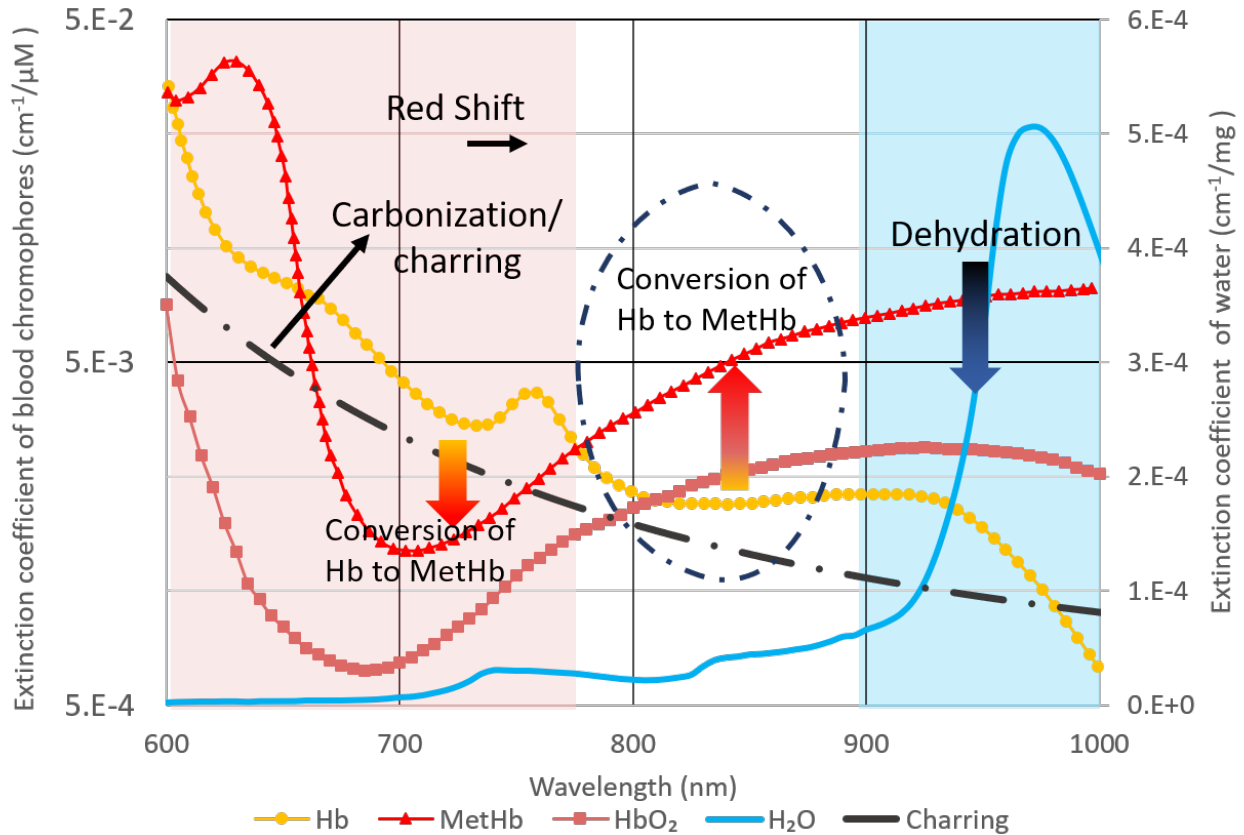


Figure 5.9: Extinction spectra of key absorbers in biological tissue undergoing thermal treatment along with an curve decreasing exponentially with wavelength to represent the influence of charring on the absorption. The plot displays the individual influence of each of the effects discussed above. The absorptivity on either side of the 800-900 nm wavelength region decreases with treatment for the different reasons mentioned. Simultaneously, the absorptivity in this region (800-900 nm) increases with thermal treatment as a consequence of conversion of Hb and HbO₂ into MetHb. Put together these features could manifest in the resultant absorption spectra in the form of a new peak at around 840 nm.

gest a similar blue shift in the absorption peak and band narrowing as is observed in our study. Chung et al.[129] attribute both these features to the weakening of the hydrogen bonding of water molecules with a rise in temperature. They also mention that depending on whether the bonding is between two water molecules or between water and the other macromolecules present in the tissue, the directionality of the shift in this absorption peak could change. The reduction of absorption around the water peak is a rather straight forward consequence of the net reduction of the water content in the tissue (dehydration).

Finally, the reduced scattering spectra experiences a drastic increase in the magnitude from native to ablated or coagulated stage, and this behavior is consistent for all tissue types, Fig. 5.5, (except for brain) and at both temperatures Fig. 5.6(b, d). The *A* and *b* parameters, which are a measure of the density and size of the scattering centers respectively are presented in Table 5.2. A consistent 3 to 4-fold increase in the scatter

Chapter 5. Optical Signatures of Thermal damage in Biological tissue - an exploratory study on *ex-vivo* biological tissue

density is observed in all the tissue types (except brain) for both temperatures. The subsequent decrease in scattering means that the A parameter at 105°C is sometimes lower than that obtained by thermal treatment at 70°C . This drastic increase in the scattering/reduced scattering with thermal treatment is something that has been observed in many *ex-vivo* and *in-vivo* studies that used CW [105]–[108] techniques to monitor the evolution of optical properties in tissue with thermal treatment. The thermal breakdown could lead to a change in the tertiary protein structure which results in increased scattering density [105]. Regarding the size of the scattering centers, a study performed on the rat liver, using a 1064 nm laser to induce thermotherapy *in-vivo*, showed a decrease in the b parameter with thermal coagulation which is in concurrence with our findings for bovine liver tissue at 105°C . In fact, their values for the b parameter - 1.16 for untreated tissue and 0.87 for thermally treated - are in very close agreement with values obtained from our own study (1.39 for untreated and 0.7 for treated) for *ex-vivo* bovine liver. The further decrease observed in the reduced scattering spectrum on over treatment is simultaneous to the further increase in the absorption and is hence, also assumed to be an outcome of the carbonization of the tissue.

Results from Liver and Muscle tissue are, in general, consistent with those obtained from the heart (myocardium) tissue. Thus, all the above-mentioned discussion is well-suited to both these tissue types. The further decrease in the reduced scattering coefficient is more evident in these two tissue types and is possibly a consequence of their tissue microstructure. Brain tissue, on the other hand, shows exceptional features in some cases. Contrary to the other three tissues, the absorption spectrum generally increases upon treatment. Similarly, unlike the other tissues we observe a decrease in reduced scattering with treatment. Apart from these two features all the other observations are in good harmony with the other tissue types. Brain matter has a jelly-like soft consistency and the large folds present in the cortical region of the cerebrum. This structure encounters further complications on exposure to elevated temperatures. Thus, though non-invasive optical measurements are routinely performed on the brain, the thermo-chemistry of this tissue must be understood to better interpret these results.

The fact that non cancerous bovine tissue was used for this study *ex-vivo* demands certain caution. Studies [130] performed on the optical properties *in-vivo* and *ex-vivo* on mouse ear models and found that in the *ex-vivo* case the optical properties decrease over time due to loss of blood. However, since most of our measurement were performed under 15 minutes the effect of this decrease can be assumed to be minimal. Also, all the observations in this study were performed as a comparison between the thermally treated tissue and the native tissue, thus the factors like influence of the radio frequency needle on the retrieved optical property can be neglected. Simultaneous histological assessment and use of thermal damage models [131] of the tissue could help in better understanding the extent of thermal damage in the tissue and its correlation with the recovered optical properties. Future studies are aimed at confirm the findings on live animal models, both healthy and diseased, before employing it intraoperatively in clinics.

5.4 Conclusions

Systematic variations in the optical properties of tissue undergoing thermal treatment could be of great interest in closely monitoring the dosage and localization of the treatment in real time. The study presented in this chapter can be broadly categorised into two sections. First, a broadband characterization of nine different porcine organs and tissue types. This permitted us to test the feasibility of using our instrumentation and technique for the purpose of monitoring thermal damage in tissue. Also this study provides the community with a library of optical properties of biological tissues which can be utilized for different purposes (e.g. design of biological phantoms, simulation of complex heterogeneous structures etc.)

Secondly, a subset of these tissue types, obtained from a different type of animal (bovine) were then chosen to study the effect of thermal damage on the optical properties of the tissue. This work demonstrates certain unique and consistent changes in the broadband absorption and reduced scattering coefficient spectra of different biological tissue *ex-vivo* undergoing RF based thermal treatment. The possible physical and biochemical nature of their origins of these variations is also discussed briefly. To our knowledge, this work demonstrates for the first time, the use of broadband time domain (TD) diffuse optical spectroscopy for this purpose.

The ability of the TD technique to continuously monitor the RF procedure, even if at few wavelengths, indicates that this technique could provide valuable *real-time* feedback on the efficiency and efficacy of the thermal treatment. The monitoring procedure could be carried on even after the termination of the thermal treatment to track changes in the optical properties of the tissue post ablation. Thanks to the portable nature of our TD-DOS instrument, a similar type of monitoring could be achieved with other modalities of thermal treatment such as microwave, laser induced and high-frequency focused ultrasound ablation.

Further understanding of the observed effects and their exact correlations with the extent of thermal damage and ablation margins, specifically in malignant tissue *in-vivo* is required. Nevertheless, this study provides a wealth of information in the form of optical properties which could be used to design reliable markers or metrics that predict the extent of tissue ablation. The key wavelengths identified can be used to develop single wavelength monitoring systems which can be incorporated into the RFA device. Other future directions could be 1) using spatially resolved optical imaging methods, such as photoacoustics alongside to assist in differentiating ablated and non-ablated regions or 2) up-scaling the point spectral measurement to Diffuse Optical Spectroscopy Imaging using multiple fibers to obtain ablation maps.

CHAPTER 6

Multi-laboratory Efforts towards Performance Assessment in Diffuse Optics - The BitMap Exercise

6.1 Introduction

The field of Diffuse Optics or Near Infrared Spectroscopy has seen a tremendous growth in development of devices for different biomedical purposes. The large variety of diffuse optics instruments can be classified on the basis of different criteria. As discussed in Chapter 1, with the same underlying principle different modalities of instrumentation have been realized depending on the type of source used, e.g. Continuous Wave; CW, Frequency Domain; FD, Time Domain; TD and Spatial Frequency Domain; SFDI. The number of channels used in the instrument, (single channel, multi-channel and tomographic) provide another way of classifying the instruments. Yet another way to distinguish instruments is on the basis of application. Spectroscopy (for the characterization of chromophores or constituents), Oximetry (for the monitoring of functional characteristics), Imagers (to provide tomographic/topographic maps of the tissue under investigation) and Flow measurement (quantification of blood flow) are some of the commonly catered applications especially from a clinical point of view. Optical mammography applied to detect and characterize breast lesions and monitor neoadjuvant chemotherapy is an excellent example in this regard. Likewise, Technology readiness level (TRL) [132] of the instrument (an estimate of the maturity of a particular technique or instrument) provides a further classification for the different instrumentation developed. This wide variety in Diffuse Optics instrumentation calls for a similar breadth in the analysis techniques. A comprehensive list of these analysis techniques can be found in Sec. 1.5 of this thesis. With such a diversity and exponential growth

it is no exaggeration to state that diffuse optics has a considerable impact on the future and evolution of the field of biophotonics.

While such a growth, especially in a field with direct and evident clinical impact is commendable, it comes with its own set of challenges. One such challenge facing these techniques is the lack of standardization and imposition of quality testing tools. Individual systems often demonstrate excellent repeatability in deriving necessary parameters, however there is a dire need to compare the results among instruments, laboratories and clinics. While protocols devised specifically for this purpose do exist [52], [133], [134], multi-laboratory studies employing these protocols to enhance the performance assessment of the instrument are few and far between [135], [136].

With the aim to enforce such a culture of performance assessment within the field, a multi-laboratory exercise was initiated as a part of the BitMap Project. BitMap is an EU level Marie-Curie consortium (Brain injury and trauma monitoring using advanced photonics, H2020 MSCA-ITN-ETN, Project No. 675332) [137] which aims to develop, utilize and validate advanced photonic devices and analysis methods for non-invasive, online monitoring of the cerebral hemodynamics for neuro-intensive care. The consortium is comprised of 15 early stage researchers and their corresponding doctoral supervisors. Also, it is a healthy mix of physicists, clinicians and industry and research experts making it ideally suited for such an expedition. A total of 29 instruments were enrolled for this study mainly from the partner institutions of the BitMap consortium and a two other external institutions. Instruments of all modalities (CW, TD, FD and SFDI, (refer Sec 1.2) and different application (Mammography, spectroscopy, oximetry etc.) were enrolled. The number of institutions and instruments involved makes this study the largest such multi-laboratory comparison of diffuse optics instrumentation so far. The vast resulting data set is intended to be shared on an open data platform which would further enhance the usefulness of this study. Such a data-set could then be used to test the validity and limitations of different analysis techniques and also be used to enhance machine learning algorithms aimed at data analysis.

The BitMap exercise, as it will be referred to from here on wards, will be comprised of three actions 1) multi-laboratory measurements 2) open-data deployment and 3) employing algorithms and common analysis techniques on the data-set. At the moment, the first action is nearing completion while the second and third actions have just been initiated. This Chapter mainly describes some of the key results of the first action. A brief discussion of the three actions will be followed by description of the protocols, phantoms and instruments employed for the exercise. The chapter concludes with some of the key results from Action 1.

6.2 Protocols, Phantoms and Implementation

6.2.1 Actions

1. Action 1 – Phantom Exercise

A consistent set of phantoms has been circulated sequentially within all the enrolled institutions to apply the tests specified in 3 internationally agreed Protocols, as described below. Care was taken to ensure measurement quality and documentation. The author of this dissertation travelled with the phantoms to most of these institutions to ensure consistency and easy application of the tests. A first level

analysis was provided by each Institution and created a first base for performance comparison. As a general rule, we opted to test all the instruments under their usual operating conditions. For this action, *the instrument along with the analysis technique that is usually employed for its measurements was considered as a single unit.*

2. Action 2 – Open Data

Once complete, the data-set will be deployed in an Open Data repository with the aim to provide a thorough documentation of this large-scale exercise and offer the opportunity to reuse it. To this end, a standardized data format was envisaged, metadata to archive relevant information on the systems was collected, and the design of a unified reporting sheet is in progress. A collaborating researcher from CEA (Grenoble, France), has initiated this action with the data available so far.

3. Action 3 – Cross-Analysis

While in the first stage each laboratory provided analysis for their own data, in a second phase the whole database can be further cross-analysed using different algorithms and programs. This helps to understand the role of the systems' parameters on final derived quantities, and conversely the differences provided by diverse analysis tools available across the community and indeed internationally. The partner institution from Birmingham will coordinate this activity. The standardization of data format and the availability of metadata from Action2 will allow for smoother data interoperability and improve the efficiency of this action.

6.2.2 Protocols and Phantoms:

- **Protocols:** Three Protocols for performance assessment of Diffuse Optics devices agreed at EU level in the framework of previous EU projects were adopted. These are the BIP Protocol (characterization of *basic instrument performances*) [134], the MEDPHOT Protocol [52] (homogeneous optical properties of turbid media), and the NEUROPT Protocol (detection of inhomogeneity) [133]. Each of these Protocols is further divided into individual tests as described in Table 6.1 summarizes the key tests and measurable of the different protocols employed for the exercise. The optical properties considered for the assessment of the instruments were limited to the optical properties (absorption, reduced scattering coefficients) and the intrinsic contrast of the sample under measurement.
- **Phantoms:** Three sets of phantoms were chosen among those proposed in previous multi-laboratory studies to apply the tests foreseen in the protocols. In particular, we opted for solid phantoms to facilitate reproducibility of results and easy application of the tests. The phantoms were circulated sequentially to all laboratories following a round-robin scheme. In detail, we selected a Responsivity phantom [134] for the specific test of the BIP protocol, a kit of 32 homogeneous solid phantoms spanning a wide range of absorption and scattering properties [52] for the MEDPHOT Protocol and a solid switchable phantom [138] for the nEU-ROPt Protocol (see Fig. 6.1).

Chapter 6. Multi-laboratory Efforts towards Performance Assessment in Diffuse Optics - The BitMap Exercise

Protocol	Tests	Phantoms	Measurable	Characterizes
MEDPHOT[2]	Accuracy, Linearity, Uncertainty, Stability, Reproducibility	Matrix of 32 homogeneous solid phantoms	Absolute absorption (μ_a) and reduced scattering (μ'_s) coefficients	Ability to accurately retrieve absolute optical properties
BIP[3]	General performance, Responsivity, DNL	Responsivity solid phantom	IRF, Background, DNL, Responsivity	Basic instrument performance
nEUROPt[4]	Depth selectivity, lateral resolution	Switchable solid phantom	Contrast, Contrast to Noise Ratio	Ability to detect an inhomogeneity

Table 6.1: Summary of the Protocols and Phantoms used for the BitMap Exercise

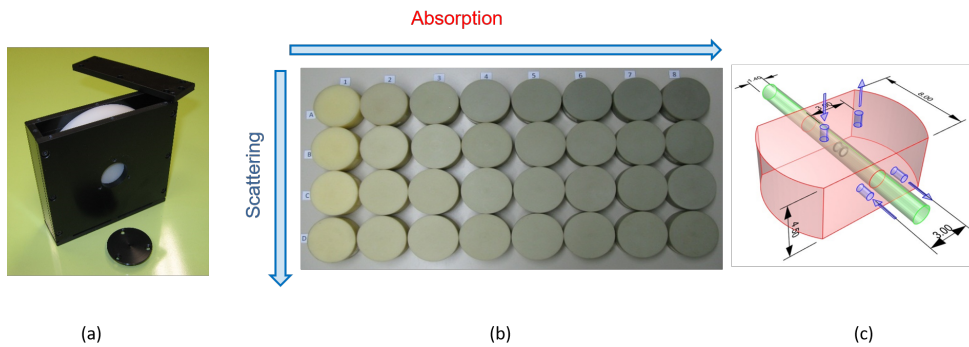


Figure 6.1: The (a) Responsivity phantom (b) MEDPHOT kit and (c) the solid switchable phantom

6.2.3 Institutions and Instruments:

The 29 instruments enrolled for the BitMap Exercise are listed in Table 6.2 along with the parent institution and some basic information on the modality and application. To give the reader an unbiased picture of the study a unique enrollment ID (see Table 6.2) for each instrument will be used to represent the instrument from this point on. It is important to note that not all the tests mentioned above are applicable to all the instrumentation presented in this table. For instance, the CW instruments (ID #4, #9 and #20) cannot be assessed using the MEDPHOT and BIP protocols which are meant for TD (and to an extent FD) instrumentation. In other cases, the mechanical design or the other similar obstacles restrict the application of certain tests or protocols to certain instruments e.g. ID #21 and #27 are designed to work in transmittance alone and hence the nEUROPt protocol which needs to be performed in reflectance cannot be applied to this instrument. Similarly, the design of instrument #7 precludes the power measurement of the source (at a particular wavelength) thus making the instrument invalid for the Responsivity measurement of the BIP protocol (will be discussed further in the relevant subsections).

Irrespective of these limitations the cohort of instruments is still assumed to be large enough to provide a valuable data-set for the other two actions. Table 6.3 is indicative of the breadth of the exercise in terms of range of modalities used but more importantly with respect to the applications. Another important dimension in which the instruments enrolled show good variability is the (technology readiness level) TRL [132]. A

6.2. Protocols, Phantoms and Implementation

Table 6.2: List of instruments enrolled for this exercise

Instrument name	Institute Short	ID	Modality	Application
Spectra Compact(broadband)	POLIMI ^a	1	TD	Spectroscopy
3mm SiPM	POLIMI ^a	2	TD	Oximetry
TD HPM based spectrometer	PTB ^b	3	TD	Spectroscopy
NIRO 200NX	UHB/UoB ^c	4	CW	Oximetry
ISS OXIPLEX-TS	UHB/UoB ^c	5	FD	Oximetry
TD Multiwavelength system	IBIB ^d	7	TD	Spectroscopy
TD-DCS system	IBIB ^d	8	TD	Blood Flow
SRS-CW system	UCL ^e	9	CW	Spectroscopy
TRS-DCS FLOWer	ICFO ^f	10	TD	Oximetry
TD MCP based system	PTB ^b	11	TD	Spectroscopy
clinical TD oximeter	IBIB ^d	13	TD	Oximetry
TD 8 channel system	IBIB ^d	14	TD	Oximetry
TD MAESTROS	UCL ^e	15	TD	Oximetry
LUCA	POLIMI ^a	16	TD	Spectroscopy
Oximin	POLIMI ^a	17	TD	Oximetry
Clinical Oximeter	POLIMI ^a	18	TD	Oximetry
Wearable TD device	POLIMI ^a	19	TD	Oximetry
OctaMon	POLIMI ^a	20	CW	Oximetry
Mammot	POLIMI ^a	21	TD	Mammography
"Fruit" spectrometer	POLIMI ^a	22	TD	Spectroscopy
OCTOPUS	POLIMI ^a	23	TD	Imaging
ClinicalDCS - BabyLux	POLIMI ^a	24	TD	Oximetry
Spectra Lab(broadband)	POLIMI ^a	25	TD	Spectroscopy
Lab TD-DCS	POLIMI ^a	26	TD	Blood Flow
Mammot v2	POLIMI ^a	27	TD	Mammography
BenchtopDOS	UoS ^g	28	SFDI	Spectroscopy
MultispectralSFDI	UoS ^g	29	TD	Imaging
NIROT Imager*	UoZ ^h	30	TD	Imaging
ISS Imagent*	UoZ ^h	31	FD	Imaging

a - Politecnico di Milano, b - Physikalisch-Technische Bundesanstalt, Berlin, c - University Hospitals Birmingham, Birmingham/ University of Birmingham, Birmingham, d - Nalecz Institute of Biocybernetics and Biomedical Engineering, Warsaw, e - University College London, London, f - The Institute of Photonic Sciences, Barcelona, g - ICube Laboratory, University of Strasbourg, Strasbourg, h - Biomedical Optics Research Laboratory, University Hospital Zurich, Zurich.

HPM - Hybrid PhotoMultiplier, MCP - MicroChannel Plate, TD - Time Domain, CW - Continuous Wave, FD - Frequency Domain, SFDI - Spatial Frequency Domain Imaging, SRS - Spatial Resolved Spectroscopy, DCS - Diffuse Correlation Spectroscopy.

* - Measurements and Analysis in Progress

Please note that the ID number 6 and 12 correspond to instruments that could not participate in the exercise successfully.

The instruments developed as a part of this thesis correspond to ID number 1 and 25.

numeric scale from 1 to 9 decides the maturity of the technology, TRL1 corresponding to basic principles observed and TRL9 to the deployment of the instrument in an operational environment. System #2, for e.g. is a state-of-the-art technology involving a large area SiPM detector and hence is low on the (TRL) scale. On the other hand other instruments like the one described in this thesis (#25) has been enrolled in some pre-clinical studies and has undergone ethical approval thereby giving it a relatively higher TRL value. Finally, the ISS and NIRO (#4, #5 and #31) instruments are commercially manufactured instruments and are routinely used in a bed-side clinical

environment thus exhibiting the highest possible TRL.

Application	Modality				Total
	CW	TD	FD	SFDI	
Spectroscopy	1	9	1	0	11
Imaging	0	4	0	1	5
Oximetry	2	8	1	0	11
Blood Flow	0	2	0	0	2
Total	3	23	2	1	29

Table 6.3: Instruments categorized based on applications and modalities

6.3 Preliminary Results from Action 1

Some of the results of Action 1 are presented here. The reader is once again reminded that not all tests are applicable to every system. Results are grouped according to the relevant tests mentioned in Table 6.1.

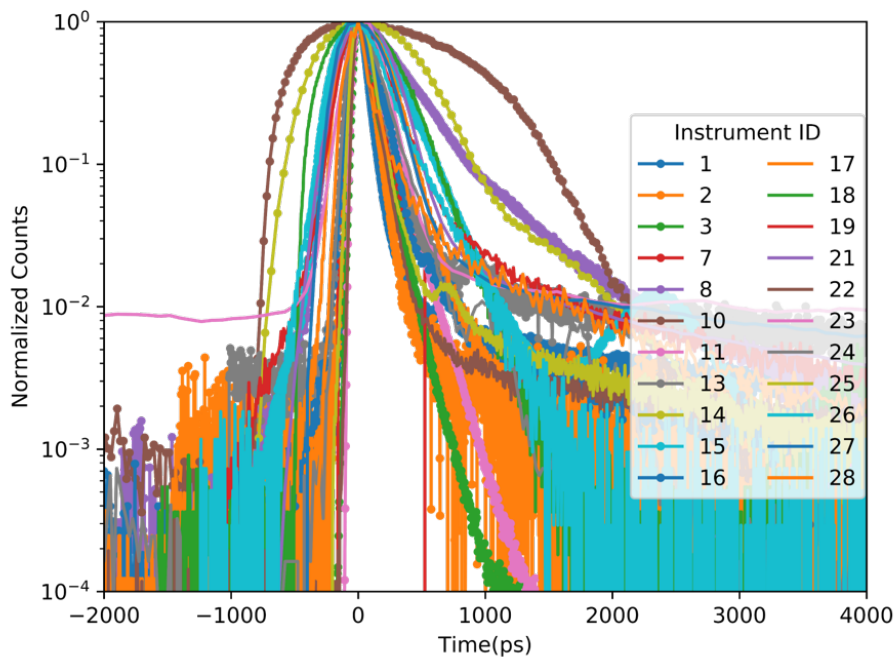


Figure 6.2: Comparison of the Instrument Response Functions of the different TD instrumentation after background subtraction and peak normalization.

6.3.1 Basic Instrument Performance:

As mentioned, this protocol concerns primarily the TD instrumentation and more specifically deals with recording the basic characteristics of the instruments which influence the quality and accuracy of measurements in clinical applications. Parameters like the average output power of the pulsed laser source, repetition rate, central wavelength and

width are some of the relevant entities with respect to the source which were recorded. With respect to the detection stage three parameters were considered

1. the IRF, its background, and its stability in time
2. the responsivity of the detection system
3. the differential nonlinearity (DNL) of the timing electronics.

IRF:

Characterizing the IRF is crucial to understand the time-resolution of the instrument as a whole. The IRF is usually measured by inserting a reference sample in between the source and detector (fibers), like a millimeter thin layer of teflon, that has negligible contribution to the temporal dispersion. The IRFs of all the time domain instruments enrolled in the exercise is presented in Fig. 6.2. Data presented is background subtracted and peak normalized.

The IRF is characterized by three important features:

- its full width at half maximum FWHM (ps)
- background (dynamic range)
- shape of the trailing edge.

From the figure it is evident that all the instruments have a dynamic range of at-least 2 orders of magnitude beyond which there is a tangible influence of the noise. However, some of the instruments (#3 and #11, green and salmon pink circles) display a higher dynamic range close to 4 orders of magnitude. Similarly, there is a wide variation in the FWHM of the different instruments from less than a 100ps to a 900ps (as can will be shown in Fig. 6.3). Also while some detectors have a fast decaying trailing edge others (based on SiPM) show a very slowly decaying tail. The trailing edge in certain cases also displays distinct shoulders and after peaks. All these variations can be explained by considering the pulse shape of the laser, temporal response of detector and electronics and finally additional dispersion from the fiber-optics. For e.g. The use of picosecond pulsed lasers operated at the maximum power settings, and huge dispersion effects from high dispersion fiber bundles could eventually result in relatively large values of FWHM (such as #10, brown circles). On the other hand use of MCP-PMT or hybrid PMT detectors, in conjunction with supercontinuum lasers such as #3 and #11 results in narrow IRFs with higher dynamic ranges. At this juncture, it is necessary to remind ourselves that the need for a narrow IRF is more critical in the case of devices dedicated to spectroscopy and related application where they might encounter larger absorption values than, say, oximeters which are in for most part of their operation restricted to a specific range of absorption values.

Fig. 6.2 indicates that the density of the data involved in the single figure hampers the ability to clearly understand the result from individual systems and makes a comparison of the results from different instruments quite challenging. To overcome this issue and facilitate an easier discussion of the results, all the tests are displayed with the help of some indicative *Figure of Merit* (FOM) plots with an example figure from one instrument to describe the test.

Responsivity

The responsivity of the detection system in diffuse optics is a measure of the efficiency of detecting low light levels emerging from tissue. In general, the responsivity of a detector is the ratio between the measured signal and the magnitude of the input illumination. In the present context, it is defined as the ratio of the photon count rate (or if the measurement is not relying on photon counting, another measure of signal magnitude) and the amount of light emitted by the tissue directly beneath the detector optode. This measurement is performed with a specific “responsivity phantom” with known diffuse transmittance factor that acts as an approximately uniform light source with Lambertian angular characteristic [2]. A transmittance measurement is performed on this “responsivity phantom” and the number of photons collected at the detector over a particular time are noted. The power input to the phantom at this specific configuration is also noted. Then substituting these values in the following formula gives the responsivity of the detector.

$$s_{\text{det}}^L(\lambda) = N_{\text{tot}} / [t_{\text{meas}} \kappa_p(\lambda) P_{\text{in}}(\lambda)] \quad (6.1)$$

where $\kappa_p(\lambda)$ is the phantom-specific photon transmittance factor, $P_{\text{in}}(\lambda)$ is the input power at the specific wavelength and in (W), N_{tot} is the total counts measured (after background subtraction) over a measurement time t_{meas} . The unit of s_{det}^L is m^2sr

The responsivity of some of the TD instrumentation is plotted in Fig. 6.3 against their corresponding FWHM (both values considered at 830nm). The instrument ID is annotated next to the data point while the application is distinguished by the marker shape in the legend. The spread suggests no evident coupling between these two parameters. One observation here is the relatively large responsivity of instruments #2 [139], #21 and #27[140]. These correspond to the large area SiPM detector and the two variations of an optical mammograph (Mammoth). All these devices work with the detector directly in contact with the sample (in this case the responsivity phantom). This explains the larger responsivity since photon harvesting capabilities of instrument have been shown to increase while working with the detector in contact. Secondly, most of the spectroscopy systems (hexagons) are located in the left-most part of the chart corresponding to shorter FWHM. This further substantiates the fact that the choice of the IRF is very much dependent on the target application of the particular instrument.

6.3.2 MEDPHOT (Absolute Optical Properties)

The MEDPHOT protocol has been discussed in detail in Chapter 2. All the tests from this protocol are dependent on the instruments capabilities to retrieve the absolute optical properties irrespective of the modality. Moreover, one of them, *the uncertainty test*, is particularly applicable to only TD instrumentation. For this reason, only the instrumentation based on TD, FD and SFDI are eligible for this protocol. In principle, CW instruments, in specific configurations, can qualify for some of these tests. However, none of the CW instrumentation enrolled for this exercise in their current manifestations satisfy this criteria.

Some general considerations for all the measurements performed as a part of the MEDPHOT protocol are.

- The standard acquisition time of measurements was 1s.

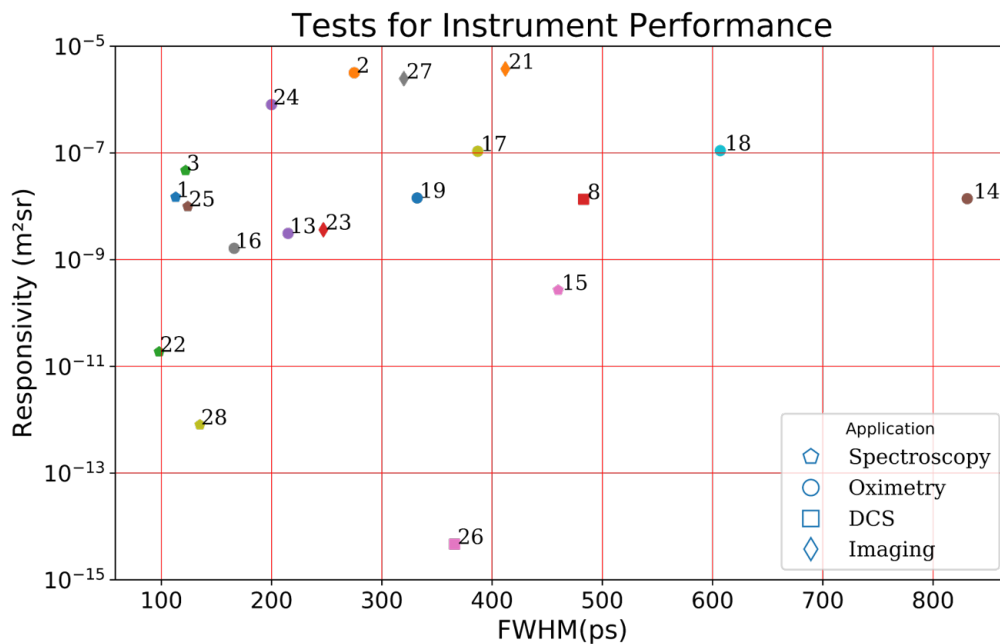


Figure 6.3: Figure of Merit (FOM) plot comparing the responsivity and FWHM of some of the TD instruments around 830nm.

- Every measurement was repeated 20 times, The results presented are the average of the 20 measurements and the standard deviation over the 20 measurement is plotted as error bars (wherever applicable).
- Apart from the Accuracy and Linearity measurements (which were performed over the entire MEDPHOT kit) all the other tests were performed on the B2 Phantom of the MEDPHOT kit.
- The expected count rate from the TD instrumentation was 500kcounts/s. But this particular condition was more suggestive than restrictive (if the standard operating conditions of the instruments demand a different count rate then that was used).

A significant part of Action 1 of this exercise involved the design of indicators that condense the result of each of the tests in the protocols in a manner that summarizes the result of the test for the specific instrument and allows for a comparison with the results from the other instruments. Such indicators, referred to as *synthetic indicators* or *synthetic descriptors* will be used henceforth to create the *figure of merit* plots.

Accuracy The accuracy test addresses the capability of the system to retrieve the absolute estimate of the absorption and reduced scattering coefficient of a reference medium or phantom. The absorption and reduced scattering coefficients obtained from all the instruments when measured on phantom B3 of the MEDPHOT kit are plotted against the wavelength at which they were measured in Fig. 6.4 (a,b). Fig. 6.4(c) shows the in optical properties provided by different instruments at 830nm (data for instruments not operational at this wavelength is provided at the wavelength closest to 830nm). Overall,

Chapter 6. Multi-laboratory Efforts towards Performance Assessment in Diffuse Optics - The BitMap Exercise

the mean discrepancy of instruments operating at 830 nm is 16% and 19% of the average value for absorption and reduced scattering, respectively. It is interesting to note here that the data point with the maximum deviation from the rest (#5) corresponds to the only frequency domain instrument in the cohort.

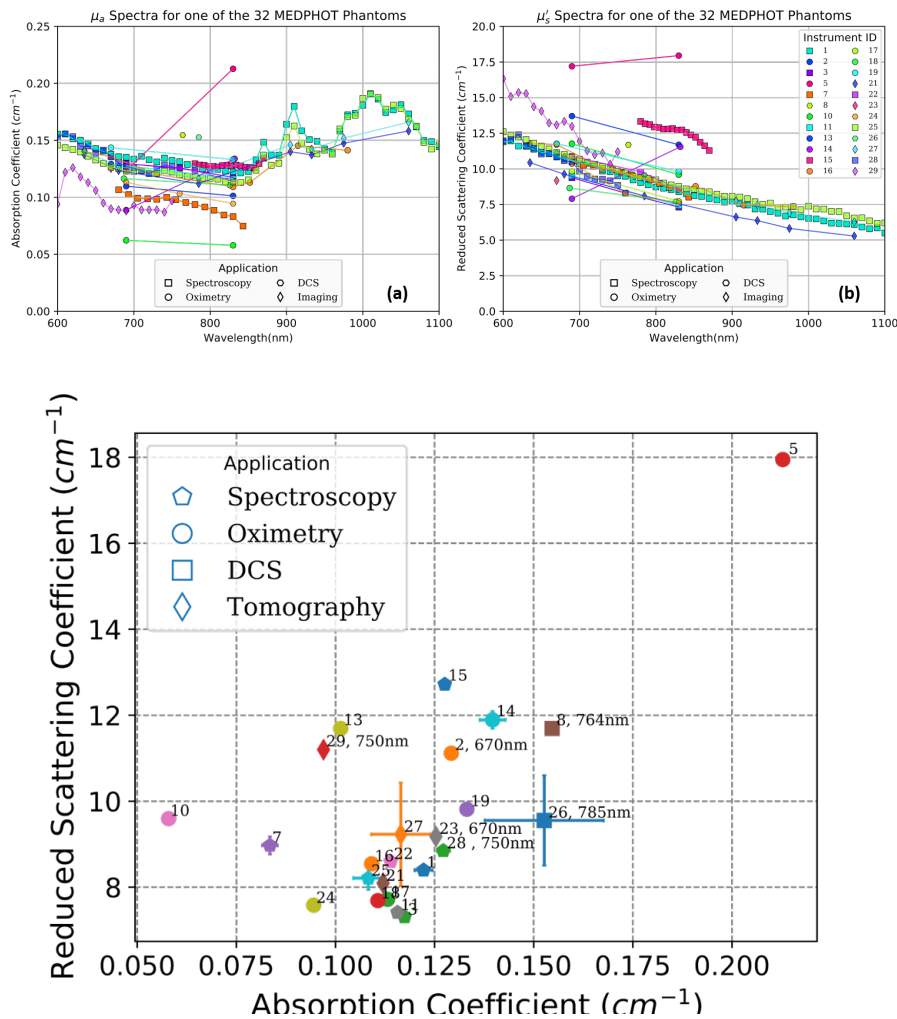


Figure 6.4: (Above) the absorption and reduced scattering spectra of all the TD instruments measured on the Phantom B3 of the MEDPHOT series. (Below) Absorption vs Reduced scattering at 830nm (wavelength mentioned in cases where it is not 830nm). Results represent the average over the 20 repetitions with the standard deviation plotted as error bars.

Linearity and Coupling

Measurements are performed on a set of phantoms with one optical property fixed while the other is expected to increase linearly with each phantom. Plotting the results of this exercise as shown in Fig. 6.5 provides insight into the influence of one optical property on the retrieval of the other. Thus using the 4 scattering series and the 8 absorption series. The key information is the linearity of the system in retrieval of the absorption and scattering coefficients, as well as the artefacts (cross-talk) caused by the absorption or scattering coefficient on the estimate of the other parameter.

6.3. Preliminary Results from Action 1

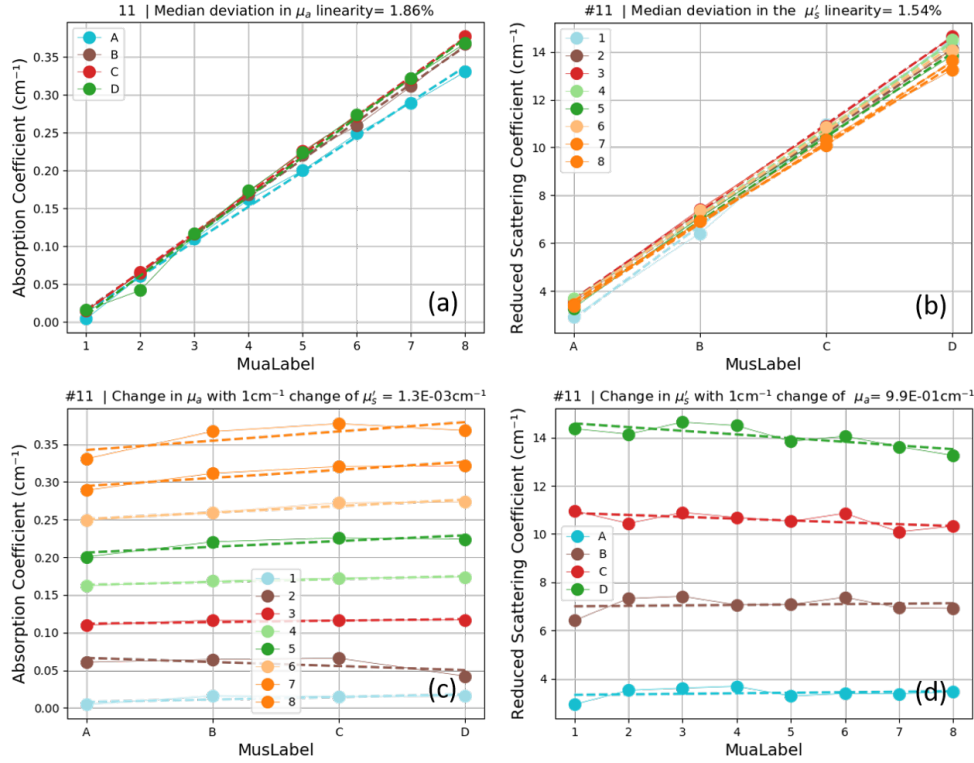


Figure 6.5: An exemplary plot of the linearity and coupling between the optical properties. (a) and (b) show the linear increase in the absorption and reduced scattering coefficients for each series corresponding to their corresponding labels (x-axis). (c) and (d) show the influence of one optical property on the other. The title of each subplot gives the instrument ID and also describes the synthetic indicator of the linearity or coupling observed which will be used for the figure of merit plots (see description in the relevant subsection).

The synthetic indicators in the titles of each of the subplots in Fig. 6.5 are used to create the FOM plots for the linearity and coupling test of the MEDPHOT protocol. These synthetic indicators are obtained in the following fashion. For the linearity plots i.e. Fig. 6.5 (a,b) The median value of the relative deviation of the data-points and the linear fit (dashed line) over the different series is considered to represent the median deviation from linearity for the specific optical property. For the coupling plots Fig. 6.5 (bottom) The median value of the absolute slopes of the linear fit (dashed line) over the different series is considered to represent the coupling between the two optical properties. To better understand this, we invoke the result from Fig. 6.5(c). Any factor resulting in an increment of 1 cm^{-1} in the reduced scattering coefficient would correspondingly deviate from the true value of the absorption coefficient by $1.3 \times 10^{-3} \text{ cm}^{-1}$.

Per these definitions, an ideal instrument would have both these values as close to 0 as possible (suggesting perfect linearity in assessing the linearly increasing optical property and zero influence of one parameter on the retrieval of the other). With this background we plot the resultant figure of merit plots for the linearity and coupling below.

Fig. 6.6 presents the resultant FOM plots for the linearity and coupling tests. Fig

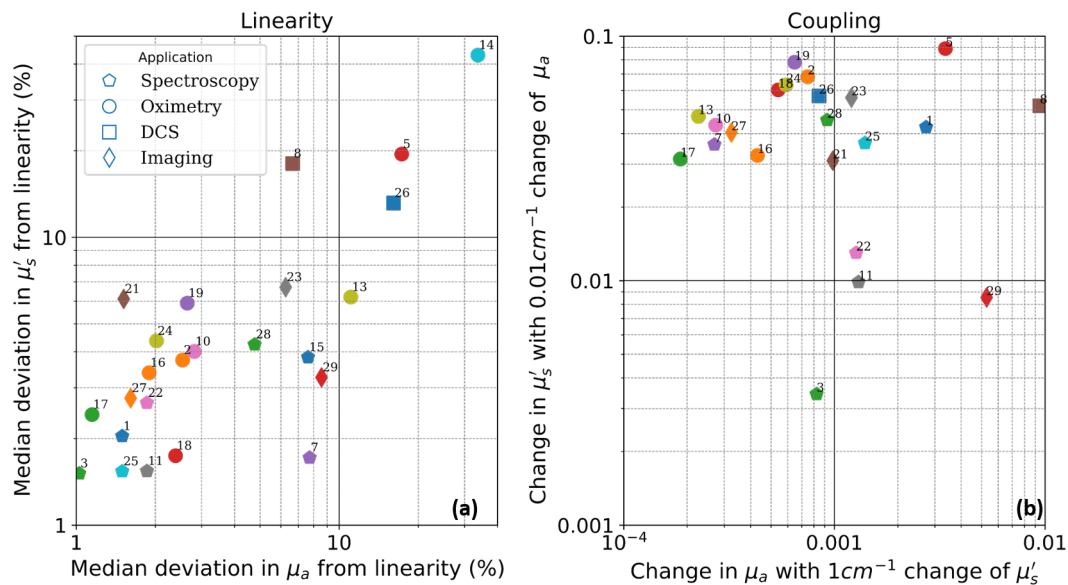


Figure 6.6: Figure of Merit plots for the (a)Linearity and (b)Coupling tests of the MEDPHOT protocol. The x and y axes in both cases are plotted on log scales.

6.6(a) plots the linearity synthetic indicators of the two optical properties against each other (absorption on the x-axis and reduced scattering on the y-axis) while (b) plots them for the coupling. In the plot for Linearity, 20 out of the 24 instruments enrolled exhibit a median deviation from linearity in both optical properties of under 10%. The instruments designed for DCS (blood flow) related studies (#8, #26) and the frequency domain instrument (#5) show a little larger deviation in linearity. Again, most of the spectrometers (hexagons) are seen to have a deviation of under 3% in the linearity of reduced scattering (μ'_s) and under 2% in the linearity of absorption.

Similarly, the FOM plots for the coupling, Fig 6.6(b), show that with an increment of 0.01 cm^{-1} in μ_a the deviation of μ'_s for most of the instruments is between 0.01 and 0.1 cm^{-1} . Considering an average reduced scattering value of 10 scm^{-1} for biological tissue, this corresponds to 0.1 - 1% variation which is reasonable. Similarly, the deviation in absorption for a 1 cm^{-1} increment in μ'_s is within 0.01 cm^{-1} for more than 50% of the enlisted instruments.

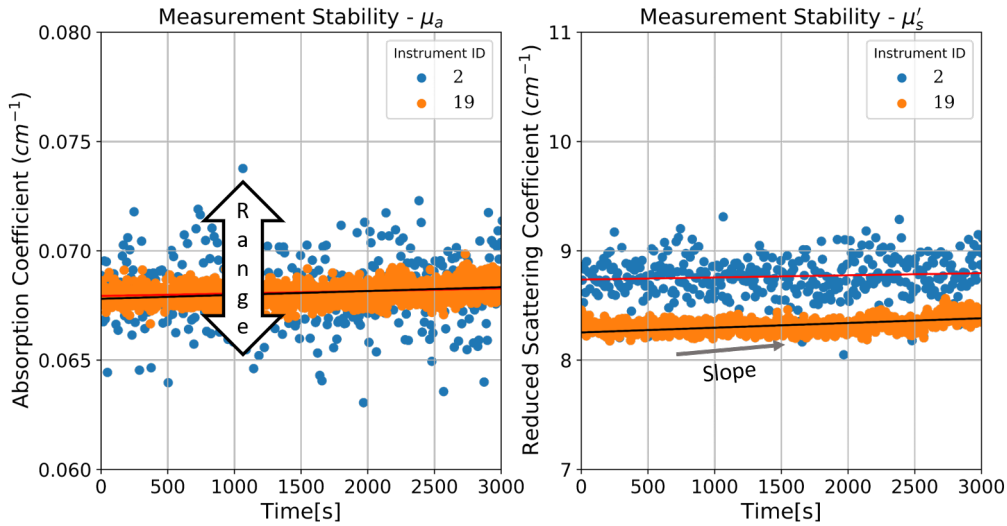
Stability:

Figure 6.7: : Example of the stability plot for instruments 2 and 19 (on the B2 Phantom). the possible synthetic indicators (range and slope) are indicated.

Fig. 6.7 displays some exemplary plots of the temporal stability in the retrieval of the optical properties over a period of more than 1 hour. Both the absorption and reduced scattering coefficients are stable within a range of $\pm 10\%$ for #2 while under 4% for #19. In this case, the *range of variation* over the entire measurement period and the drift given by the *slope of the temporal evolution* plots were considered as the synthetic indicators.

Fig 6.8 plots the above mentioned synthetic indicators for both optical properties for all instruments. Most of the instruments lie in the region with a range of under 10% for both optical properties. Slope/deviation from the mean value of under 0.001% per minute. This means that using any of these instruments for a continuous monitoring of the optical properties in a clinical environment, one can expect a maximum deviation of 0.001% in μ_a in one minute (or 0.1% in 100 minutes or $1^3/4$ hours).

Noise/Uncertainty:

A test of the power/count rate dependence on the precision of the measured optical properties is performed by measuring the DTOFs at different count rates and comparing their performance in retrieving the optical properties. 20 acquisition, with 1 second acquisition time, were taken at different count rates and the coefficient of variation, CV (defined as the ratio of the standard deviation of repetitive measurements over the mean value for the absorption) of the retrieved optical properties at each count rate are plotted against the counts as shown in Fig. 6.9. As a general practice, a CV=1% can be considered as a reasonable target for precision on diffuse optics measurements. The Noise/Uncertainty plot identifies the minimum number of counts or input energy required to reach such a goal (the red and the green lines and circles for each plot). This is further dependent on the maximum count rate of the system or the maximum input

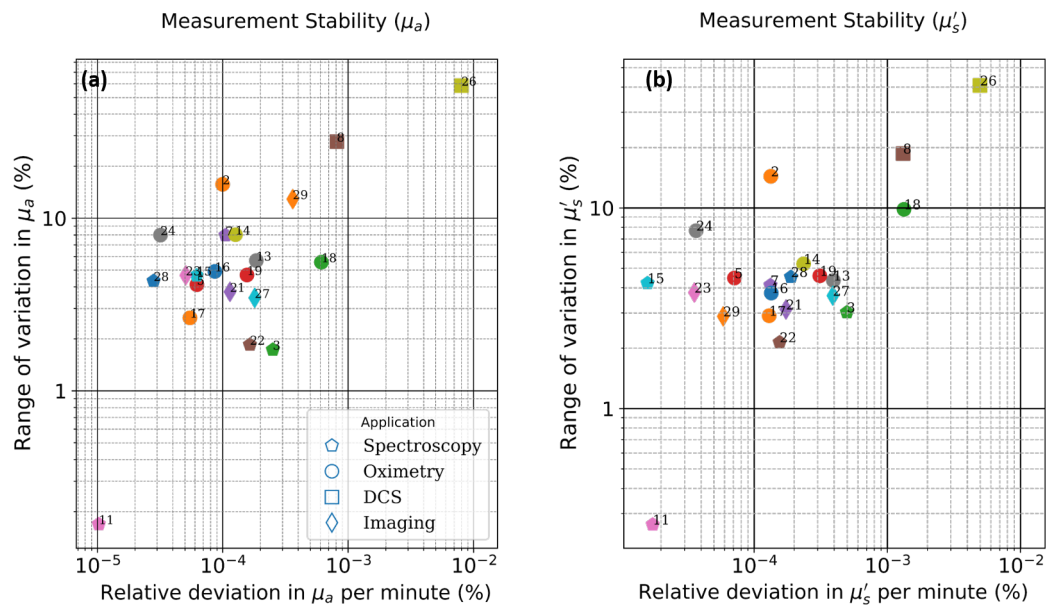
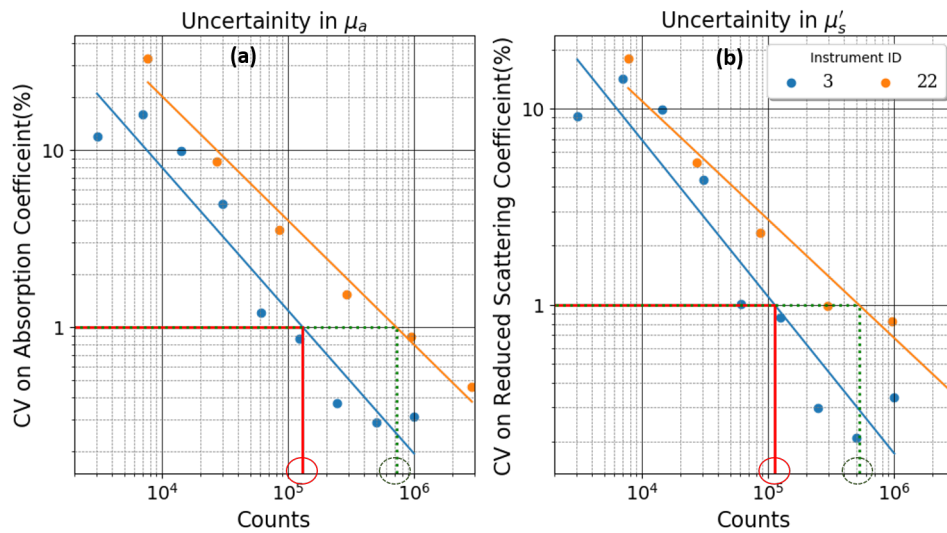


Figure 6.8: Figure of Merit plots for the Stability test for both the optical properties. The range of variation is plotted against the slope that corresponds to the deviation over time for both the optical properties.

power and correspondingly affects the acquisition time.

The synthetic indicators chosen for the Noise test are the number of counts necessary to reach a CV of 1% in both the optical properties. Fig. 6.10 plots the counts necessary to achieve 1% CV in μ'_s against counts necessary to achieve 1% CV in μ_a . The requirement for a good CV in most cases is in between a 100 kcounts and 1 million counts and in most cases it is closer to the former. Also, all the results are not far from the diagonal line in the plot suggesting the count rate necessary to achieve 1% CV in both optical properties is nearly the same. An interesting observation in this regard is that instrument #7 that relies on the method of moments for fitting [141], [142] requires a substantially lower number of counts to achieve a minimal variation in the results compared to the rest of the instrumentation. Thus it would be interesting to understand how the usage of this method of analysis (which is different from the traditional analytical solution based on the DE employed by a majority of the other instruments enlisted) fares with the other instruments. These kind of initiatives will be undertaken in the Action 3 mentioned above.



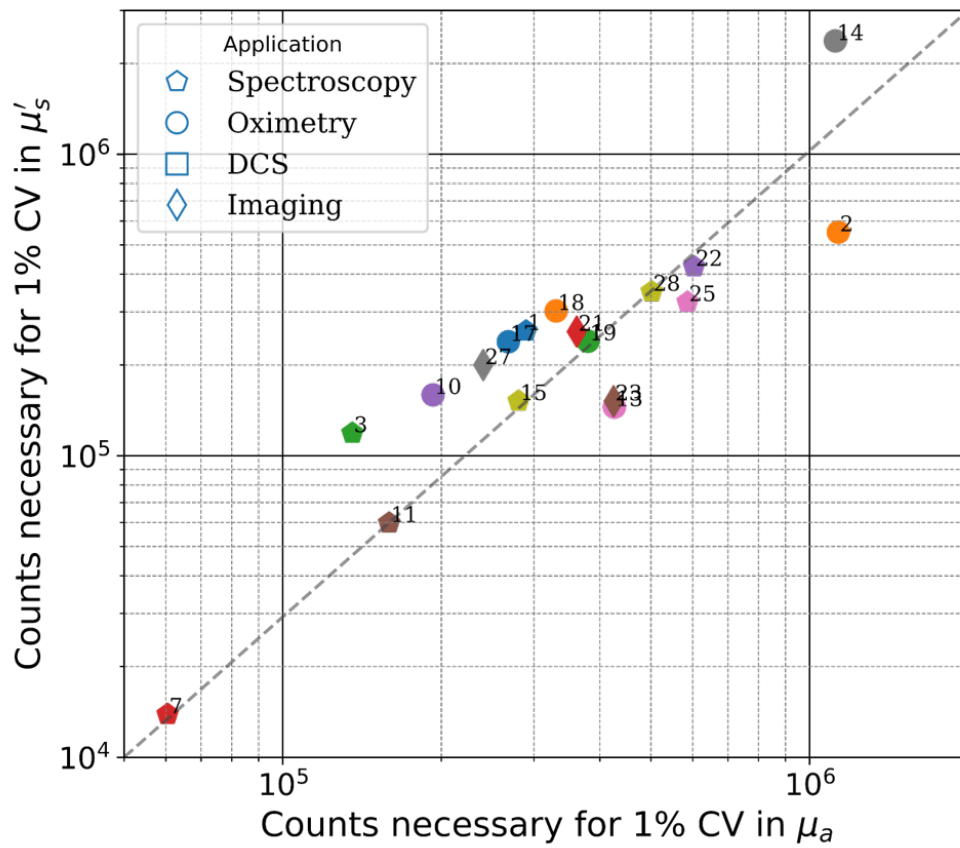


Figure 6.10: Figure of Merit plots for the Noise/Uncertainty measurement.

Reproducibility:

The reproducibility test, as the name suggests, is a general test of how reproducible the instrument is on a day-to-day basis. Fig. 6.11 displays the reproducibility among some of the instruments. Data were taken over 3 different measurement sessions (usually spanning 3 different days).

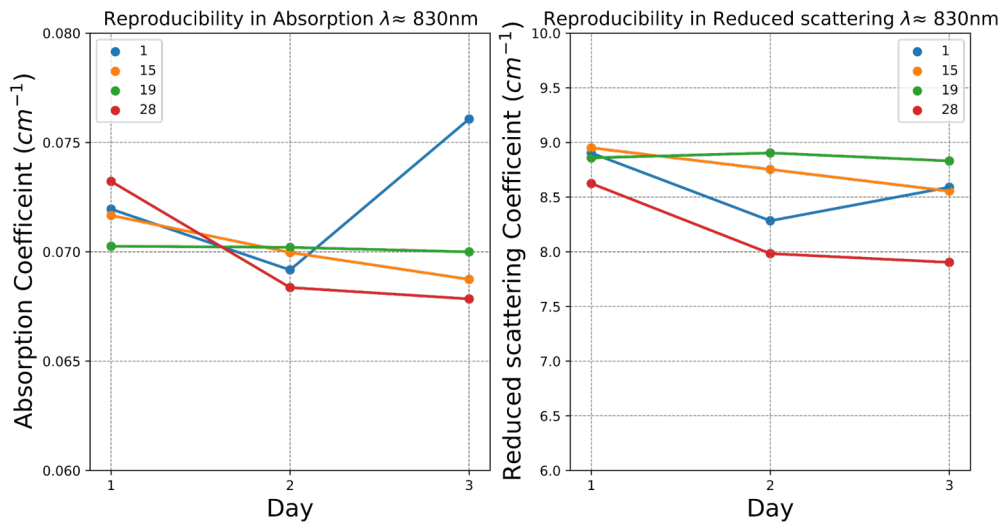


Figure 6.11: Plot of the day to day reproducibility in both the optical properties for some of the instruments (all measured on phantom B2 of the MEDPHOT series).

To determine a synthetic indicator for this case, the CV mentioned in the previous paragraph is reused. The coefficient of variation over the three measurements of absorption and reduced scattering for a given instruments are plotted against each other in Fig. 6.12. Generally ($\geq 70\%$), the reproducibility is better than 5% in both optical properties with some of them lower than even 1%. Such a testing is critical in a clinical scenario and in general represents a good scientific conduct. Instruments with relatively large values of CV can still be utilized as long as sufficient measures are taken to address this concern. A good example for this would be the commercial frequency domain instrument enrolled in this study #5 [143]. A phantom (manufactured by the company) with known optical properties is generally used to calibrate the performance of this instrument before clinical thus ensuring reliability and reproducibility in the results.

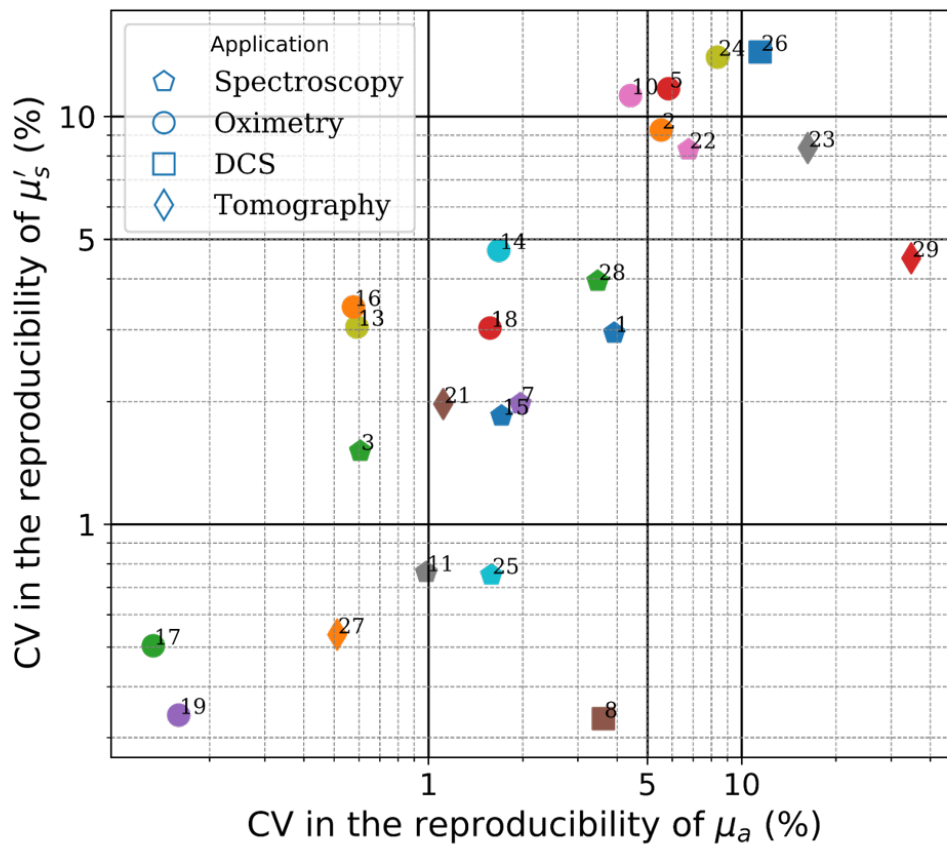


Figure 6.12: Figure of Merit plots for the reproducibility measurement.

6.3.3 the nEUROPt Protocol:

Developed in the context of time-domain brain imaging, this protocol primarily relies on the measured DTOF and the distribution of the counts as a function of time. This can however be easily extended to other modalities such as continuous wave and frequency domain. Two of the tests from this protocol were chosen for the BitMap Exercise namely the Contrast and Lateral Resolution tests. Of these, we present here the results from the contrast measurements.

Contrast:

To ascertain the depth sensitivity of instruments to localized optical perturbations – for e.g. functional imaging of brain activity – the systems were tested against an inhomogeneous phantom made of a bulk homogeneous material holding a rod with an embedded inclusion (see Fig 6.1(c)). A detailed description of the test can be found in [133]. Briefly, the test involved measuring the DTOF on the phantom seen in Fig. 6.1(c) in reflectance with the in-homogeneity moving deeper within the phantom. When the optodes are placed on the side surface of the phantom (at the positions marked in Fig. 6.1(c)) movement of the inclusion corresponds to depth scan.

Then the contrast is defined as the relative difference in counts given by:

$$C_i = (M_i - M_0)/M_0 \quad (6.2)$$

Here, C_i is the contrast at position i , M_i corresponds to the number of counts with the inclusion at position i and M_0 is the number of counts on the DTOF measured on a homogeneous region (far from the inclusion) of the phantom.

Since each measurement was repeated for 20 times, this also allowed for a calculation of the Contrast-to-noise ratio (CNR) given by

$$CNR_i = (M_i - M_0)/\sigma(M_0) \quad (6.3)$$

Here, $\sigma(M_0)$ refers to the standard deviation of the 20 acquisitions performed at each position at the baseline/homogeneous state.

The inclusion used for this exercise has a diameter of 5mm and a length of 5mm. The equivalent perturbation/inhomogeneity in absorption ($\Delta\mu_a$) achieved by this inclusion is 0.17 cm^{-1} supposing an effective volume of 1 cm^3 [144].

As mentioned above, the test could be performed on CW instruments as well. However, as evident from the figure, this tests requires that the optodes of the instruments to be separated from one another and fixed on either side of the rod with the inhomogeneity. Moreover, this measurement can be performed only in reflectance. With these these stipulations 18 of the 29 instruments enrolled for the BitMap Exercise were eligible for this measurement.

The two parameters described above, namely the Contrast and the Contrast to Noise ratio will be used as the synthetic indicators for this test. For time domain instrumentation, the resultant DTOFs can be gated in time and the counts from the resultant "time-windows" or "time-gates" can be inserted in the Eq. 6.2 and Eq. 6.3 to get the contrast and CNR at specific time-gates. The DTOFs measured in the BitMap exercise were divided into time windows of 400ps gates which were then used to plot the contrast at early and late gates.

Exemplary plots of contrast and CNR for the depth scan at an "early" (corresponding to the time interval 800-1200ps) and "late" gate (corresponding to the time interval 2000-2400ps) for instrument #16 can be found in Fig 6.13(a). The contrast plots at early and late gates suggest that for early time windows or gates the peak contrast is observed at shallower depths (at around 7mm in this case) while the late gates see maximum contrast at deeper regions (around 11mm). The CNR values as a function of depth have profiles similar to the contrast profiles. The maximum value of CNR at the early gate is, however, much higher than the maximum value at a late gate (logarithmic axis).

The contrast and CNR values at the late gate at a depth of 20mm were chosen as the two synthetic indicators for the figure of merit plot for this particular test. Since the concept of gating is applicable only to the TD instruments the contrast and CNR values of the CW instruments were calculated as a function of the total counts measured. The resultant figure of merit plot is shown in Fig 6.13(b).

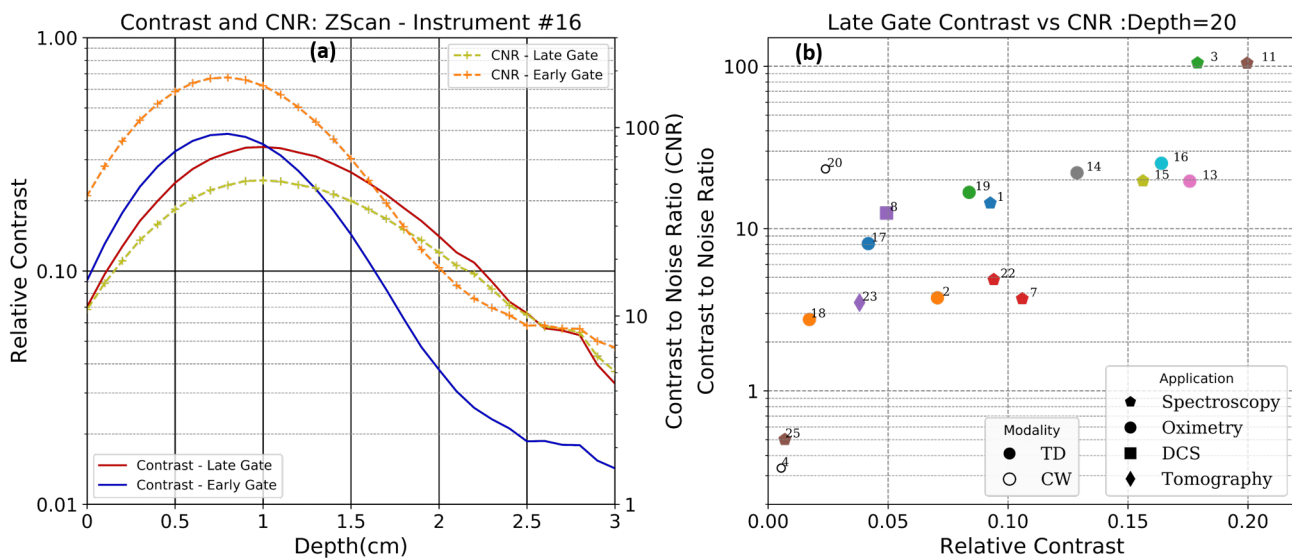


Figure 6.13: (a) Depth dependent Contrast and CNR values plotted against the inclusion depth for the Z-scan for an early and late time gate. (b) Figure of Merit plot for the contrast test of the nEUROPt protocol (Contrast vs CNR at an inclusion depth of 20mm).

A good spread is evident both in contrast and CNR values over all the instruments enrolled. Literature suggests that the depth dependent contrast is influenced by the instrument response (IRF) [134]. This is confirmed from the observation since all the instruments which have hybrid PMT or MCP based detection system (i.e. # 11, 3, 13, 14 and 15) are clustered at the top right corner of the plot suggestive of better contrast and CNR values. This could be attributed the IRF profiles of these instruments which have a fast decaying tail with almost negligible influence at later photon arrival times. On the contrary, silicon based detectors have an exponentially decaying tail [145] which could affect the performance of the instruments employing these detectors (# 1, 2, 22, 23, 25, 19) thus leading to relatively lower values of contrast. Similarly, higher values of CNR were observed for instruments with higher responsivity (see sec 6.3) since

higher value of responsivity implies lower photon noise for the same acquisition time and inter-fiber distance. CW instruments (empty markers) show very low values of contrast suggesting poor resolution at large depths (20mm). Lack of proper contact with the surface of the phantom due to the unusual design of the detection fiber for instrument #25 (discussed in chapter 2) could explain the extremely low contrast and CNR values for this instrument.

6.4 Conclusions:

In conclusion, a first of its kind, multi-laboratory performance assessment exercise named the BitMap Exercise has been initiated. This exercise aims at enforcing a culture of Performance Assessment and Standardization in the diffuse optics community with particular outlook for clinical application. A total of 31 instruments have been enrolled for the exercise of which 29 instruments have concluded the Action 1, with the goal to test the instruments on the same phantom kits, implementing shared Protocols (BIP, MEDPHOT, nEUROPt). The instruments were widely varying in terms of TRL (from subsystem realizations in the lab up to commercial clinical devices), modalities (time-domain, frequency-domain, continuous wave and spatial frequency domain imaging) and different applications (spectroscopy, oximetry, imaging and blood flow). The systems were challenged against various figures of merits such as responsivity as measure of photon harvesting efficiency, accuracy and linearity in the retrieval of homogeneous optical properties, stability and reproducibility of the measurement and contrast as indicator of sensitivity to deep optical perturbations.

The exercise has already generated sufficient interest in the community and has been presented multiple times at EU level workshops intended for standardization and performance assessment in the field of biophotonics [146], [147]. Action 1 and the results presented here are first level analysis of the data generated from the exercise and the data procured from this exercise is aimed to be deployed in open data repositories for consumption and benefit of the other important players in the field. Future efforts are aimed also to perform cross analysis of the entire data-set using common analysis procedures and use the data to train and improve different analysis algorithms.

CHAPTER 7

Conclusions:

The advances and developments achieved during this thesis can be summarized as follows.

- Broadband DOS for Heterogeneous Diffusive Media:
 1. Development of a clinical-grade, portable, broadband TD- DOS instrumentation, functional in the wavelength range of 600 - 1100nm, with the ability to perform measurements at multiple inter-fiber distances thus useful to disentangle the optical properties of depth wise heterogeneous tissues.
 2. Broadband validation of an analytical method for multi-layered geometries based on relative multi-distance measurements on tissue mimicking silicon phantoms and ex-vivo biological tissue and finally some initial applications *in-vivo*.
 3. Multi-distance broadband measurements *in-vivo* to investigate the optical properties and stratified nature of human abdominal region in healthy adult volunteers.
- Broadband TD-DOS monitoring of different ex-vivo tissues and organs with particular emphasis on understanding the influence of thermal damage on the variation of the tissue optical properties.
- Initiation of one of the largest multi-laboratory exercises (the BitMap exercise) aimed at enforcing a culture of standardization and performance assessment at an international level.

The study performed on the human abdomen *in-vivo* highlights some of the key deficiencies in using the standard homogeneous model of analysis while dealing with

Chapter 7. Conclusions:

such stratified structures. Thus a future step in this direction is aimed at developing and validating more multi-layered analysis models that can help improve the accuracy in disentangling the different layers optically. In the coming weeks the developed instrument will be installed at an hospital in Verona (Italy) for the non-invasive monitoring of physical frailty in the elderly obese.

Also, the study performed on monitoring the thermal treatment of tissues and organs using TD-DOS provides interesting biomarkers which need to be further validated and understood with the ultimate aim of providing valuable real-time feedback to a radiologist using any thermal treatment modality for malignant tissue ablation.

Finally, some future directions with regards to the BitMap exercise is a deployment of the data-set on an open data platform and test common analysis methodologies all of which could be of great value to the community at large. II

APPENDIX *A*

Supplementary Information for Chapter 4

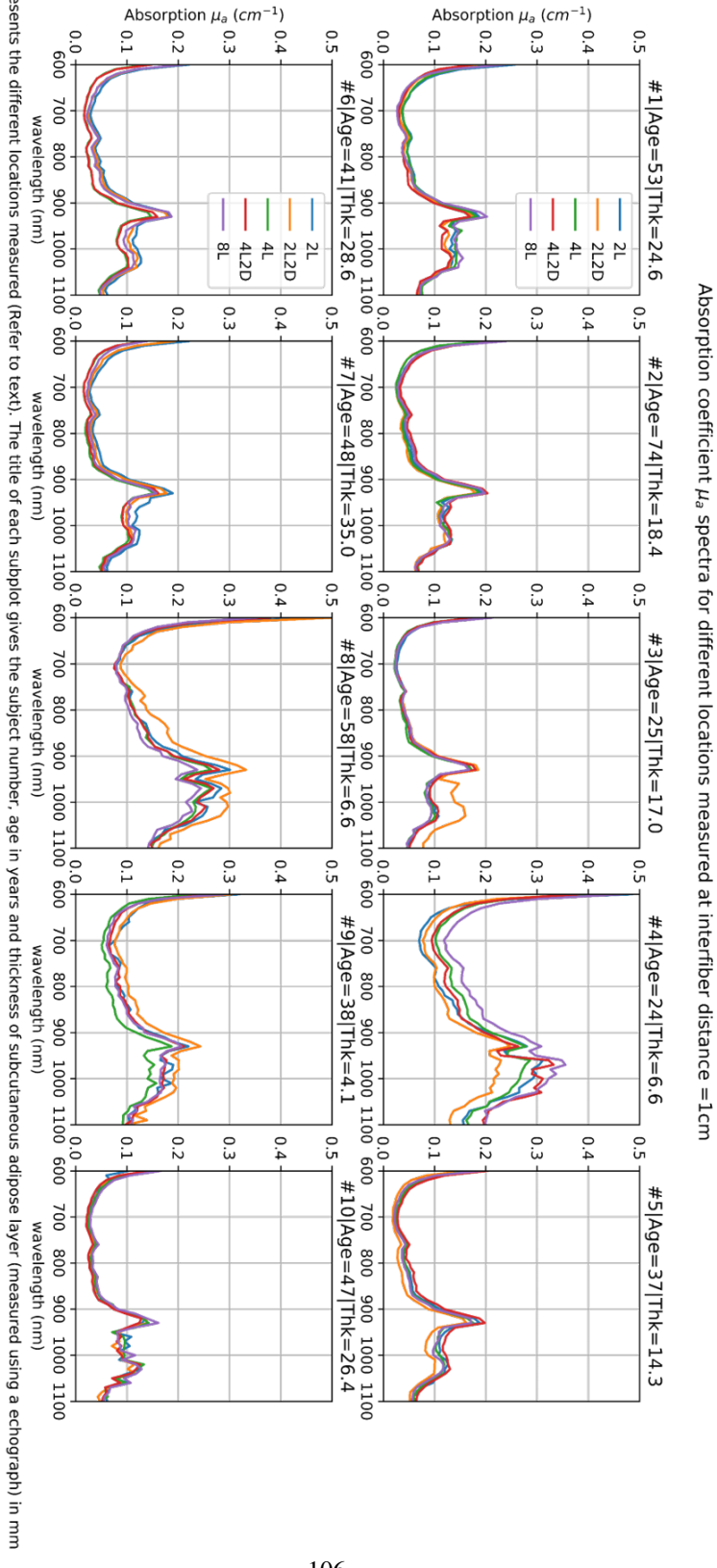
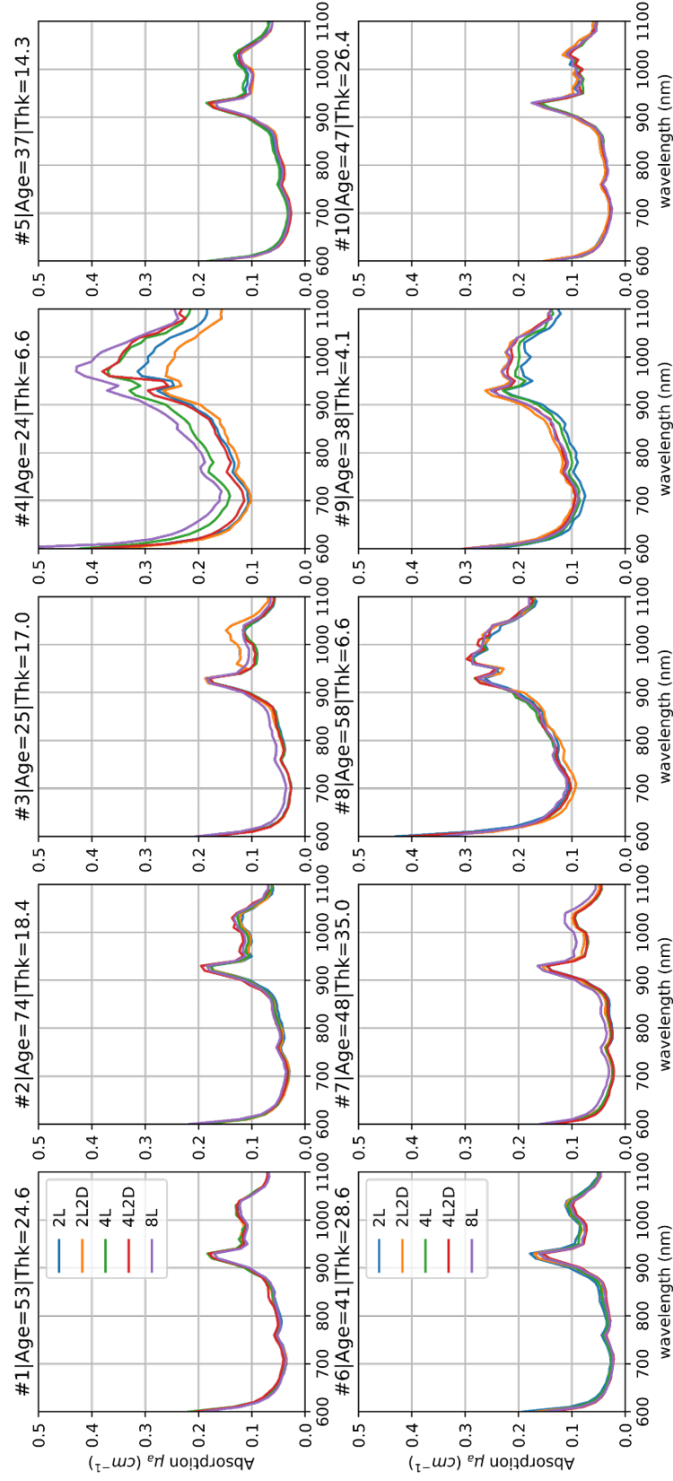


Figure A.1: Absorption spectra for different locations (see legend) measured at the inter-fiber distance of 1 cm

Absorption coefficient μ_a spectra for different locations measured at interfiber distance = 2cm



The legend represents the different locations measured (Refer to text). The title of each subplot gives the subject number, age in years and thickness of subcutaneous adipose layer (measured using a echograph) in mm

Figure A.2: Absorption spectra for different locations (see legend) measured at the inter-fiber distance of 2 cm

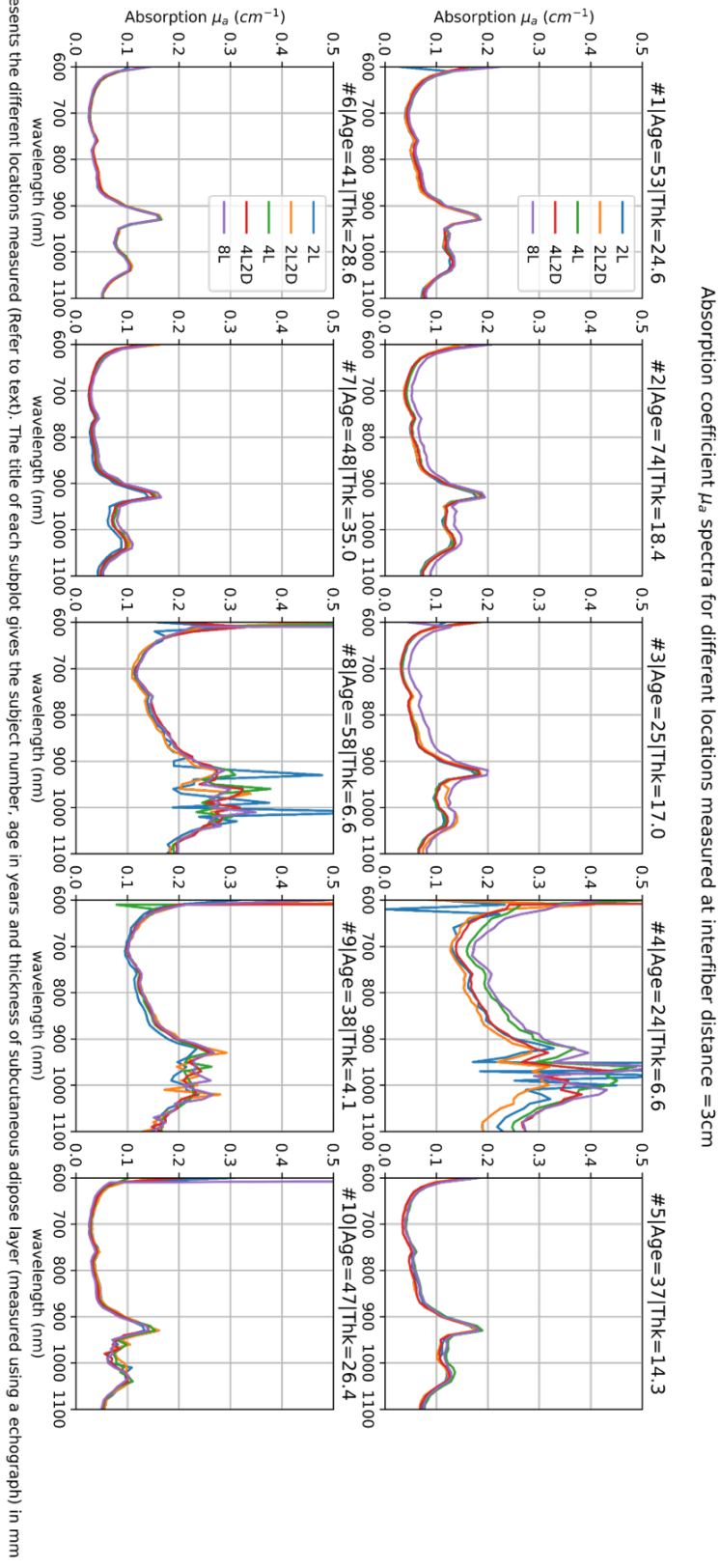
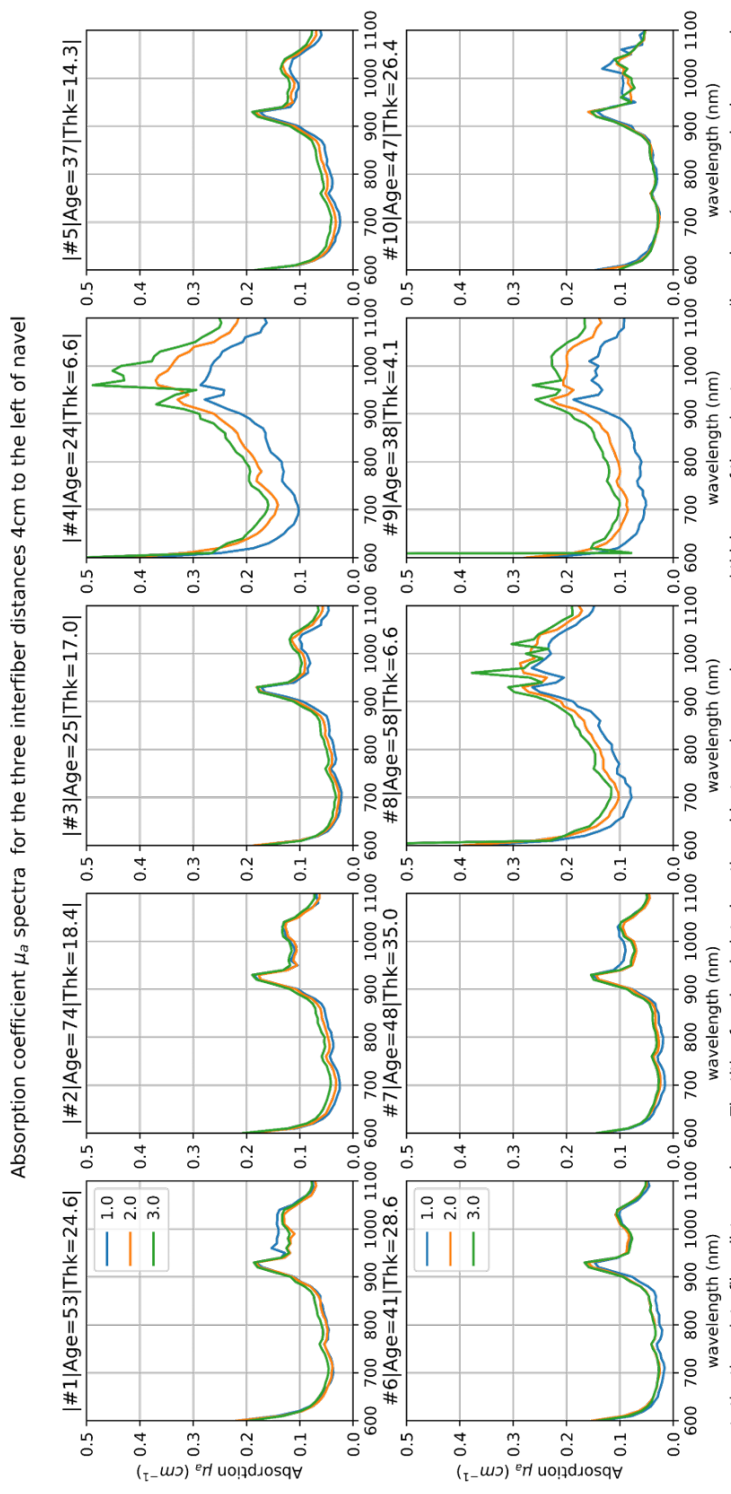


Figure A.3: Absorption spectra for different locations (see legend) measured at the inter-fiber distance of 2 cm



The legend represents the three interfiber distances in cm. The title of each subplot gives the subject number, age in years and thickness of the subcutaneous adipose layer(measured using an echograph) in mm

Figure A.4: Comparison of absorption spectra for different inter-fiber distances (see legend) measured at the location 4 cm to the left of the navel

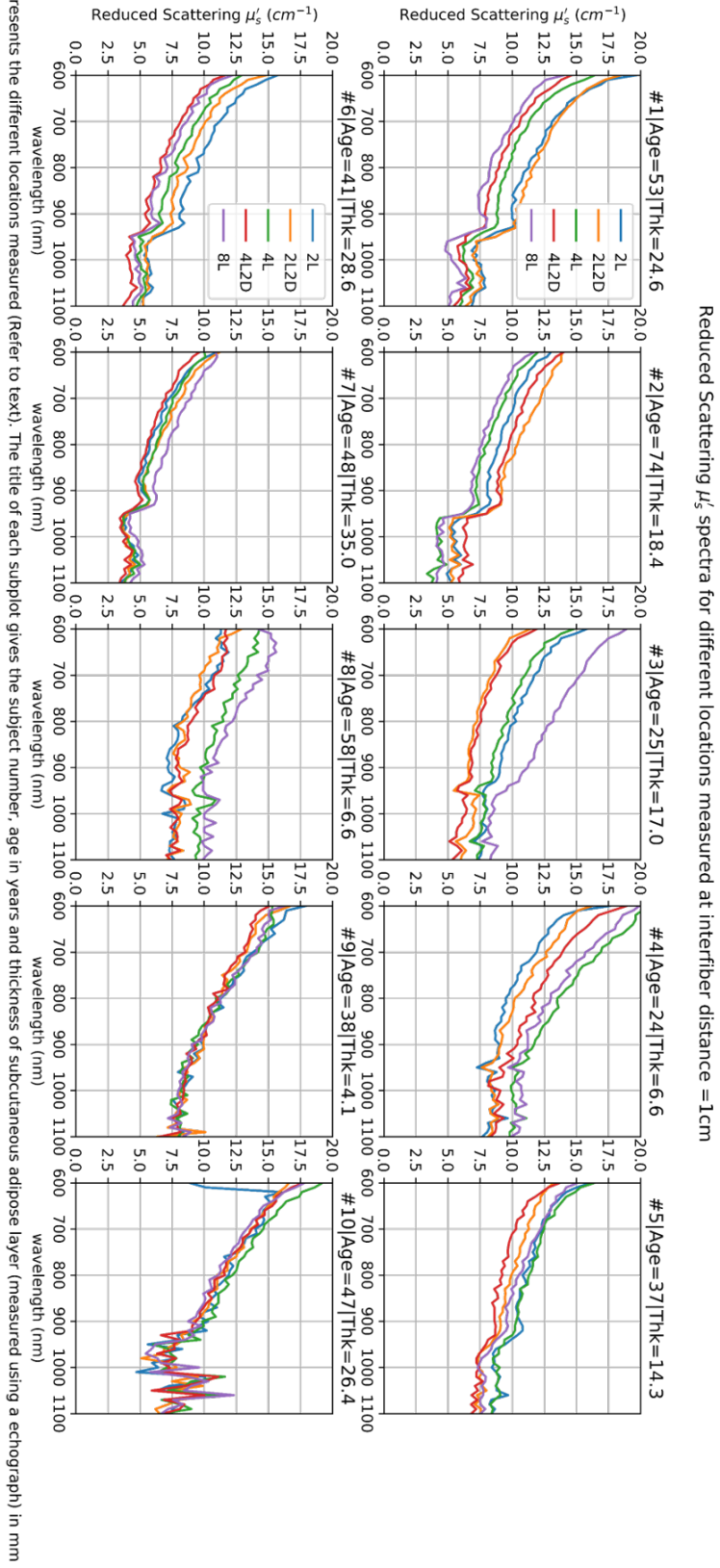


Figure A.5: Reduced scattering for different locations (see legend) measured at the inter-fiber distance of 3 cm

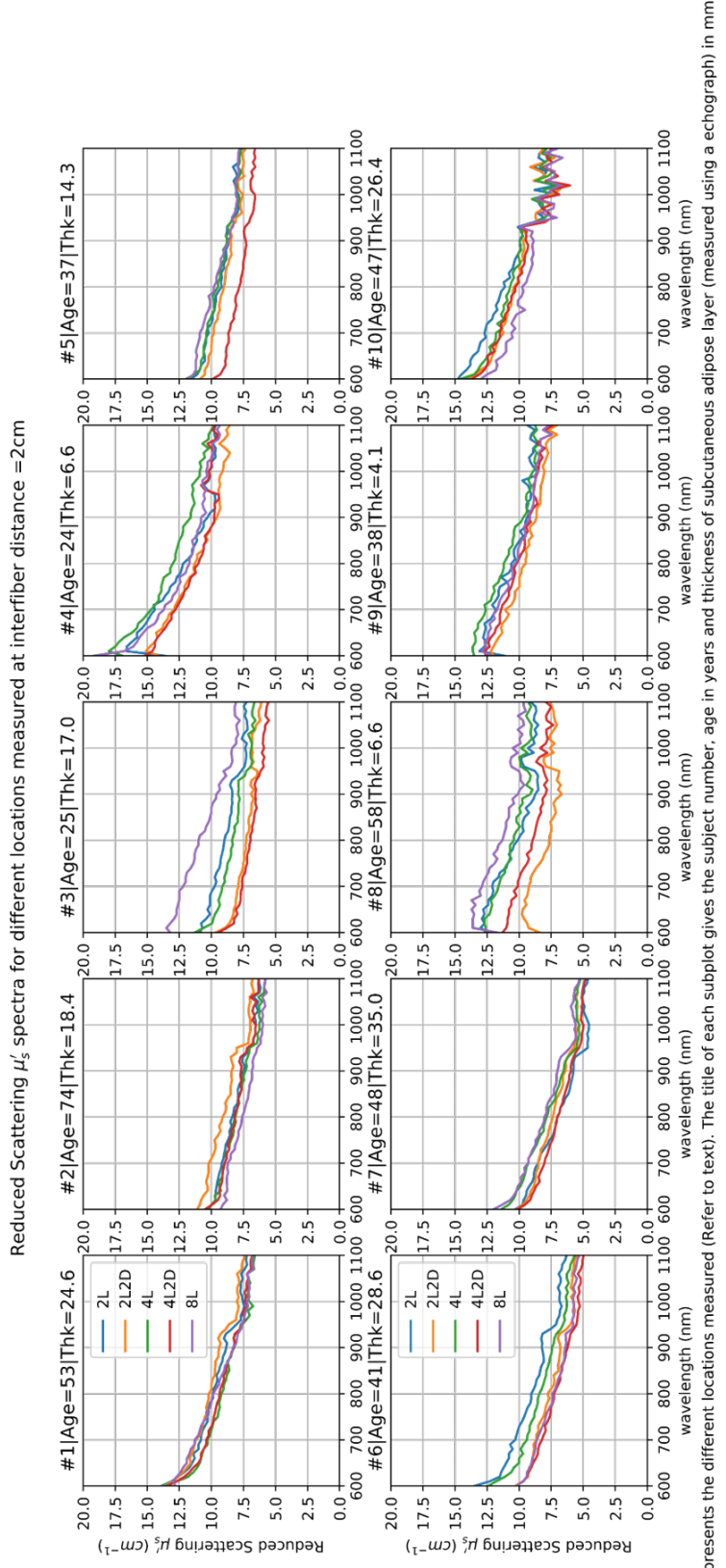


Figure A.6: Reduced scattering for different locations (see legend) measured at the inter-fiber distance of 3 cm

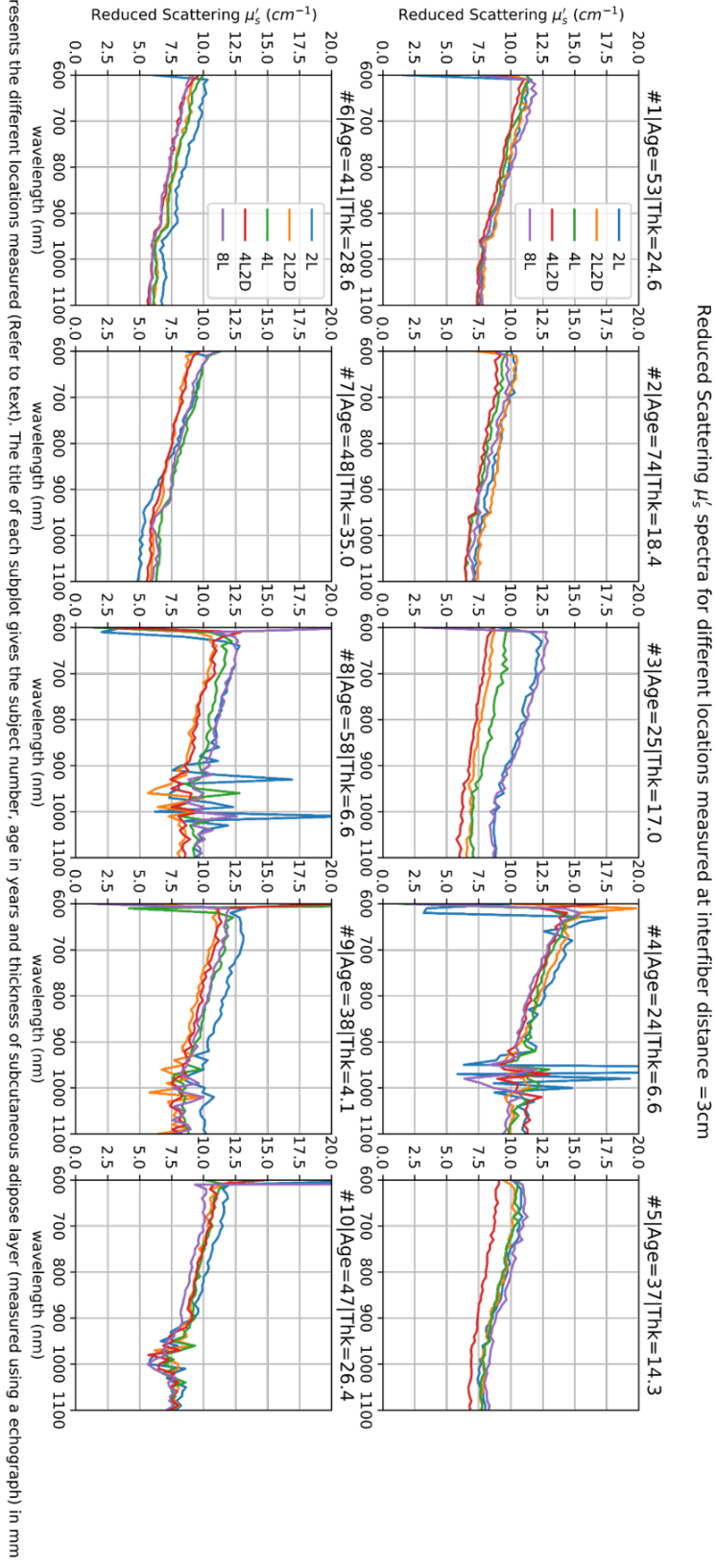


Figure A.7: Reduced scattering spectra for different locations (see legend) measured at the inter-fiber distance of 3 cm

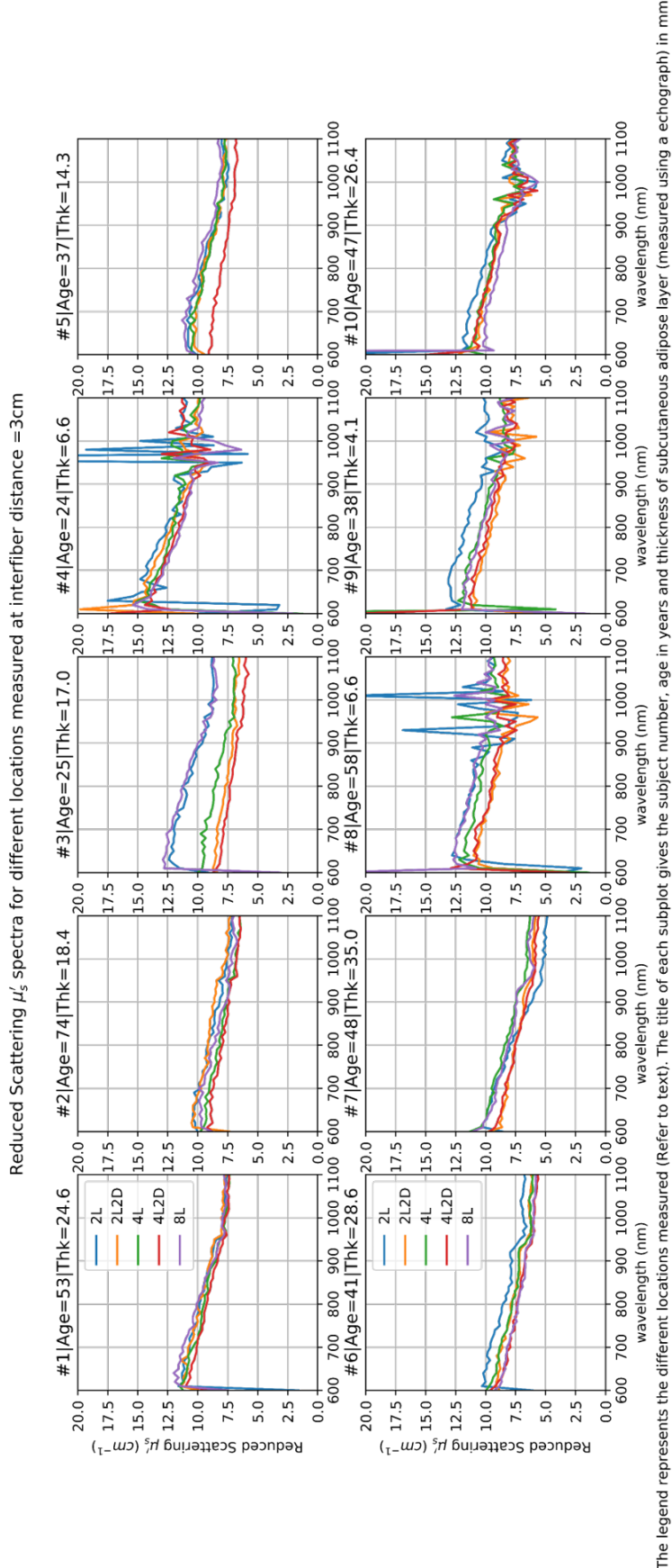


Figure A.8: Comparison of reduced scattering spectra for different inter-fiber distances (see legend) measured at the location 4 cm to the left of the navel

APPENDIX *B*

Supplementary Information for Chapter 5

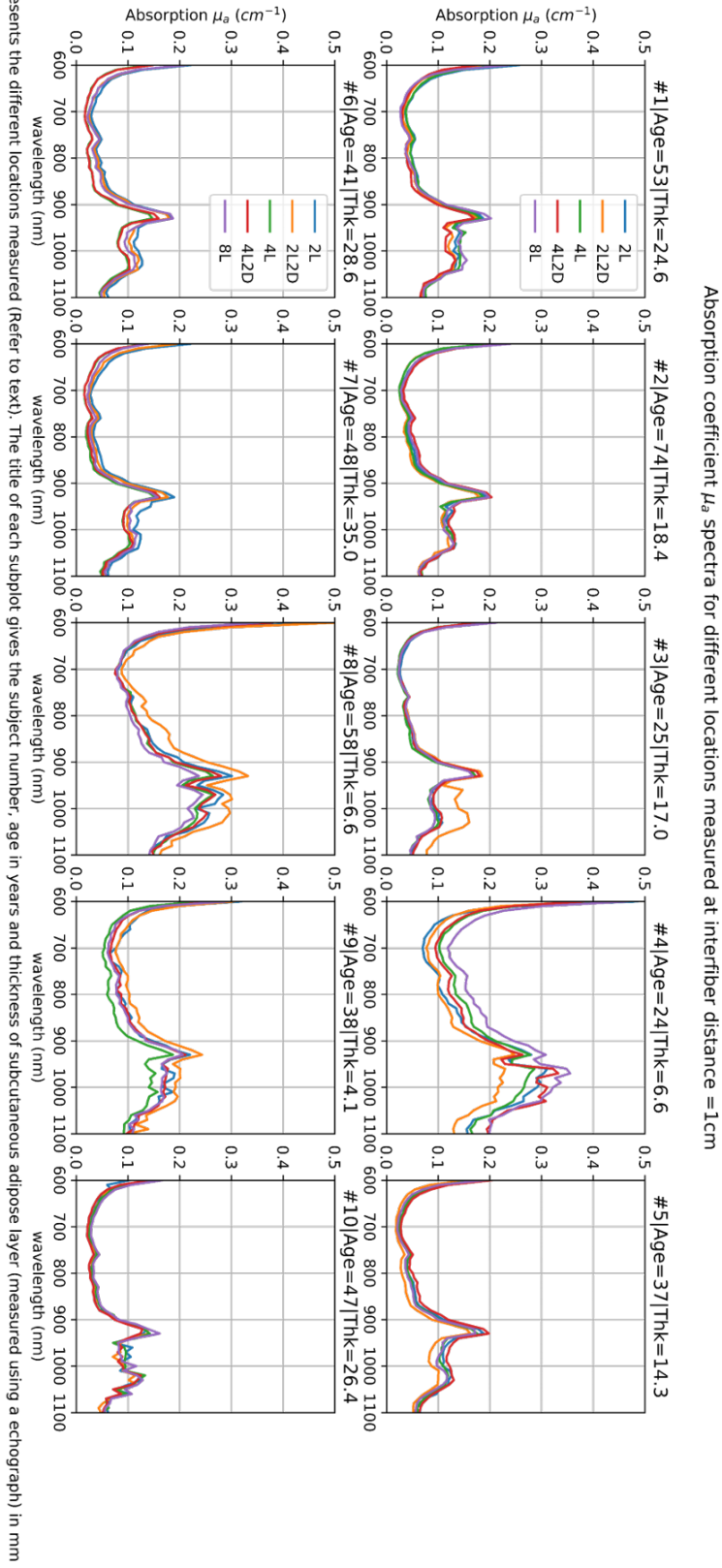
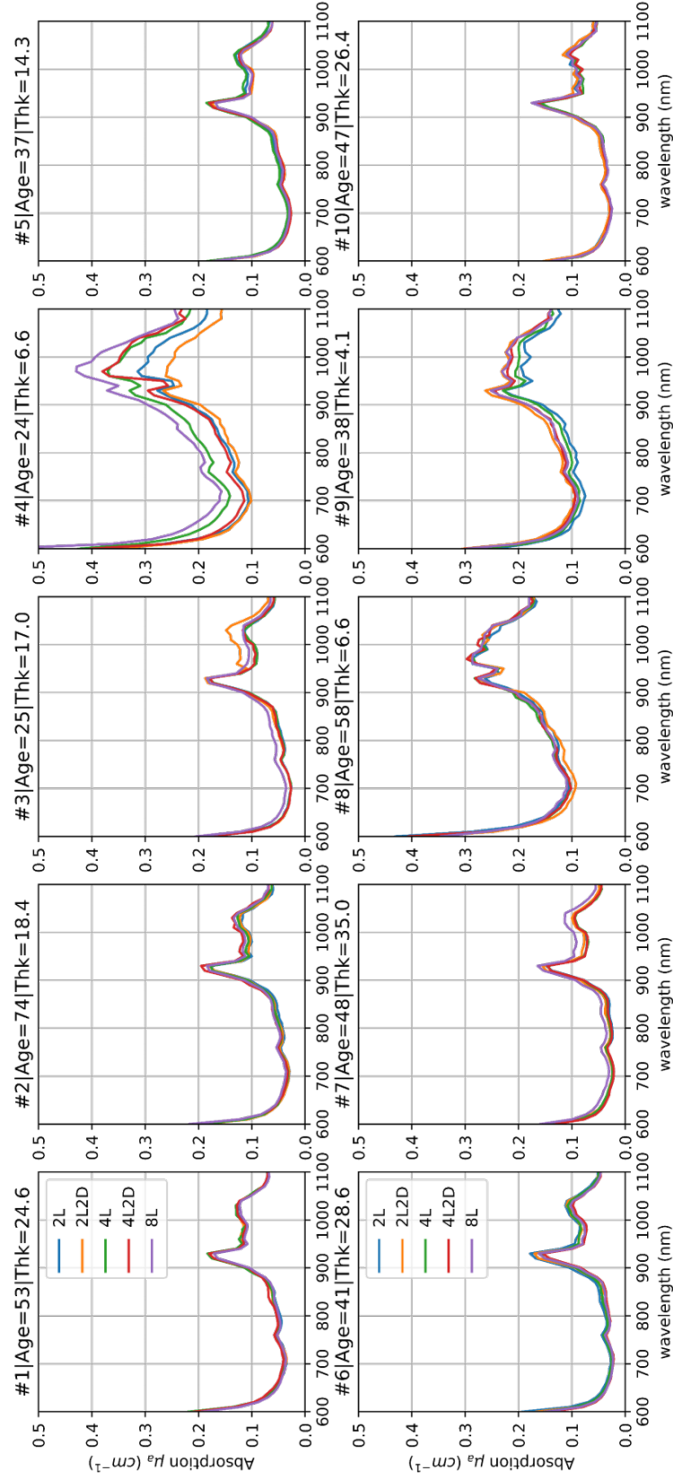


Figure B.1: Absorption spectra for different locations (see legend) measured at the inter-fiber distance of 1 cm

Absorption coefficient μ_a spectra for different locations measured at interfiber distance = 2cm



The legend represents the different locations measured (Refer to text). The title of each subplot gives the subject number, age in years and thickness of subcutaneous adipose layer (measured using an echograph) in mm

Figure B.2: Absorption spectra for different locations (see legend) measured at the inter-fiber distance of 2 cm

Appendix B. Supplementary Information for Chapter 5

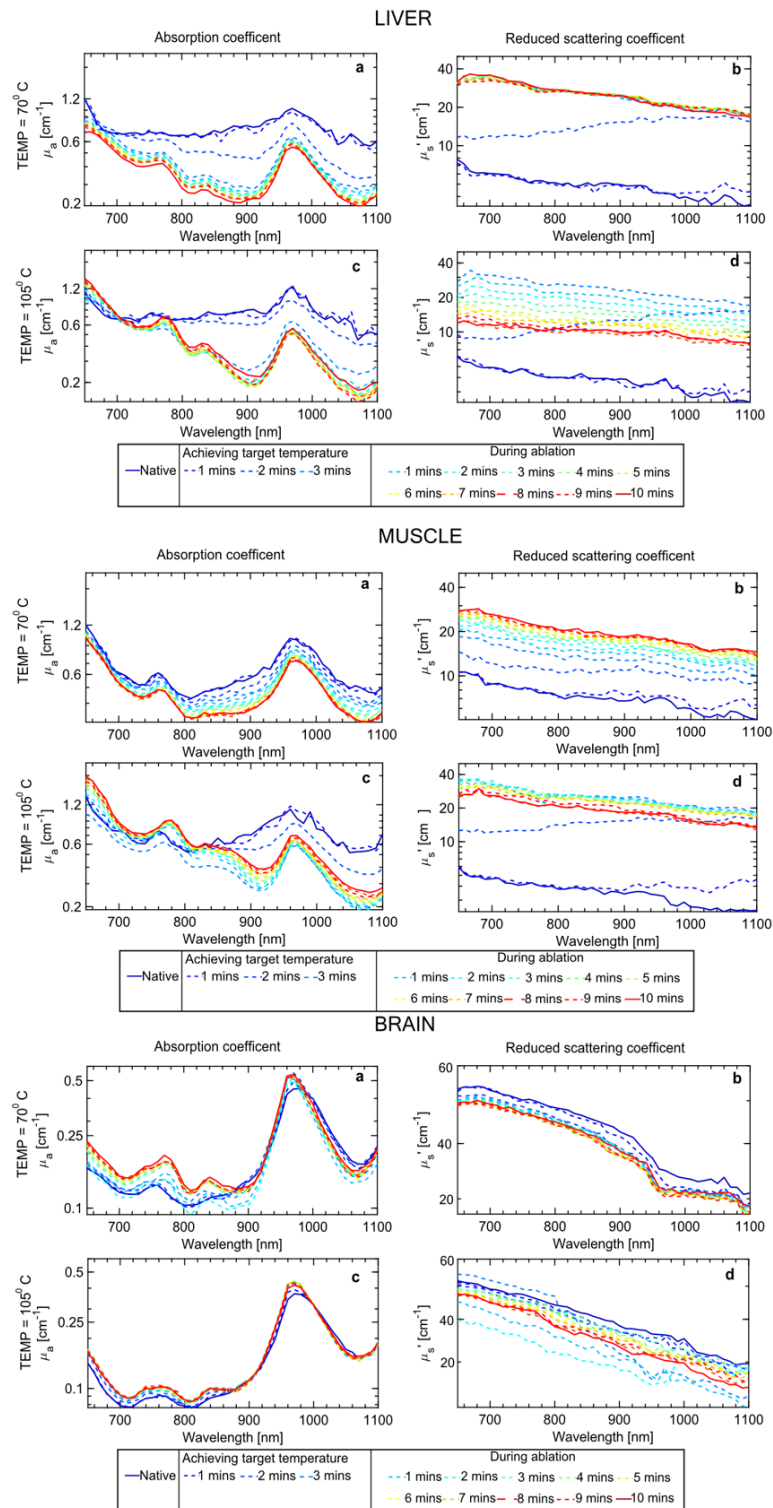


Figure B.3: Evolution of optical property spectra with RF treatment - Broadband absorption (a and c) and reduced scattering coefficient (b and d) spectra of the tissues during the RF based thermal treatment at the two temperatures. The native tissue spectra are always plotted in blue line. As mentioned earlier, the acquisition time per one spectrum is 1 minute. The RF instrument takes a time of less than 3 minutes to achieve either of the target temperatures. Once the target temperature is achieved the RF device treats the tissue by fixing the temperature for a span of 10 minutes. Hence in total a set of 13 spectra are acquired during the RF based thermal treatment.

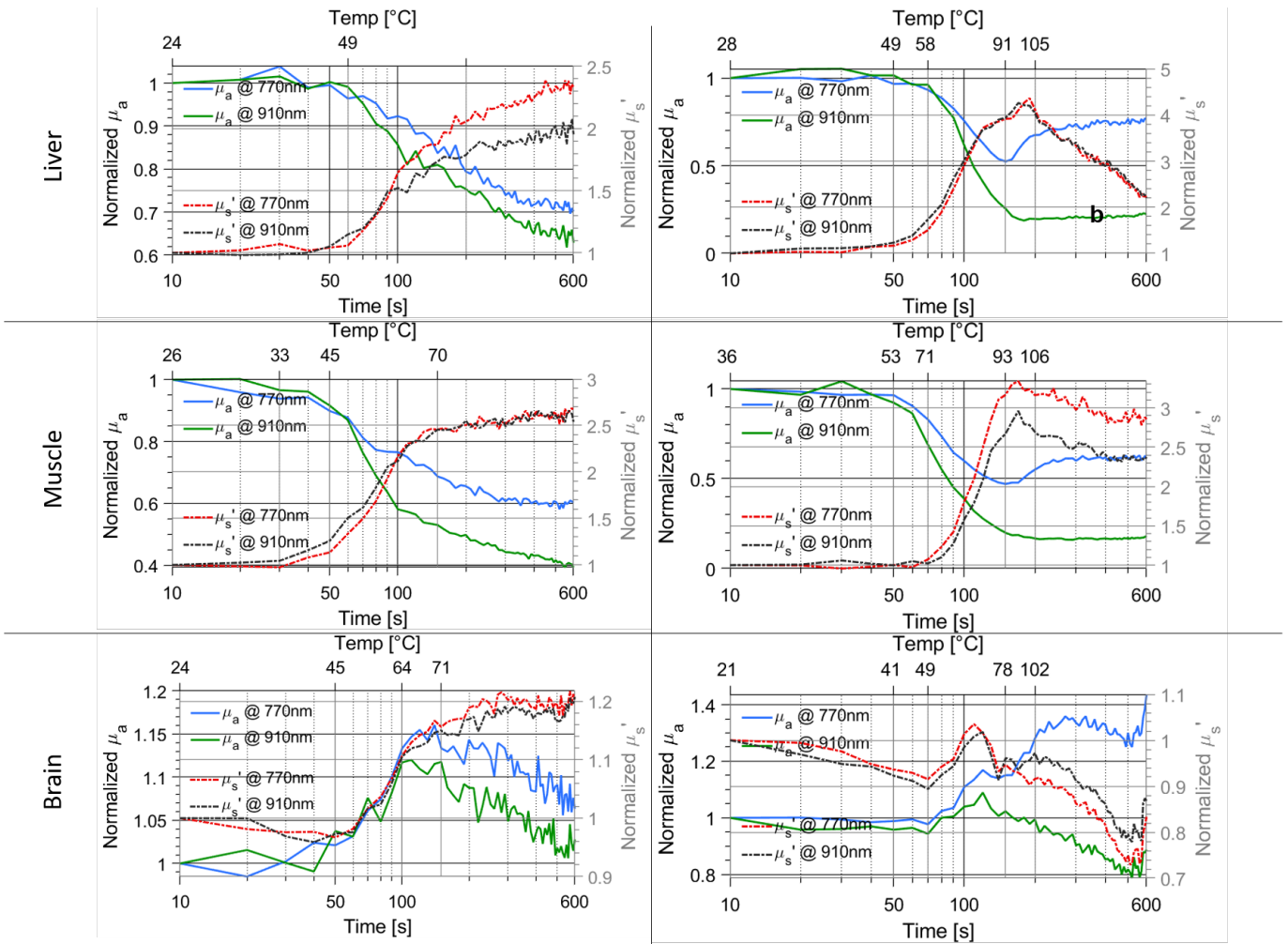


Figure B.4: Time evolution of optical properties at select wavelengths with RF treatment A total of five wavelengths (770,840,910, 980 and 1060nm) were chosen to monitor closely the key spectral changes observed in Fig. 5.6. Fig. 5.8 a and b chart the variation of both the optical properties at two (770 and 910nm) of these five wavelengths for the 70°C and 105°C respectively. The time axes (x-axis) in these graphs are logarithmic and the y axes represents the value of the optical property normalized to the value of the native tissue. The average temperature of the RF electrode at specific time points is given on the temperature axis on the top of each graph.

Bibliography

- [1] A. Messiah, *Quantum Mechanics*. Dover, 1999.
- [2] J. C. Maxwell, «On physical lines of force», *Philosophical Magazine*, vol. 90, no. S1, pp. 11–23, 2010.
- [3] P. Taroni, A. Pifferi, A. Torricelli, D. Comelli, and R. Cubeddu, «In vivo absorption and scattering spectroscopy of biological tissues», *Photochemical & Photobiological Sciences*, vol. 2, no. 2, pp. 124–129, 2003.
- [4] G. Strangman, D. A. Boas, and J. P. Sutton, «Non-invasive neuroimaging using near-infrared light», *Biological psychiatry*, vol. 52, no. 7, pp. 679–693, 2002.
- [5] A. E. Cerussi, N. S. Shah, D. Hsiang, A. Durkin, J. A. Butler, and B. J. Tromberg, «In vivo absorption, scattering, and physiologic properties of 58 malignant breast tumors determined by broadband diffuse optical spectroscopy», *Journal of biomedical optics*, vol. 11, no. 4, p. 044 005, 2006.
- [6] P. Taroni, A. M. Paganoni, F. Ieva, F. Abbate, E. Cassano, R. Cubeddu, and A. Pifferi, «Is collagen an independent risk factor for breast cancer?», in *Clinical and Translational Biophotonics*, Optical Society of America, 2016, TTh4B–3.
- [7] A. Pifferi, J. Swartling, E. Chikoidze, A. Torricelli, P. Taroni, A. L. Bassi, S. Andersson-Engels, and R. Cubeddu, «Spectroscopic time-resolved diffuse reflectance and transmittance measurements of the female breast at different interfiber distances», *Journal of biomedical optics*, vol. 9, no. 6, pp. 1143–1152, 2004.
- [8] G. Strangman, D. A. Boas, and J. P. Sutton, «Non-Invasive Neuroimaging Using Near-Infrared Light», English, *Society of Biological Psychiatry*, vol. 52, pp. 679–693, 2002.
- [9] S. K. V. Sekar, A. Farina, A. Dalla Mora, C. Lindner, M. Pagliazzi, M. Mora, G. Aranda, H. Dehghani, T. Durduran, P. Taroni, *et al.*, «Broadband (550–1350 nm) diffuse optical characterization of thyroid chromophores», *Scientific reports*, vol. 8, no. 1, p. 10 015, 2018.
- [10] J. R. Mourant, T. Fuselier, J. Boyer, T. M. Johnson, and B. J., «Prediction and measurements of scattering and absorption over broad wavelength ranges in tissue phantoms», English, *Appl. Opt.*, vol. 36, no. 4, pp. 386–396, 1997.
- [11] D. A. Boas, L. Campbell, and A. G. Yodh, «Scattering and imaging with diffusing temporal field correlations», *Physical review letters*, vol. 75, no. 9, p. 1855, 1995.
- [12] D. A. Boas and A. G. Yodh, «Spatially varying dynamical properties of turbid media probed with diffusing temporal light correlation», *JOSA A*, vol. 14, no. 1, pp. 192–215, 1997.

Bibliography

- [13] D. Delpy and M. Cope, «Quantification in tissue near-infrared spectroscopy», *Philosophical Transactions of the Royal Society of London. Series B: Biological Sciences*, vol. 352, no. 1354, pp. 649–659, 1997.
- [14] L. Wang, S. L. Jacques, and L. Zheng, «MCML—Monte Carlo modeling of light transport in multi-layered tissues.», *Comput. Methods Programs Biomed.*, vol. 47, no. 2, pp. 131–146, 1995.
- [15] E. L. Hull, M. G. Nichols, and T. H. Foster, «Localization of luminescent inhomogeneities in turbid media with spatially resolved measurements of cw diffuse luminescence emittance», *Applied optics*, vol. 37, no. 13, pp. 2755–2765, 1998.
- [16] V. Quaresima, S. J. Matcher, and M. Ferrari, «Identification and quantification of intrinsic optical contrast for near-infrared mammography», *Photochemistry and photobiology*, vol. 67, no. 1, pp. 4–14, 1998.
- [17] T. J. Farrell, M. S. Patterson, and B. Wilson, «A diffusion theory model of spatially resolved, steady-state diffuse reflectance for the noninvasive determination of tissue optical properties in vivo», *Medical physics*, vol. 19, no. 4, pp. 879–888, 1992.
- [18] B. W. Pogue and M. S. Patterson, «Frequency-domain optical absorption spectroscopy of finite tissue volumes using diffusion theory», *Phys. Med. Biol.*, vol. 39, no. 7, pp. 1157–1180, 1994. [Online]. Available: <http://stacks.iop.org/0031-9155/39/1157>.
- [19] M. S. Patterson, B. Chance, and B. C. Wilson, «Time resolved reflectance and transmittance for the noninvasive measurement of tissue optical properties», English, *Appl. Opt.*, vol. 28, no. 12, pp. 2331–2336, 1989.
- [20] A. Gibson, J. Hebden, and S. R. Arridge, «Recent advances in diffuse optical imaging», *Physics in Medicine & Biology*, vol. 50, no. 4, R1, 2005.
- [21] G. Yu, T. Durduran, D. Furuya, J. H. Greenberg, and A. G. Yodh, «Frequency-domain multiplexing system for in vivo diffuse light measurements of rapid cerebral hemodynamics», *Applied optics*, vol. 42, no. 16, pp. 2931–2939, 2003.
- [22] H. E. D’Arceuil, M. P. Hotakainen, C. Liu, G. Themelis, A. De Crespigny, and M. A. Franceschini, «Near-infrared frequency-domain optical spectroscopy and magnetic resonance imaging: a combined approach to studying cerebral maturation in neonatal rabbits», *Journal of biomedical optics*, vol. 10, no. 1, p. 011 011, 2005.
- [23] T. D. O’Sullivan, A. E. Cerussi, D. J. Cuccia, and B. J. Tromberg, «Diffuse optical imaging using spatially and temporally modulated light.», *Journal of biomedical optics*, vol. 17, no. 7, pp. 071 311–071 311, 2012.
- [24] A. Pifferi, A. Torricelli, P. Taroni, D. Comelli, A. Bassi, and R. Cubeddu, «Fully automated time domain spectrometer for the absorption and scattering characterization of diffusive media», *Rev. Sci. Instr.*, vol. 78, no. 5, 053103, p. 053 103, 2007. DOI: 10.1063/1.2735567. [Online]. Available: <http://link.aip.org/link/?RSI/78/053103/1>.
- [25] S. Gioux, A. Mazhar, and D. J. Cuccia, «Spatial frequency domain imaging in 2019: principles, applications, and perspectives», *Journal of Biomedical Optics*, vol. 24, no. 7, p. 071 613, 2019.
- [26] S. Chandrasekhar, *Radiative transfer*. Courier Corporation, 2013.
- [27] R. Sanchez and N. J. McCormick, «A review of neutron transport approximations», English, *Nucl. Sci. Eng.*, vol. 80, no. 4, pp. 481–535, 1982.
- [28] A. Ishimaru, «Diffusion of a pulse in densely distributed scatterers», *J. Opt. Soc. Am.*, vol. 68, no. 8, pp. 1045–1050, 1978. [Online]. Available: <http://www.opticsinfobase.org/abstract.cfm?URI=josa-68-8-1045>.
- [29] Z. Guo and S. Kumar, «Discrete-Ordinates Solution of Short-Pulsed Laser Transport in Two-Dimensional Turbid Media», *Appl. Opt.*, vol. 40, no. 19, pp. 3156–3163, 2001. [Online]. Available: <http://ao.osa.org/abstract.cfm?URI=ao-40-19-3156>.

- [30] S. Arridge, H. Dehghani, M. Schweiger, and E. Okada, «The finite element model for the propagation of light in scattering media: a direct method for domains with nonscattering regions», *Med. Phys.*, vol. 27, no. 1, pp. 252–264, 2000.
- [31] S. R. Arridge, M. Schweiger, M. Hiraoka, and D. T. Delpy, «A Finite Element Approach for Modeling Photon Transport in Tissue», *Med. Phys.*, vol. 20, no. 2, pp. 299–309, 1993.
- [32] M. Abramowitz and I. A. Stegun, *Handbook of Mathematical Functions with Formulas, Graphs, and Mathematical Tables*, ninth. New York: Dover, 1964.
- [33] D. Contini, F. Martelli, and G. Zaccanti, «Photon migration through a turbid slab described by a model based on diffusion approximation. I. Theory», English, *Appl. Opt.*, vol. 36, no. 19, pp. 4587–4599, 1997.
- [34] K. Furutsu, «Diffusion equation derived from space-time transport equation», *JOSA*, vol. 70, no. 4, pp. 360–366, 1980.
- [35] Y. Kuga, A. Ishimaru, and A. P. Bruckner, «Experiments on picosecond pulse propagation in a diffuse medium», *JOSA*, vol. 73, no. 12, pp. 1812–1815, 1983.
- [36] S. J. Madsen, B. C. Wilson, M. S. Patterson, Y. D. Park, S. L. Jacques, and Y. Hefetz, «Experimental tests of a simple diffusion model for the estimation of scattering and absorption coefficients of turbid media from time-resolved diffuse reflectance measurements», *Applied optics*, vol. 31, no. 18, pp. 3509–3517, 1992.
- [37] G. Yoon, S. A. Prahl, and A. J. Welch, «Accuracies of the diffusion approximation and its similarity relations for laser irradiated biological media», *Applied Optics*, vol. 28, no. 12, pp. 2250–2255, 1989.
- [38] J. J. Duderstadt and W. R. Martin, «Transport theory.», *Transport theory.*, by Duderstadt, JJ; Martin, WR. Chichester (UK): John Wiley & Sons, 10+ 613 p., 1979.
- [39] F. Martelli, S. Del Bianco, A. Ismaelli, and G. Zaccanti, *Light propagation through biological tissue*, 3.824746. SPIE press, 2010, vol. 10.
- [40] R. C. Haskell, L. O. Svaasand, T. Tsay, T. Feng, M. S. McAdams, and B. J. Tromberg, «Boundary conditions for the diffusion equation in radiative transfer», *J. Opt. Soc. Am. A*, vol. 11, no. 10, pp. 2727–2741, 1994. [Online]. Available: <http://josaa.osa.org/abstract.cfm?URI=josaa-11-10-2727>.
- [41] D. C. Comsa, T. J. Farrell, and M. S. Patterson, «Quantification of bioluminescence images of point source objects using diffusion theory models», *Physics in Medicine & Biology*, vol. 51, no. 15, p. 3733, 2006.
- [42] D. Ancora, «Light propagation in Extreme Conditions-The role of optically clear tissues and scattering layers in optical biomedical imaging», *arXiv preprint arXiv:1706.09409*, 2017.
- [43] W. H. Press, S. A. Teukolsky, W. T. Vetterling, and B. P. Flannery, «Numerical recipes in C++», *The art of scientific computing*, vol. 2, p. 1002, 1992.
- [44] J.-P. Bouchard, I. Veilleux, R. Jedidi, I. Noiseux, M. Fortin, and O. Mermet, «Reference optical phantoms for diffuse optical spectroscopy. Part 1—Error analysis of a time resolved transmittance characterization method», *Optics express*, vol. 18, no. 11, pp. 11 495–11 507, 2010.
- [45] E. Alerstam, T. Svensson, and S. Andersson-Engels, «Parallel computing with graphics processing units for high-speed Monte Carlo simulation of photon migration», *Journal of biomedical optics*, vol. 13, no. 6, p. 060 504, 2008.
- [46] S. Konugolu Venkata Sekar, A. Farina, A. Dalla Mora, C. Lindner, M. Pagliuzzi, M. Mora, G. Aranda, H. Dehghani, T. Durduran, P. Taroni, and A. Pifferi, «Broadband (550-1350 nm) diffuse optical characterization of thyroid chromophores», *Scientific Reports*, vol. 8, no. 1, pp. 1–8, 2018, ISSN: 20452322. DOI: 10 . 1038 / s41598 - 018 - 27684 - 8. [Online]. Available: <http://dx.doi.org/10.1038/s41598-018-27684-8>.

Bibliography

- [47] S. Konugolu Venkata Sekar, A. Dalla Mora, I. Bargigia, E. Martinenghi, C. Lindner, P. Farzam, M. Pagliuzzi, T. Durduran, P. Taroni, A. Pifferi, and A. Farina, «Broadband (600-1350 nm) Time-Resolved Diffuse Optical Spectrometer for Clinical Use», *IEEE Journal on Selected Topics in Quantum Electronics*, vol. 22, no. 3, pp. 406–414, 2016, ISSN: 1077260X. DOI: 10.1109/JSTQE.2015.2506613.
- [48] A. Kienle and T. Glanzmann, «In vivo determination of the optical properties of muscle with time-resolved reflectance using a layered model», *Physics in Medicine & Biology*, vol. 44, no. 11, p. 2689, 1999.
- [49] F. Martelli, S. Del Bianco, and G. Zaccanti, «Procedure for retrieving the optical properties of a two-layered medium from time-resolved reflectance measurements», *Optics Letters*, vol. 28, no. 14, p. 1236, 2003, ISSN: 0146-9592. DOI: 10.1364/ol.28.001236.
- [50] F. Martelli, S. Del Bianco, G. Zaccanti, A. Pifferi, A. Torricelli, A. Bassi, P. Taroni, and R. Cubeddu, «Phantom validation and in vivo application of an inversion procedure for retrieving the optical properties of diffusive layered media from time-resolved reflectance measurements», *Optics letters*, vol. 29, no. 17, pp. 2037–2039, 2004.
- [51] A. Dalla Mora, D. Contini, S. Arridge, F. Martelli, A. Tosi, G. Boso, A. Farina, T. Durduran, E. Martinenghi, A. Torricelli, *et al.*, «Towards next-generation time-domain diffuse optics for extreme depth penetration and sensitivity», *Biomedical optics express*, vol. 6, no. 5, pp. 1749–1760, 2015.
- [52] A. Pifferi, A. Torricelli, A. Bassi, P. Taroni, R. Cubeddu, H. Wabnitz, D. Grosenick, M. Moller, R. Macdonald, J. Swartling, T. Svensson, S. Andersson-Engels, R. L. P. van Veen, H. J. C. M. Sterenborg, J. M. Tualle, H. L. Nghiem, S. Avriller, M. Whelan, and H. Stamm, «Performance assessment of photon migration instruments: the MEDPHOT protocol», *English, Appl. Opt.*, vol. 44, no. 11, pp. 2104–2114, 2005.
- [53] R. C. Smith and K. S. Baker, «Optical properties of the clearest natural waters (200–800 nm)», *Applied optics*, vol. 20, no. 2, pp. 177–184, 1981.
- [54] K. F. Palmer and D. Williams, «Optical properties of water in the near infrared», *JOSA*, vol. 64, no. 8, pp. 1107–1110, 1974.
- [55] G. M. Hale and M. R. Querry, «Optical constants of water in the 200-nm to 200- μ m wavelength region», *Applied optics*, vol. 12, no. 3, pp. 555–563, 1973.
- [56] *EUR-Lex - 32017R0745 - EN - EUR-Lex*, [Online; accessed 19. Feb. 2020], Feb. 2020. [Online]. Available: <https://eur-lex.europa.eu/legal-content/EN/TXT/?uri=CELEX:32017R0745>.
- [57] T. H. Pham, T. Spott, L. O. Svaasand, and B. J. Tromberg, «Quantifying the properties of two-layer turbid media with frequency-domain diffuse reflectance.», *Applied optics*, 2000, ISSN: 1559-128X.
- [58] O. Pucci, V. Toronov, and K. St. Lawrence, «Measurement of the optical properties of a two-layer model of the human head using broadband near-infrared spectroscopy», *Applied Optics*, vol. 49, no. 32, p. 6324, 2010, ISSN: 0003-6935. DOI: 10.1364/AO.49.006324. [Online]. Available: <https://www.osapublishing.org/abstract.cfm?URI=ao-49-32-6324>.
- [59] A. Kienle, T. Glanzmann, G. Wagnieres, and H. van den Bergh, «Investigation of two-layered turbid media with time-resolved reflectance», *Applied optics*, vol. 37, no. 28, pp. 6852–6862, 1998.
- [60] A. Pifferi, A. Torricelli, P. Taroni, and R. Cubeddu, «Reconstruction of absorber concentrations in a two-layer structure by use of multidistance time-resolved reflectance spectroscopy», *Optics letters*, vol. 26, no. 24, pp. 1963–1965, 2001.
- [61] M. Shimada, Y. Hoshi, and Y. Yamada, «Simple algorithm for the measurement of absorption coefficients of a two-layered medium by spatially resolved and time-resolved reflectance», *Applied optics*, vol. 44, no. 35, pp. 7554–7563, 2005.

- [62] F. Martelli, A. Sassaroli, A. Pifferi, A. Torricelli, L. Spinelli, and G. Zaccanti, «Heuristic Green's function of the time dependent radiative transfer equation for a semi-infinite medium», *Opt. Express*, vol. 15, no. 26, pp. 18 168–18 175, 2007. [Online]. Available: <http://www.opticsexpress.org/abstract.cfm?URI=oe-15-26-18168>.
- [63] C. Sato, M. Shimada, Y. Hoshi, and Y. Yamada, «Extraction of depth-dependent signals from time-resolved reflectance in layered turbid media», *Journal of Biomedical Optics*, vol. 10, no. 6, p. 064 008, 2005.
- [64] F. Martelli, S. Del Bianco, L. Spinelli, S. Cavalieri, P. Di Ninni, T. Binzoni, A. Jelzow, R. Macdonald, and H. Wabnitz, «Optimal estimation reconstruction of the optical properties of a two-layered tissue phantom from time-resolved single-distance measurements», *Journal of biomedical optics*, vol. 20, no. 11, p. 115 001, 2015.
- [65] S. Geiger, D. Reitzle, A. Liemert, and A. Kienle, «Determination of the optical properties of three-layered turbid media in the time domain using the P 3 approximation», *OSA Continuum*, vol. 2, no. 6, pp. 1889–1899, 2019.
- [66] A. Farina, A. Torricelli, I. Bargigia, L. Spinelli, R. Cubeddu, F. Foschum, M. Jäger, E. Simon, O. Fugger, A. Kienle, F. Martelli, P. Di Ninni, G. Zaccanti, D. Milej, P. Sawosz, M. Kacprzak, A. Liebert, and A. Pifferi, «In-vivo multilaboratory investigation of the optical properties of the human head», *Biomedical Optics Express*, vol. 6, no. 7, p. 2609, 2015, ISSN: 2156-7085. DOI: 10.1364/BOE.6.002609. [Online]. Available: <https://www.osapublishing.org/abstract.cfm?URI=boe-6-7-2609>.
- [67] *Home | SOLUS*, [Online; accessed 17. Feb. 2020], Feb. 2020. [Online]. Available: <http://www.solus-project.eu>.
- [68] S. K. V. Sekar, I. Bargigia, A. D. Mora, P. Taroni, A. Ruggeri, A. Tosi, A. Pifferi, and A. Farina, «Diffuse optical characterization of collagen absorption from 500 to 1700 nm», *J. Biomed. Opt.*, vol. 22, no. 1, p. 015 006, Jan. 2017, ISSN: 1083-3668. DOI: 10.1117/1.JBO.22.1.015006.
- [69] P. Taroni, A. Bassi, D. Comelli, A. Farina, R. Cubeddu, and A. Pifferi, «Diffuse optical spectroscopy of breast tissue extended to 1100 nm», *J. Biomed. Opt.*, vol. 14, no. 5, p. 054 030, Sep. 2009, ISSN: 1083-3668. DOI: 10.1117/1.3251051.
- [70] *Assorted Spectra*, [Online; accessed 20. Feb. 2020], Sep. 2018. [Online]. Available: <https://omlc.org/spectra>.
- [71] S. B. Heymsfield, V. Stevens, R. Noel, C. McManus, J. Smith, and D. Nixon, «Biochemical composition of muscle in normal and semistarved human subjects: Relevance to anthropometric measurements», *American Journal of Clinical Nutrition*, vol. 36, no. 1, pp. 131–142, 1982, ISSN: 00029165. DOI: 10.1093/ajcn/36.1.131.
- [72] H. Menzel, C. Clement, and P. DeLuca, «ICRP Publication 110. Realistic reference phantoms: an ICRP/ICRU joint effort. A report of adult reference computational phantoms.», *Annals of the ICRP*, vol. 39, no. 2, p. 1, 2009.
- [73] H. Auger, L. Bherer, É. Boucher, R. Hoge, F. Lesage, and M. Dehaes, «Quantification of extra-cerebral and cerebral hemoglobin concentrations during physical exercise using time-domain near infrared spectroscopy», *Biomed. Opt. Express*, vol. 7, no. 10, p. 3826, Oct. 2016. DOI: 10.1364/BOE.7.003826.
- [74] E. A. Genina, A. N. Bashkatov, and V. V. Tuchin, «Optical Clearing of Cranial Bone», *Adv. Opt. Technol.*, vol. 2008, May 2008, ISSN: 1687-6393. DOI: 10.1155/2008/267867.
- [75] J. Sun, S. J. Lee, L. Wu, M. Sarntinoranont, and H. Xie, «Refractive index measurement of acute rat brain tissue slices using optical coherence tomography», *Opt. Express*, vol. 20, no. 2, p. 1084, Jan. 2012. DOI: 10.1364/OE.20.001084.
- [76] A. Villringer and B. Chance, «Non-invasive optical spectroscopy and imaging of human brain function», English, *Trends Neuroscience*, vol. 20, pp. 435–442, 1997.

Bibliography

- [77] D. Comelli, A. Bassi, A. Pifferi, P. Taroni, A. Torricelli, R. Cubeddu, F. Martelli, and G. Zaccanti, «In vivo time-resolved reflectance spectroscopy of the human forehead», *Applied optics*, vol. 46, no. 10, pp. 1717–1725, 2007.
- [78] E. Okada and D. T. Delpy, «Near-infrared light propagation in an adult head model. I. Modeling of low-level scattering in the cerebrospinal fluid layer», *Applied optics*, vol. 42, no. 16, pp. 2906–2914, 2003.
- [79] A. Custo, W. M. Wells Iii, A. H. Barnett, E. M. Hillman, and D. A. Boas, «Effective scattering coefficient of the cerebral spinal fluid in adult head models for diffuse optical imaging», *Applied optics*, vol. 45, no. 19, pp. 4747–4755, 2006.
- [80] H. Dehghani and D. T. Delpy, «Near-infrared spectroscopy of the adult head: effect of scattering and absorbing obstructions in the cerebrospinal fluid layer on light distribution in the tissue», *Appl. Opt.*, vol. 39, no. 25, pp. 4721–4729, Sep. 2000, ISSN: 2155-3165. DOI: 10.1364/AO.39.004721.
- [81] *Controlling the global obesity epidemic*, <https://www.who.int/nutrition/topics/obesity/en/>, Accessed: 2020-01-15.
- [82] K. Sun, J. Tordjman, K. Clément, and P. E. Scherer, «Fibrosis and adipose tissue dysfunction», *Cell metabolism*, vol. 18, no. 4, pp. 470–477, 2013.
- [83] J. C. F. Walker, B. Butterfield, T. A. G. Langrish, J. M. Harris, and J. M. Uprichard, *Primary Wood Processing*. London: Chapman and Hall, 1993.
- [84] A. Giordano, A. Frontini, and S. Cinti, «Convertible visceral fat as a therapeutic target to curb obesity», *Nature Reviews Drug Discovery*, vol. 15, no. 6, pp. 405–424, 2016, ISSN: 14741784. DOI: 10.1038/nrd.2016.31. arXiv: 300.
- [85] M. Guzmán-alonso and T. M. Cortazár, «Water content at different skin depths and the influence of moisturizing formulations», *Household and Personal Care Today*, vol. 11, no. February, pp. 35–40, 2016. [Online]. Available: http://www.teknoscienze.com/Contents/Riviste/PDF/HPC1%7B%5C_%7D2016%7B%5C_%7DLOW%7B%5C_%7D37-43.pdf.
- [86] *Mie scattering from collagen fibers*, https://omlc.org/classroom/ece532/class3/mie_collagen.html, Accessed: 2020-01-15.
- [87] C. D’Andrea, L. Spinelli, A. Bassi, A. Giusto, D. Contini, J. Swartling, A. Torricelli, and R. Cubeddu, «Time-resolved spectrally constrained method for the quantification of chromophore concentrations and scattering parameters in diffusing media», *Opt. Express*, vol. 14, no. 5, pp. 1888–1898, 2006. [Online]. Available: <http://www.opticsexpress.org/abstract.cfm?URI=oe-14-5-1888>.
- [88] R. Simpson, J. G. Laufer, M. Kohl-Bareis, M. Essenpreis, and M. Cope, «Near-infrared optical properties of ex-vivo human skin and subcutaneous tissues using reflectance and transmittance measurements», *Optical Tomography and Spectroscopy of Tissue: Theory, Instrumentation, Model, and Human Studies II*, vol. 2979, pp. 307–313, Aug. 1997. DOI: 10.1117/12.280259.
- [89] S. Geiger, D. Reitzle, A. Liemert, and A. Kienle, «Determination of the optical properties of three-layered turbid media in the time domain using the P 3 approximation», *OSA Continuum*, vol. 2, no. 6, p. 1889, Jun. 2019, ISSN: 2578-7519. DOI: 10.1364/OSAC.2.001889. [Online]. Available: <https://www.osapublishing.org/abstract.cfm?URI=osac-2-6-1889>.
- [90] I. Mellal, A. Oukaira, E. Kengene, and A. Lakhssassi, «Thermal Therapy Modalities for Cancer Treatment: A Review and Future Perspectives», *International Journal of Applied Science - Research and Review*, vol. 04, no. 02, pp. 1–11, 2017, ISSN: 23949988. DOI: 10.21767/2394-9988.100064. [Online]. Available: <http://www.imedpub.com/articles/thermal-therapy-modalities-for-cancertreatment-a-review-and-future-perspectives.php?aid=21099>.

- [91] L. O. ... S. Neurosurgery, Functional, and undefined 1976, «Electrophysiologic principles of radiofrequency lesion making», *karger.com*, [Online]. Available: <https://www.karger.com/Article/Abstract/102478>.
- [92] E. Choi, Y. Choi, E. Jang, J. K. ... T. K. journal of ..., and undefined 2016, «Neural ablation and regeneration in pain practice», *ncbi.nlm.nih.gov*, [Online]. Available: <https://www.ncbi.nlm.nih.gov/pmc/articles/PMC4731549/>.
- [93] Y. Anzai, R. Lufkin, A. Desalles, D. R. Hamilton, K. Farahani, and K. L. Black, «Preliminary Experience with MR-Guided Thermal Ablation of Brain Tumors», Tech. Rep.
- [94] J. F. McGahan and G. D. Dodd, *Radiofrequency ablation of the liver: Current status*, 2001. DOI: 10.2214/ajr.176.1.1760003.
- [95] J. Chua, Y. Lam, B. Tan, K. T. ... S. medical ..., and undefined 2019, «Single-centre retrospective review of risk factors for local tumour progression and complications in radiofrequency ablation of 555 hepatic lesions», *ncbi.nlm.nih.gov*, [Online]. Available: <https://www.ncbi.nlm.nih.gov/pmc/articles/PMC6482426/>.
- [96] G. Hindricks, C. Piorkowski, H. Tanner, R. Kobza, J. H. Gerds-Li, C. Carbucicchio, and H. Kottkamp, «Perception of atrial fibrillation before and after radiofrequency catheter ablation: Relevance of asymptomatic arrhythmia recurrence», *Circulation*, vol. 112, no. 3, pp. 307–313, Jul. 2005, ISSN: 00097322. DOI: 10.1161/CIRCULATIONAHA.104.518837.
- [97] K. Pillai, J. Akhter, T. Chua, M. Shehata, N. A. ... Medicine, and undefined 2015, «Heat sink effect on tumor ablation characteristics as observed in monopolar radiofrequency, bipolar radiofrequency, and microwave, using ex vivo calf liver», *ncbi.nlm.nih.gov*, [Online]. Available: <https://www.ncbi.nlm.nih.gov/pmc/articles/PMC4553952/>.
- [98] S. S. Raman, D. S. Lu, D. J. Vodopich, J. Sayre, and C. Lassman, «Creation of radiofrequency lesions in a porcine model: correlation with sonography, CT, and histopathology», *American Journal of Roentgenology*, vol. 175, no. 5, pp. 1253–1258, 2000.
- [99] J. R. Leyendecker, G. D. Dodd III, G. A. Halff, V. A. McCoy, D. H. Napier, L. G. Hubbard, K. N. Chintapalli, S. Chopra, W. K. Washburn, R. M. Esterl, *et al.*, «Sonographically observed echogenic response during intraoperative radiofrequency ablation of cirrhotic livers: pathologic correlation», *American Journal of Roentgenology*, vol. 178, no. 5, pp. 1147–1151, 2002.
- [100] L. Solbiati, M. Tonolini, and L. Cova, «Monitoring RF ablation.», *European radiology*, vol. 14 Suppl 8, P34–42, Oct. 2004, ISSN: 0938-7994. DOI: 10.1007/s10406-004-0089-y. [Online]. Available: <http://www.ncbi.nlm.nih.gov/pubmed/15700331>.
- [101] W. C. Lin, C. Buttermere, and A. Mahadevan-Jansen, «Effect of thermal damage on the in vitro optical and fluorescence characteristics of liver tissues», *IEEE Journal on Selected Topics in Quantum Electronics*, vol. 9, no. 2, pp. 162–170, 2003, ISSN: 1077260X. DOI: 10.1109/JSTQE.2003.811288.
- [102] C. ANDERSON, «Real-time spectroscopic assessment of thermal damage: implications for radiofrequency ablation*1», *Journal of Gastrointestinal Surgery*, vol. 8, no. 6, pp. 660–669, Sep. 2004, ISSN: 1091255X. DOI: 10.1016/j.gassur.2004.04.009. [Online]. Available: <https://linkinghub.elsevier.com/retrieve/pii/S1091255X04001787>.
- [103] J. W. Spliethoff, E. Tanis, D. J. Evers, B. H. W. Hendriks, W. Prevoo, and T. J. M. Ruers, «Monitoring of tumor radio frequency ablation using derivative spectroscopy», *Journal of Biomedical Optics*, vol. 19, no. 9, p. 097004, 2014, ISSN: 1083-3668. DOI: 10.1117/1.jbo.19.9.097004.
- [104] C. P. Hsu, M. K. Razavi, S. K. So, I. H. Parachikov, and D. A. Benaron, «Liver Tumor Gross Margin Identification and Ablation Monitoring during Liver Radiofrequency Treatment», *J Vasc Interv Radiol*, pp. 1473–1478, 2005. DOI: 10.1097/01.RVI.000017833.30967.39.

Bibliography

- [105] J. P. Ritz, A. Roggan, C. Isbert, and G. Müller, «Optical properties of native and coagulated porcine liver tissue between 400 and 2400 nm - Ritz - 2001 - Lasers in Surgery and Medicine - Wiley Online Library», *Lasers in surgery ...*, vol. 212, no. March, pp. 205–212, 2001. [Online]. Available: <http://onlinelibrary.wiley.com/doi/10.1002/lsm.1134/abstract%7B%5C%7D5Cnpapers3://publication/uuid/8123850E-2360-4C1D-B501-CA1DDBFD3A32>.
- [106] V. K. Nagarajan, V. R. Gogineni, S. B. White, and B. Yu, «Real time evaluation of tissue optical properties during thermal ablation of ex vivo liver tissues», *International Journal of Hyperthermia*, 2018, ISSN: 14645157. DOI: 10.1080/02656736.2018.1488278.
- [107] V. K. Nagarajan and B. Yu, «Monitoring of tissue optical properties during thermal coagulation of ex vivo tissues», *Lasers in Surgery and Medicine*, 2016, ISSN: 10969101. DOI: 10.1002/lsm.22541.
- [108] A. M. K. Nilsson, C. Stureson, D. L. Liu, and S. Andersson-Engels, «Changes in spectral shape of tissue optical properties in conjunction with laser-induced thermotherapy», *Applied Optics*, vol. 37, no. 7, p. 1256, 1998, ISSN: 0003-6935. DOI: 10.1364/ao.37.001256.
- [109] A. N. Yaroslavsky, P. C. Schulze, I. V. Yaroslavsky, R. Schober, F. Ulrich, and H. J. Schwarzmair, «Optical properties of selected native and coagulated human brain tissues in vitro in the visible and near infrared spectral range», *Physics in Medicine and Biology*, vol. 47, no. 12, pp. 2059–2073, 2002, ISSN: 00319155. DOI: 10.1088/0031-9155/47/12/305.
- [110] I. Cilesiz and A. J. Welch, «Light dosimetry: effects of dehydration and thermal damage on the optical properties of the human aorta: errata», *Applied Optics*, vol. 33, no. 16, p. 3571, 1994, ISSN: 00036935. DOI: 10.1364/AO.33.003571.
- [111] A. N. Bashkatov, E. A. Genina, and V. V. Tuchin, «OPTICAL PROPERTIES OF SKIN, SUBCUTANEOUS, AND MUSCLE TISSUES: A REVIEW», *J. Innov. Opt. Health Sci.*, vol. 04, no. 01, pp. 9–38, Jan. 2011, ISSN: 1793-5458. DOI: 10.1142/S1793545811001319.
- [112] J. P. Joseph and K. Rajappan, «Radiofrequency ablation of cardiac arrhythmias: past, present and future», *QJM*, vol. 105, no. 4, pp. 303–314, Apr. 2012, ISSN: 1460-2725. DOI: 10.1093/qjmed/hcr189.
- [113] S. McDermott and D. A. Gervais, «Radiofrequency Ablation of Liver Tumors», *Semin. Intervent. Radiol.*, vol. 30, no. 1, p. 49, Mar. 2013. DOI: 10.1055/s-0033-1333653.
- [114] S. Shankar, E. VanSonnenberg, S. G. Silverman, P. R. Morrison, and K. Tuncali, «Soft Tissue Ablation», *SpringerLink*, pp. 369–376, 2005. DOI: 10.1007/0-387-28674-8_30.
- [115] S. Gananadha, S. Wulf, and D. L. Morris, «Safety and efficacy of radiofrequency ablation of brain: a potentially minimally invasive treatment for brain tumours», *Minim. Invasive Neurosurg.*, vol. 47, no. 6, pp. 325–328, Dec. 2004, ISSN: 0946-7211. DOI: 10.1055/s-2004-830124.
- [116] B. D. Henz, P. A. Friedman, C. J. Bruce, D. R. Holmes Jr., M. Bower, M. Madhavan, C. V. DeSimone, D. Wahnschaffe, S. Berhow, A. J. Danielsen, D. J. Ladewig, S. B. Mikell, S. B. Johnson, S. H. Suddendorf, T. Kara, G. A. Worrell, and S. J. Asirvatham, «Advances in Radiofrequency Ablation of the Cerebral Cortex in Primates Using the Venous System: Improvements for Treating Epilepsy with Catheter Ablation Technology», *Epilepsy research*, vol. 108, no. 6, p. 1026, Aug. 2014. DOI: 10.1016/j.eplesyres.2014.04.002.
- [117] C. de Boor, *L-436 A Practical Guide to Splines*. Springer-Verlag New York, 1978, p. 348, ISBN: 978-0-387-95366-3. [Online]. Available: <http://www.springer.com/us/book/9780387953663>.
- [118] Wei-Chiang Lin, C. Buttemere, and A. Mahadevan-Jansen, «Effect of thermal damage on the in vitro optical and fluorescence characteristics of liver tissues», *IEEE Journal of Selected Topics in Quantum Electronics*, vol. 9, no. 2, pp. 162–170, Mar. 2003, ISSN: 1077-260X. DOI: 10.1109/JSTQE.2003.811288. [Online]. Available: <http://ieeexplore.ieee.org/document/1238967/>.

- [119] R. Splinter, R. H. Svenson, L. Littmann, J. R. Tuntelder, C. H. Chuang, G. P. Tatsis, and M. Thompson, «Optical properties of normal, diseased, and laser photocoagulated myocardium at the Nd: YAG wavelength», *Lasers in surgery and medicine*, vol. 11, no. 2, pp. 117–124, 1991.
- [120] J. W. Pickering, P. Posthumus, and M. J. van Gemert, «Continuous measurement of the heat-induced changes in the optical properties (at 1,064 nm) of rat liver», *Lasers in surgery and medicine*, vol. 15, no. 2, pp. 200–205, 1994.
- [121] J. F. Black and J. K. Barton, «Chemical and Structural Changes in Blood Undergoing Laser Photocoagulation», *Photochemistry and Photobiology*, vol. 80, no. 1, p. 89, 2004, ISSN: 0031-8655. DOI: 10.1562/2004-03-05-ra-102.1.
- [122] J. F. Black, N. Wade, and J. K. Barton, «Mechanistic comparison of blood undergoing laser photocoagulation at 532 and 1,064 nm», *Lasers in Surgery and Medicine*, vol. 36, no. 2, pp. 155–165, 2005, ISSN: 01968092. DOI: 10.1002/lsm.20134.
- [123] J. K. Barton, D. P. Popok, and J. F. Black, «Thermal analysis of blood undergoing laser photocoagulation», *IEEE Journal of selected topics in quantum electronics*, vol. 7, no. 6, pp. 936–943, 2001.
- [124] «Cooperative Phenomena in Two-pulse, Two-color Laser Photocoagulation of Cutaneous Blood Vessels»,
- [125] L. Randeberg, J. Bonesrønning, M. Dalaker, J. Nelson, and L. Svaasand, «Methemoglobin formation during laser induced photothermolysis of vascular skin lesions», *Lasers in Surgery and Medicine: The Official Journal of the American Society for Laser Medicine and Surgery*, vol. 34, no. 5, pp. 414–419, 2004.
- [126] *Optical Absorption of Carbonized Tissue*, <https://omlc.org/spectra/carbon/index.html>, Accessed: 2020-01-15.
- [127] J. R. Collins, «Change in the Infra-Red Absorption Spectrum», vol. 91, no. 1892, 1910. DOI: <https://doi.org/10.1103/PhysRev.26.771>.
- [128] —, «Change in the infra-red absorption spectrum of water with temperature», *Physical Review*, vol. 26, no. 6, pp. 771–779, 1925, ISSN: 0031899X. DOI: 10.1103/PhysRev.26.771.
- [129] S. H. Chung, A. E. Cerussi, S. I. Merritt, J. Ruth, and B. J. Tromberg, «Non-invasive tissue temperature measurements based on quantitative diffuse optical spectroscopy (DOS) of water», *Physics in Medicine and Biology*, vol. 55, no. 13, pp. 3753–3765, 2010, ISSN: 00319155. DOI: 10.1088/0031-9155/55/13/012.
- [130] E. Salomatina and A. Yaroslavsky, «Evaluation of the in vivo and ex vivo optical properties in a mouse ear model», *Physics in Medicine & Biology*, vol. 53, no. 11, p. 2797, 2008.
- [131] P. Moroz, S. K. Jones, and B. N. Gray, «Status of hyperthermia in the treatment of advanced liver cancer», *Journal of surgical oncology*, vol. 77, no. 4, pp. 259–269, 2001.
- [132] *TRL Scale in Horizon 2020 and ERC - Explained - Enspire Science Ltd.* [Online; accessed 10. Feb. 2020], Jan. 2018. [Online]. Available: <https://enspire.science/trl-scale-horizon-2020-erc-explained>.
- [133] H. Wabnitz, A. Jelzow, M. Mazurenka, O. Steinkellner, R. Macdonald, D. Milej, N. Żołek, M. Kacprzak, P. Sawosz, R. Maniewski, A. Liebert, S. Magazov, J. C. Hebden, F. Martelli, P. Di Ninni, G. Zaccanti, A. Torricelli, D. Contini, R. Re, L. M. Zucchelli, L. Spinelli, R. Cubeddu, and A. Pifferi, «Performance assessment of time-domain optical brain imagers, part 2: nEUROpt protocol», *J. Biomed. Opt.*, vol. 19, no. 8, p. 086012, Aug. 2014, ISSN: 1083-3668. DOI: 10.1117/1.JBO.19.8.086012.

Bibliography

- [134] H. Wabnitz, D. R. Taubert, M. Mazurenka, O. Steinkellner, A. Jelzow, R. Macdonald, D. Milej, P. Sawosz, M. Kacprzak, A. Liebert, R. Cooper, J. Hebden, A. Pifferi, A. Farina, I. Bargigia, D. Contini, M. Caffini, L. Zucchelli, L. Spinelli, R. Cubeddu, and A. Torricelli, «Performance assessment of time-domain optical brain imagers, part 1: basic instrumental performance protocol», *Journal of Biomedical Optics*, vol. 19, no. 8, p. 086010, 2014, ISSN: 1083-3668. DOI: 10.1117/1.JBO.19.8.086010. [Online]. Available: <http://biomedicaloptics.spiedigitallibrary.org/article.aspx?doi=10.1117/1.JBO.19.8.086010>.
- [135] B. J. Tromberg, Z. Zhang, A. Leproux, T. D. O’Sullivan, A. E. Cerussi, P. Carpenter, R. S. Mehta, D. Roblyer, W. Yang, K. D. Paulsen, B. W. Pogue, S. Jiang, P. Kaufman, A. G. Y. AG, S. H. Chung, M. Schnall, B. S. Snyder, N. Hylton, D. A. Boas, S. A. Carp, S. J. Isakoff, and D. Mankoff, «Predicting Responses to Neoadjuvant Chemotherapy in Breast Cancer: ACRIN 6691 Trial of Diffuse Optical Spectroscopic Imaging (DOSI)», *Cancer research*, vol. 76, no. 20, p. 5933, Oct. 2016. DOI: 10.1158/0008-5472.CAN-16-0346.
- [136] S. Kleiser, D. Ostojic, B. Andresen, N. Nasserli, H. Isler, F. Scholkmann, T. Karen, G. Greisen, and M. Wolf, «Comparison of tissue oximeters on a liquid phantom with adjustable optical properties: an extension», *Biomed. Opt. Express*, vol. 9, no. 1, p. 86, Jan. 2018. DOI: 10.1364/BOE.9.000086.
- [137] *BitMap ITN*, [Online; accessed 14. Feb. 2020], Feb. 2020. [Online]. Available: <http://www.bitmap-itn.eu>.
- [138] A. Pifferi, A. Torricelli, R. Cubeddu, G. Quarto, R. Re, S. K. V. Sekar, L. Spinelli, A. Farina, F. Martelli, and H. Wabnitz, «Mechanically switchable solid inhomogeneous phantom for performance tests in diffuse imaging and spectroscopy», *J. Biomed. Opt.*, vol. 20, no. 12, p. 121304, Jul. 2015, ISSN: 1083-3668. DOI: 10.1117/1.JBO.20.12.121304.
- [139] A. Behera, L. Di Sieno, S. Rohilla, A. Pifferi, A. Torricelli, D. Contini, B. Krämer, F. Koberling, and A. Dalla Mora, «Large area SiPM and high throughput timing electronics: toward new generation time-domain instruments», in *European Conference on Biomedical Optics*, Optical Society of America, 2019, 11074_1.
- [140] The Optical Society, «Diagnosing Breast Cancer Using Red Light», *The Optical Society*, Mar. 2018. [Online]. Available: https://www.osa.org/en-us/about_osa/newsroom/news_releases/2018/diagnosing_breast_cancer_using_red_light.
- [141] H. Wabnitz, M. Moeller, A. Liebert, H. Obrig, J. Steinbrink, and R. Macdonald, «Time-resolved near-infrared spectroscopy and imaging of the adult human brain», in *Oxygen transport to tissue XXXI*, Springer, 2010, pp. 143–148.
- [142] A. Jelzow, H. Wabnitz, I. Tachtsidis, E. Kirilina, R. Brühl, and R. Macdonald, «Separation of superficial and cerebral hemodynamics using a single distance time-domain NIRS measurement», *Biomedical optics express*, vol. 5, no. 5, pp. 1465–1482, 2014.
- [143] *Near-Infrared, Non-Invasive Tissue Oximeter | OxiplexTS | ISS*, [Online; accessed 13. Feb. 2020], Jan. 2020. [Online]. Available: <http://www.iss.com/biomedical/instruments/oxiplexTS.html>.
- [144] A. Pifferi, A. Torricelli, R. Cubeddu, G. Quarto, R. Re, S. K. V. Sekar, L. Spinelli, A. Farina, F. Martelli, and H. Wabnitz, «Mechanically switchable solid inhomogeneous phantom for performance tests in diffuse imaging and spectroscopy», *Journal of Biomedical Optics*, vol. 20, no. 12, p. 121304, 2015, ISSN: 1083-3668. DOI: 10.1117/1.JBO.20.12.121304. [Online]. Available: <http://biomedicaloptics.spiedigitallibrary.org/article.aspx?doi=10.1117/1.JBO.20.12.121304>.
- [145] E. Martinenghi, A. Dalla Mora, D. Contini, A. Farina, F. Villa, A. Torricelli, and A. Pifferi, «Spectrally Resolved Single-Photon Timing of Silicon Photomultipliers for Time-Domain Diffuse Spectroscopy», *Photonics Journal, IEEE*, vol. 7, pp. 1–12, Aug. 2015. DOI: 10.1109/JPHOT.2015.2456070.

- [146] *Performance Assessment and Standardization in Biophotonics is back. Save the date! - Digital Single Market - European Commission*, [Online; accessed 14. Feb. 2020], Jul. 2019. [Online]. Available: <https://ec.europa.eu/digital-single-market/en/news/performance-assessment-and-standardization-biophotonics-back-save-date>.
- [147] *Performance Assessment and Standardization in Biophotonics Workshop - Digital Single Market - European Commission*, [Online; accessed 14. Feb. 2020], Dec. 2018. [Online]. Available: <https://ec.europa.eu/digital-single-market/en/news/performance-assessment-and-standardization-biophotonics-workshop>.